PRODUCTION AND CHARACTERIZATION OF NANO-CLUSTER MATERIALS

by

TIMOTHY MARTIN AYERS

(Under the Direction of Michael A. Duncan)

ABSTRACT

The primary focus of this thesis is to present a new method by which metal-cluster materials may be produced and isolated. A laser vaporization flowtube reactor (LVFR) has been built for this purpose. This new apparatus combines the versatility of a high repetition rate, high power laser vaporization cluster source with a known method for cluster production and isolation. Initial experiments on the apparatus reveal that titanium and vanadium oxide clusters coated with tetrahydrofuran can be produced, isolated and characterized efficiently. These experiments also showed that the clusters isolated depend heavily on the synthesis conditions inside the LVFR. The secondary focus of this thesis is to introduce nanotechnology to chemistry students early in their academic development. In order for new generations of scientists to become familiar with modern science, new laboratory experiments that have applications involving lasers and nanotechnology must be incorporated into undergraduate laboratories. Accordingly, this thesis contains an advanced laboratory experiment where inorganic cluster materials are produced using a laser desorption time-of-flight mass spectrometer (LD-TOF). The remainder of this thesis is dedicated to the production and characterization of nano-cluster materials using the LD-TOF, including metal-polycyclic aromatic hydrocarbon adducts.

INDEX WORDS: Laser vaporization, Laser desorption, Gas phase synthesis, nanoparticles, Polycyclic aromatic hydrocarbons, Transition metal oxides

PRODUCTION AND CHARACTERIZATION OF NANO-CLUSTER MATERIALS

by

TIMOTHY MARTIN AYERS

B.S. The University of West Georgia, 2001

A Dissertation Submitted to the Graduate Faculty of The University of Georgia in Partial Fulfillment of the Requirements for the Degree

DOCTOR OF PHILOSOPHY

ATHENS, GEORGIA

2006

PRODUCTION AND CHARACTERIZATION OF NANO-CLUSTER MATERIALS

by

TIMOTHY MARTIN AYERS

Major Professor:	Michael A. Duncan
Committee:	Charles Kutal Geoffrey. D. Smith

Electronic Version Approved:

Maureen Grasso
Dean of the Graduate School
The University of Georgia
August 2006

DEDICATION

To my parents and friends,

It's a dangerous business stepping out your door. You step into the road, and if you don't keep your feet, there's no knowing where you'll be swept off to. I've seen foreign cultures, ever-flowing rivers, lakes in the sky, snow in July...but none compares to home.

TABLE OF CONTENTS

Page

CHAPTER

1 HISTORY OF NANOSCIENCE 1

1.1 FROM SCIENCE FICTION TO PRACTICAL SCIENCE . . . 2

1.2 SOL-GEL PROCESSES 4

1.3 QUANTUM DOTS 6

1.4 GAS PHASE SYNTHETIC METHODS 7

1.5 REFERENCES 9

2 EXPERIMENTAL 16

2.1 LASER DESORPTION APPARATUS 17

2.2 LASER VAPORIZATION FLOWTUBE APPARATUS . . . 19

2.3 REFERENCES 21

3 CLUSTER EDUCATION 25

3.1 BACKGROUND 26

3.2 EXPERIMENTAL AND SAFETY 27

3.3 INORGANIC CLUSTER MATERIALS 28

3.4 CONCLUSIONS 35

3.5 REFERENCES 35

4 TRANSITION METAL – PAH COMPLEXES 42

4.1 BACKGROUND 43
4.2 EXPERIMENTAL 46
4.3 RESULTS AND DISCUSSION 46
4.4 STRUCTURES AND GROWTH TRENDS 63
4.5 REFERENCES 67
5 PRODUCTION AND ISOLATION OF TRANSITION METAL OXIDE NANO-CLUSTER MATERIALS 88
5.1 BACKGROUND 89
5.2 EXPERIMENTAL 91
5.3 TITANIUM OXIDE – THF 91
5.4 VANADIUM OXIDE – THF 96
5.5 CONCLUSIONS 98
5.6 REFERENCES 99
6 FUTURE DIRECTIONS 110
6.1 LASER VAPORIZATION FLOWTUBE MODIFICATIONS . . 111
6.2 FUTURE EXPERIMENTS 112
6.3 REFERENCES 113

CHAPTER 1

HISTORY AND IMPORTANCE OF NANOSCIENCE

1.1 FROM SCIENCE FICTION TO PRACTICAL SCIENCE

One frequent misconception is that nanoscience is a relatively new idea. In reality, the scientific world has envisioned the production, characterization and manipulation of structures and chemical processes on the nanometer scale for decades. In a famous talk given in 1959, Richard Feynman suggested that science had only just begun to explore the microscopic frontier.[1] Motion pictures like "the Fantastic Voyage" allowed audiences to imagine devices which could reduce a human to a size smaller than the human cell.[2] But in reality, new innovations in instrumentation which could make nanoscience possible were just appearing in the 1950's. E.W. Mueller invented the field electron microscope in 1951, and it was the first instrument that allowed observation of atoms and their arrangements on surfaces.[3] More advanced surface imaging instruments including scanning tunneling microscope and atomic force microscopy were not invented until 1982[4] and 1986,[5] respectively, by Bennig and coworkers. It was not a coincidence that an explosion in nanoscience also took place soon after these inventions appeared. Since scientists could "see" how atoms were arranged on surfaces, manipulating chemistry at the atomic level became possible.

The motivation for materials research in the nanometer size range is the interesting properties which many systems may offer. Having a size between molecular and bulk structures, nanomaterials have an blend of properties which are not very well understood. Figure 1 illustrates one of the unique characteristics of particles with nanometer dimensions. At small radii, the number of atoms on the surface of a particle is a significant fraction of the total number of atoms in the system. This characteristic results in the greater catalytic activity for small particles of many systems in comparison to their bulk materials. For example, gold is for the most part chemically unreactive. In fact, surface science research and theoretical calculations have proved that no hydrogenation or oxidation reactions should take place on bulk gold surfaces, indicating that gold

should be catalytically inactive.[6] However, Haruta and coworkers discovered that small particles (less than 10 nm dia.) of gold supported on metal oxide surfaces showed unexpected catalytic behavior in hydrogenation, oxidation and reduction processes.[6-8]

In special cases such as fullerenes and nanotubes,[9-11] the small dimension of the particles leads to an increase in stability and durability. Unsaturated chemical bonding and the interconnectivity of the carbon atoms in these systems produce particularly robust structures. For example, the binding energy of each carbon atom in the C_{60} cage structure is 7.4 eV,[10] whereas a typical carbon – carbon double bond has a binding energy of 6.29 eV.[12] Accordingly, many researchers have speculated that fullerene and nanotube materials could be utilized as lubricants,[11] working parts in nano-machinery,[13] or even as materials for futuristic projects such as a space elevator.[14]

However, the physical dimension of nanomaterials is not the only characteristic that makes them special. In the early part of the 20th century, de Broglie introduced the theory that every particle has an intrinsic wavelength that is inversely proportional to the particle's momentum. However, a particle's wavelength (de Broglie wavelength) is only a concern when the size of the physical system to which the particle is confined is comparable to its wavelength. In this instance, the behavior of the particle is best described using quantum mechanics.[15,16] Since the mass of an electron is small, then its de Broglie wavelength is on the order of nanometers. Therefore, electrons in nanomaterials are not allowed to take on arbitrary values as in bulk lattices but instead exhibit a distinct energy level spectrum based on the size of the box (size of the nanoparticle) to which they are confined. The quantum behavior of electrons in nanomaterials may therefore result in unique optical, electronic and magnetic properties.[17-19] However, an important question remains...how did nanotechnology develop from an idea to a reality?

1.2 SOL-GEL PROCESSES

The advent of sol-gel processes represents the very beginning of nanotechnology. The sol-gel process includes a wide range of organic and inorganic materials which all share a common method of preparation.[20] The first phase of the process involves the generation of a colloidal suspension or "sol". This suspension is then converted into a viscous gel and subsequently to a solid material in the final phases. The use of colloids in practical applications dates back 17,000 years, where primitive man used these materials in cave paintings at Lascaux, France.[20] From the Roman Empire through the 19th century, sol-gel processes were used in a variety of applications, including the production of glasses, ceramics, concretes and stained glass windows. However, all of the first users of sol-gel process were oblivious to the scientific principles underlying the method.

At the beginning of the 20th century, an explosion in sol-gel research began as its potential for scientific and practical applications began to be realized. W. A. Patrick contributed greatly to interest in this area when he discovered that metals embedded in silica gels resulted in catalytic activity.[21-23] Common salts of transition metals such as iron chloride hexahydrate were dissolved into the "sol" and became trapped in the matrix during gel processing. In particular, embedded iron and sodium were found useful for the catalytic production of sulfur trioxide (SO_3).[22]

The notable scientist, Michael Faraday, discovered and prepared the first gold colloid materials in 1857. He associated the bright red color of the colloidal suspension to the extremely small size of the particles but did not possess the tools necessary to confirm his hypothesis.[24] Almost one hundred years later, the size of the particles in Faraday's colloidal solutions was finally established. Using low resolution electron microscopy, Turkevich *et al* was able to estimate the average size of the gold colloids was around 60 Å.[25] Turkevich *et al* also discovered that the shape of the gold colloids produced is linked to the agent employed for the reduction of the gold

salt, sodium chloroaurate ($NaAuCl_4$).[26] For example, reduction with sodium nitrate yields spherical particles whereas reduction with carbon monoxide yields cylindrical particles. Thus, this research became the first example of shape manipulation of nano-size colloidal materials.

Recently, the sol-gel method has been used to trap a variety of nano-materials in hopes of achieving new catalytic and optical properties. Fullerenes and fullerene derivatives have been incorporated in gels using a variety of methods,[27] with the intention of producing new energy storage and nonlinear optical devices.[28,29] Since Patrick's discovery that sol-gels could be used as supports for catalysts, a variety of metals and metal oxides trapped within the gel matrices have also been studied extensively.[30-32]

Since the number of practical uses of the sol-gel process has greatly increased in recent decades, scientists have also been compelled to explain the mechanisms, kinetics and thermodynamics of gel formation.[33,34] Through these studies, both the advantages and disadvantages of the sol-gel process have been recognized.[20,35] In general, sol-gel processes involve low temperatures and mild pH conditions, therefore degradation of the material trapped within the gel is minimized. However, careful aging and drying are required to achieve a uniform sol-gel material. Also, during sol-gel densification and drying, the material is subject to dimensional changes and stress cracking. Though the sol-gel process is a proven and thoroughly characterized technique, it is only applicable to solution-based chemistry. Thus, it is unclear how the sol-gel process could be adapted to include unique clusters and nanoparticles produced by gas phase methods.

1.3 QUANTUM DOTS

The discovery and characterization of quantum dots resulted in another leap in the field of nanotechnology. Quantum dots are typically made of semiconductor materials on the order of nanometers in size. This happens to be near the de Broglie wavelength of the electrons in the system, therefore the electrons in these systems are confined to discrete energy levels. What makes quantum dots unusual is the potential for controlling their size and shape in order to control the number of electrons and the structure of energy levels in these systems.[36]

Some of the first examples of semiconductor quantum dots were produced by Reed *et al*[37] and Brus and coworkers.[38] Brus and coworkers found they were able to control the absorption spectrum of CdSe quantum dots by simply controlling their size. An increase in the size of the CdSe quantum dots leads to a larger potential box to which the electrons in the system are confined and consequently red-shifts the UV-Vis spectrum.[38] Since this discovery, numerous examples of semiconductor quantum dots have been produced using a variety of techniques including lithography,[39-41] vapor deposition,[37,42-44] and colloid synthetic methods.[18,38,45,46]

Semiconductor quantum dots have numerous potential applications including lasers,[47,48] photon detectors,[49,50] and biological tagging and sensing.[51-53] Semiconductor diode lasers have long been useful in optical fiber telecommunications. However, quantum dot lasers have many potential advantages over their quantum well counterparts, including lower threshold currents and narrower line widths.[48] Another potentially fascinating application of quantum dots lies in the area of optical memories. 3-D arrays of quantum dots which are addressed optically could retain vast amounts of information, surpassing current 2-D micro-electronic devices.[54] In fact, practical applications of quantum dots are just beginning to be realized. Quantum dots may soon be found in everyday household items as the field matures.

1.4 GAS PHASE SYNTHETIC TECHNIQUES

"Wet" chemistry synthetic methods were the first to be utilized in nanomaterials production. Recently, many researchers are focusing on gas phase synthetic processes because these methods have certain advantages over liquid-based methods. Of these advantages, one of the most important is that gas-phase processes generally are more pure environments for synthesis.[54] Impurities in semiconductor nanomaterials are particularly detrimental for the production of electronic devices. Therefore, the production of nanomaterials intended for nano-electronics may be best performed using gas phase procedures. Another advantage is that gas phase synthetic methods can be adapted to continuous production processes, whereas, liquid based synthetic methods are typically executed in batch form.[54] Batch processes can result in product variation from one batch to the next, reducing the quality of product produced.

Gas phase synthetic techniques are also attractive since many fascinating cluster species have been detected in gas phase experiments but have not been successfully isolated. C_{60} was discovered in molecular beam experiments by Smalley and coworkers in 1985,[9,55,56] and isolated in macroscopic quantities by Krätschmer and Huffman in 1990.[57] It thus became the first example of a cluster molecule found in gas phase experiments to be isolated. Since this achievement, gas phase isolation of cluster materials has primarily been limited to fullerenes and metallo-fullerenes.[10] Fullerene based systems are synthesized by laser discharge or carbon arc sources,[10,58-62] are relatively inert, and can often be extracted from soot and dissolved directly using ordinary solvents. However, fullerenes remain a rare example of a cluster species that was first discovered in gas phase experiments and subsequently isolated in bulk quantities.

Of particular interest to our research group are metal-containing cluster species which are a particular challenge for isolation due to problems of solubility and reactivity. Of these are the

M_8C_{12} metal carbide clusters, also known as "met-cars," which were discovered by Castleman and coworkers in 1992,[63-68] and have been studied extensively by our research group.[69-78] Our research group has also studied other extremely stable metal-carbon clusters of the form $M_{14}C_{13}$, which exist as molecular "nanocrystals".[69-78] Yet another class of very stable clusters produced in gas phase experiments and studied extensively by our research group includes metal adducts with polycyclic aromatic hydrocarbons (PAH's).[79-84] Neither the met-car, nanocrystal, nor metal-PAH systems have been isolated in pure form.[85] Unfortunately, the favorable characteristics experienced in fullerene isolation are not generally expected for metal-containing clusters. Although the bonding stability of metal-containing clusters may be quite high (eg. metal carbides contain stronger bonds than the fullerenes)[85], these systems contain exposed transition metals, and are therefore expected to be highly reactive. Consequently, the conditions for producing, isolating and stabilizing these cluster materials are not at all obvious.

The primary focus of this thesis is to present a new method by which metal-cluster materials may be produced and isolated. However, the secondary focus is to introduce nanotechnology to science students early in their academic development. In order for new generations of scientists to become familiar with modern science, new laboratory experiments that have applications involving lasers and nanotechnology must be incorporated into undergraduate laboratories. Accordingly, this thesis contains an advanced laboratory experiment where cluster materials are produced using a laser vaporization time-of-flight mass spectrometer. The remainder of the thesis is dedicated to the production and characterization of nano-cluster materials, including metal-PAH adducts and metal oxide nanomaterials.

1.5 REFERENCES

(1) Feynman, R. *Eng. Sci.* **1960**, *23*, 22.

(2) Fleischer, R. Fantastic Voyage; 20th Century Fox: US, 1966.

(3) Mueller, E. W. *Z. Phys.* **1951**, *131*, 136.

(4) Binnig, G.; Rohrer, H.; Gerber, C.; Weibel, E. *Phys. Rev. Lett.* **1982**, *49*, 57.

(5) Binnig, G.; Quate, C. F.; Gerber, C. *Phys. Rev. Lett.* **1986**, *56*, 930.

(6) Haruta, M. *Chem. Rec.* **2003**, *3*, 75.

(7) Haruta, M. *Catal. Surv. Jpn.* **1997**, *1*, 61.

(8) Haruta, M. *Nature* **2005**, *437*, 1098.

(9) Kroto, H. W.; Heath, J. R.; O'Brien, S. C.; Curl, R. F.; Smalley, R. E. *Nature* **1985**, *318*, 162.

(10) *Science of Fullerenes and Carbon Nanotubes*; Dresselhaus, M. S.; Dresselhaus, G.; Eklund, P. C., Eds.; Academic Press: San Diego, 1996.

(11) Vul', A. Y.; Huffman, D. R. *Mol. Cryst. Liq. Crys. C* **1998**, *10*, 37.

(12) Carey, F. A.; Sundberg, R. J. *Advanced Organic Chemistry. Part A: Structure and Mechanisms*, 2nd ed.; Plenum Press: New York, 1984.

(13) Shirai, Y.; Osgood, A. J.; Zhao, Y.; Yao, Y.; Saudan, L.; Yang, H.; Yu-Hung, C.; Alemany, L. B.; Sasaki, T.; Morin, J.-F.; Guerrero, J. M.; Kelly, K. F.; Tour, J. M. *J. Am. Chem. Soc.* **2006**, *128*, 4854.

(14) Pugno, N. M. *Los Alamos National Laboratory, Preprint Archive, Condensed Matter* **2006**, 1.

(15) *Clusters and Colloids: From Theory to Applications*; Schmid, G., Ed.; Wiley-VCH: Weinheim, 1994, pp 555.

(16) *Nanoparticles. From Theory to Application*; Schmid, G., Ed.; Wiley-VCH: Weinheim, 2004, pp 434.

(17) Alivisatos, A. P.; Harris, A. L.; Levinos, N. J.; Steigerwald, M. L.; Brus, L. E. *J. Chem. Phys.* **1988**, *89*, 4001.

(18) Steigerwald, M. L.; Brus, L. E. *Abstr. Pap. Am. Chem. S.* **1990**, *199*, 162.

(19) Brus, L. E.; Trautman, J. K. *Philos T Roy Soc A* **1995**, *353*, 313.

(20) Brinker, C. J.; Scherer, G. W. *Sol-Gel Science: The Physics and Chemistry of Sol-Gel Processing*; Academic Press: London, 1990.

(21) Patrick, W. A. Silica Gel. US 1,297,724, 1919.

(22) Patrick, W. A. Gels; Absorbents For Gases; Catalytic Agents. GB 159,508, 1921.

(23) Patrick, W. A. Catalysts. GB 208,656, 1923.

(24) Faraday, M. *Philos. Trans.* **1857**, *147*, 145.

(25) Turkevich, J.; Stevenson, P. C.; Hillier, J. *Disc. Faraday Soc.* **1951**, *11*, 55.

(26) Thomas, J. M. *Pure Appl. Chem.* **1988**, *60*, 1517.

(27) Brusatin, G.; Innocenzi, P. *J. Sol-Gel Sci. Technol.* **2001**, *22*, 189.

(28) Zerda, T. W.; Brodka, A.; Coffer, J. *J. Non-Cryst. Solids* **1994**, *168*, 33.

(29) Chollet, P. A.; Kajzar, F. *J. Sol-Gel Sci. Technol.* **2001**, *22*, 255.

(30) Livage, J. *J. Solid State Chem.* **1986**, *64*, 322.

(31) Rao, C. N. R. *Acc. Chem. Res.* **1987**, *20*, 228.

(32) Cao, G. *J Phys Chem B* **2004**, *108*, 19921.

(33) Brinker, C. J.; Scherer, G. W. *J. Non-Cryst. Solids* **1985**, *70*, 301.

(34) Wright, J. D.; Sommerdijk, N. A. J. M. *Sol-Gel Materials: Chemistry and Applications*; Gordon and Breach Science Publishers: Amsterdam, 2001.

(35) MacKenzie, J. D. *J. Non-Cryst. Solids* **1988**, *100*, 162.

(36) Jacak, L.; Hawrylak, P.; Wójs, A. *Quantum Dots*; Springer: Berlin, 1998.

(37) Reed, M. A.; Bate, R. T.; Bradshaw, K.; Duncan, W. M.; Frensley, W. R.; Lee, J. W.; Shih, H. D. *J. Vac. Sci. Technol., B* **1986**, *4*, 358.

(38) Steigerwald, M. L.; Alivisatos, A. P.; Gibson, J. M.; Harris, T. D.; Kortan, R.; Muller, A. J.; Thayer, A. M.; Duncan, T. M.; Douglass, D. C.; Brus, L. E. *J. Am. Chem. Soc.* **1988**, *110*, 3046.

(39) Arnot, H.; Andrews, S. R.; Beaumont, S. P. *Microelectron. Eng.* **1989**, *9*, 365.

(40) Andrews, S. R.; Arnot, H. E. G. *Superlattices Microstruct.* **1991**, *9*, 433.

(41) Bryant, G. W. *J Lumin* **1996**, *70*, 108.

(42) Leonard, D.; Krishnamurthy, M.; Fafard, S.; Merz, J. L.; Petroff, P. M. *J. Vac. Sci. Technol., B* **1994**, *12*, 1063.

(43) Leonard, D.; Fafard, S.; Pond, K.; Zhang, Y. H.; Merz, J. L.; Petroff, P. M. *J. Vac. Sci. Technol., B* **1994**, *12*, 2516.

(44) Franchi, S.; Trevisi, G.; Seravalli, L.; Frigeri, P. *Prog. Cryst. Growth Charact. Mater.* **2003**, *47*, 166.

(45) Schmid, G. *Chem. Rev.* **1992**, *92*, 1709.

(46) Vanmaekelbergh, D.; Liljeroth, P. *Chem. Soc. Rev.* **2005**, *34*, 299.

(47) Bimberg, D. *J. Phys. D: Appl. Phys.* **2005**, *38*, 2055.

(48) Henini, M.; Bugajski, M. *Microelectron. J.* **2005**, *36*, 950.

(49) Rogalski, A. *Progr. Quant. Electr.* **2003**, *27*, 59.

(50) Stiff-Roberts, A. D.; Chakrabarti, S.; Su, X.; Bhattacharya, P. *Laser Focus World* **2005**, *41*, 103.

(51) Bruchez, M., Jr.; Moronne, M.; Gin, P.; Weiss, S.; Alivisatos, A. P. *Science* **1998**, *281*, 2013.

(52) Alivisatos, P. *Pure Appl. Chem.* **2000**, *72*, 3.

(53) Alexson, D.; Chen, H.; Cho, M.; Dutta, M.; Li, Y.; Shi, P.; Raichura, A.; Ramadurai, D.; Parikh, S.; Stroscio, M. A.; Vasudev, M. *J. Phys.: Condens. Matter* **2005**, *17*, R637.

(54) Kruis, F. E.; Fissan, H.; Peled, A. *J. Aerosol Sci.* **1998**, *29*, 511.

(55) Kroto, H. W. *Science* **1988**, *242*, 1139.

(56) Curl, R. F.; Smalley, R. E. *Science* **1988**, *242*, 1017.

(57) Krätschmer, W.; Lamb, L. D.; Fostirpoulos, K.; Huffman, D. R. *Nature* **1990**, *347*, 354.

(58) Haufler, R. E.; Conceicao, J.; Chibante, L. P. F.; Chai, Y.; Byrne, N. E.; Flanagan, S.; Haley, M. M.; O'Brien, S. C.; Pan, C.; Xiao, Z.; Billups, W. E.; Ciufolini, M. A.; Hauge, R. H.; Margrave, J. L.; Wilson, L. J.; Curl, R. F.; Smalley, R. E. *J. Phys. Chem.* **1990**, *94*, 8634.

(59) Koch, A. S.; Khemani, K. C.; Wudl, F. *J. Org. Chem.* **1991**, *56*, 4543.

(60) Chai, Y.; Guo, T.; Changming, J.; Haufler, R. E.; Chibante, L. P. F.; Fure, J.; Wang, L. S.; Alford, J. M.; Smalley, R. E. *J. Phys. Chem.* **1991**, *95*, 7564.

(61) Lahamer, A.; Ying, Z. C.; Haufler, R. E.; Hettich, R. L.; Compton, R. N. *Adv. Metal Semiconductor Clusters* **1998**, *4*, 179.

(62) Shinohara, H. *Adv. Metal Semiconductor Clusters* **1998**, *4*, 205.

(63) Guo, B. C.; Kearns, K. P.; Castleman, A. W., Jr. *Science* **1992**, *255*, 1411.

(64) Guo, B. C.; Wei, S.; Purnell, J.; Buzza, S.; Castleman, A. W., Jr. *Science* **1992**, *256*, 515.

(65) Wei, S.; Guo, B. C.; Purnell, J.; Buzza, S.; Castleman, A. W., Jr. *Science* **1992**, *256*.

(66) Wei, S.; Guo, B. C.; Purnell, J.; Buzza, S.; Castleman, A. W., Jr. *J. Phys. Chem.* **1992**, *96*, 4166.

(67) Cartier, S. F.; Chen, Z. Y.; Walder, G. J.; Sleppy, C. R.; Castleman, A. W., Jr. *Science* **1993**, *260*, 195.

(68) Guo, B. C.; Castleman, A. W., Jr. *Adv. Metal Semiconductor Clusters* **1994**, *2*, 137.

(69) Pilgrim, J. S.; Duncan, M. A. *J. Am. Chem. Soc.* **1993**, *115*, 9724.

(70) Pilgrim, J. S.; Duncan, M. A. *J. Am. Chem. Soc.* **1993**, *115*, 6958.

(71) Pilgrim, J. S.; Duncan, M. A. *J. Am. Chem. Soc.* **1993**, *115*, 4395.

(72) Pilgrim, J. S.; Duncan, M. A. *International Journal of Mass Spectrometry and Ion Processes* **1994**, *138*, 283.

(73) Pilgrim, J. S.; Brock, L. R.; Duncan, M. A. *J. Phys. Chem.* **1995**, *99*, 544.

(74) Brock, L. R.; Duncan, M. A. *J. Phys. Chem.* **1996**, *100*, 5654.

(75) Reddic, J. E.; Duncan, M. A. *Chem. Phys. Lett.* **1997**, *264*, 157.

(76) von Helden, G.; Tielens, A. C. G. M.; van Heijnsbergen, D.; Duncan, M. A.; Hony, S.; Waters, L. B. F. M.; Meijer, G. *Science* **2000**, *288*, 313.

(77) Heijnsbergen, D.; Duncan, M. A.; Meijer, G.; von Helden, G. *Chem. Phys. Lett.* **2001**, *349*, 220.

(78) von Helden, G.; van Heijnsbergen, D.; Duncan, M. A.; Meijer, G. *Chem. Phys. Lett.* **2001**, *333*, 350.

(79) Buchanan, J. W.; Reddic, J. E.; Grieves, G. A.; Duncan, M. A. *J. Phys. Chem. A* **1998**, *102*, 6390.

(80) Buchanan, J. W.; Grieves, G. A.; Flynn, N. D.; Duncan, M. A. *Int. J. Mass Spectrom.* **1999**, *187*, 617.

(81) Buchanan, J. W.; Grieves, G. A.; Reddic, J. E.; Duncan, M. A. *Int. J. Mass Spectrom.* **1999**, *183*, 323.

(82) Foster, N. R.; Grieves, G. A.; Buchanan, J. W.; Flynn, N. D.; Duncan, M. A. *J. Phys. Chem. A* **2000**, *104*, 11055.

(83) Duncan, M. A.; Knight, A. M.; Negishi, Y.; Nagao, S.; Judai, K.; Nakajima, A.; Kaya, K. *J. Phys. Chem. A* **2001**, *105*, 10093.

(84) Ayers, T. M.; Westlake, B. C.; Duncan, M. A. *J. Phys. Chem. A* **2004**, *108*, 9805.

(85) Rohmer, M. M.; Benard, M. *Chem. Rev.* **2000**, *100*, 495.

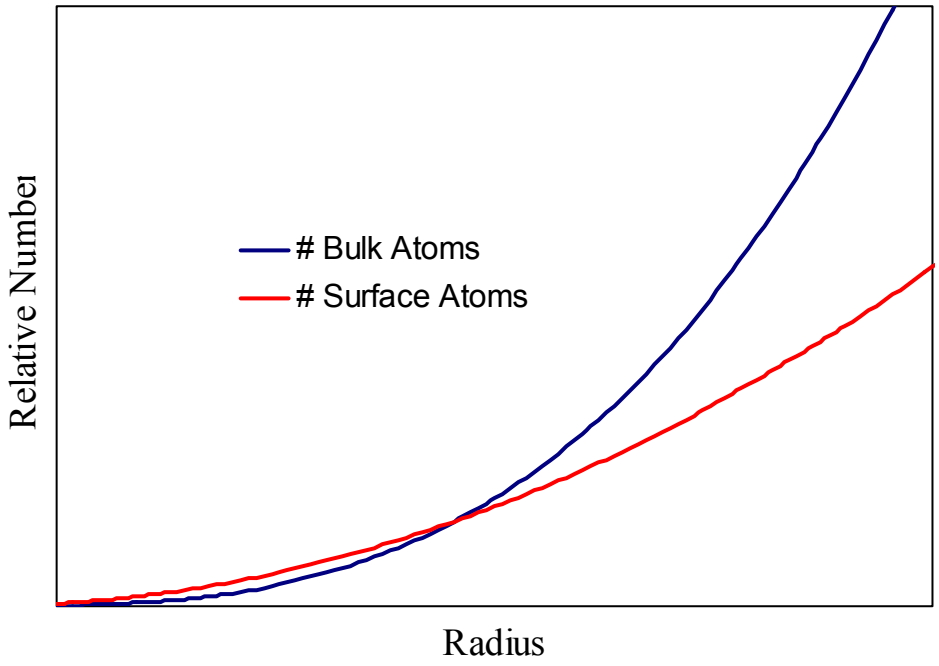

Figure 1. A plot of surface area (# surface atoms) and volume (# bulk atoms) as a function of the radius of a particle.

CHAPTER 2

EXPERIMENTAL

2.1 LASER DESORPTION APPARATUS

Laser desorption and vaporization experiments described within this thesis are performed on a linear time-of-flight mass spectrometer. A schematic of our linear time-of-flight mass spectrometer is depicted in Figure 1. The instrument described here is homemade, but moderately priced commercial instruments are also available.[1,2] The samples analyzed are solid powders that are pressed into a 1/8 in. dia. hole on the end of a stainless steel probe tip or solutions which are dried on the surface of a flat stainless steel probe tip. Unlike matrix assisted laser desorption ionization time-of-flight (MALDI-TOF) mass spectrometry, no matrix is used in these experiments. Once inside the mass spectrometer, the chosen sample is vaporized and ionized using repeated pulses (10 Hz) from the focused output (20 cm lens) of a Nd:YAG laser (Continuum MiniLite) operating at either 532 or 355 nm. The fluence of the laser is adjusted with a variable attenuator and/or iris diaphragm prior to focusing to optimize production of the desired clusters, so that energies less than 1 mJ/pulse are employed for most of these experiments. The laser focal point can be moved periodically to different positions on the probe tip to sample fresh material. The alignment of the desorption laser on the sample is monitored with a small video camera (Watec WAT-902C) equipped with a zoom lens and this is displayed on an eight-inch black and white video monitor (Ultrak KM-9). High acceleration voltages (up to 15 kV) and delayed-pulsed ion extraction are implemented for improved mass resolution.[3] The operating pressure in the mass spectrometer ion source is about $1x10^{-7}$ torr.

The laser vaporization technique has long been utilized to produce clusters of metals, non-metals and metal compounds in the gas phase.[4-7] However, the processes by which atoms or molecules are vaporized from solid precursors and how clusters grow are not completely understood. High temperature plasmas are generated by focusing a pulsed laser onto a solid

sample. These plasmas contain a variety of species including neutrals, ions, and electrons. Processes involving the vaporization of atoms followed by three-body recombination or direct vaporization of molecular species are both possible, and one or the other of these may dominate depending on the material studied. In molecular beam experiments, a collision gas such as argon or helium is present to aide in cooling and cluster growth.[4] Absent the collision gas, atomic vapor must condense without multiple collisions, but this may also occur in elements that produce high atomic vapor densities.[7]

The mechanism of ionization in laser vaporization experiments is also not well understood. Clusters may grow from atomic ions or neutral species, with neutrals later becoming ionized through collisions with electrons generated in the laser plasma. The latter process is least probable, since the electrons needed for the ionization process will be depleted rapidly thru electrostatic attraction with the acceleration voltages. Photoionization is a possible method of ionization but is unlikely to be efficient. The energies available from the photons produced by the lasers employed for vaporization are low in comparison to ionization energies. Multiphoton processes are also highly improbable. The photons necessary for the ionization process are only present for a 3-5 nanoseconds and cluster growth is likely a much slower process (100 nsec-microsecond time scale).

The cluster cations that form are accelerated down the flight tube by the electric fields created by the repeller plate, the draw-out grid and the plate defining the beginning of the flight tube. While in the flight tube, the ions separate according to their mass given by the following equation,

$$KE = zeV = \tfrac{1}{2}mv^2 \qquad (1)$$

where KE = kinetic energy, z = the charge of the particle, and eV = the potential difference between the repeller and draw-out-grid. Because all ions receive the same kinetic energy, the velocity of each ion will be inversely proportional to the square root of its mass. Ions are subsequently detected at the end of the flight tube using a standard electron multiplier tube. Signals are collected and averaged with a digital oscilloscope (LeCroy LT 341) and transferred to a PC via an IEEE-488 interface for processing. The time-of-flight measurement begins with the laser pulse, which forms ions almost instantaneously, and the synch-out pulse from the laser triggers the oscilloscope trace. Traces of ion signal pulses versus time are accumulated by summing the results of 10-20 laser shots with a frequency of 1 Hz. Time traces are converted to mass spectra by squaring the time axis values and multiplying by an instrument constant derived from an appropriate calibration mass sample.

Many experiments were also reproduced using a commercial time-of-flight instrument (Bruker "Autoflex") and identical cluster distributions were obtained in all spectra of cationic species. The Bruker instrument has a clear advantage in mass resolution over home-made instruments. However, it uses a nitrogen laser (337 nm) for the vaporization and ionization processes and this is not as efficient as our Nd:YAG laser in desorbing most metal containing samples[8,9] due to its low output power (10-20 μJ/pulse).

2.2 LASER VAPORIZATION FLOWTUBE APPARATUS

The laser vaporization flow reactor (LVFR) used in our laboratory was designed following schematics of a previous instrument built by Andres and coworkers (Figure 2).[10,11] Using an oven cluster source, the Andres group was able to isolate ligand-coated gold clusters using a flow apparatus where the ligands were inserted downstream of the cluster source.[12] We expanded on this

concept by using a more general laser vaporization cluster source, while employing the proven method demonstrated by Andres for cluster passivation and recovery.

An illustration of the LVFR constructed in our laboratory is presented in Figure 3. It consists of a laser vaporization cluster source using an excimer laser (Lambda Physik Compex 110) that has a high output power (300 mJ/pulse) at the KrF wavelength (248 nm) and a high repetition rate (100 Hz) for efficient production of high average metal vapor densities. The vaporization laser has such high power that it can be loosely focused in a rectangular spot about 1x10 mm in dimension and still have enough intensity to ablate transition metal targets. A continuous expansion of argon or helium gas for collisional quenching and cooling of the laser generated vapor flows over the sample surface and entrains the metal vapor into a flow which travels down a 1.5 inch diameter tube. The pressure in the flow-tube when the experiment is in operation is 20-60 torr. Immediately downstream (about 20 cm from the vaporization point) the metal vapor and clusters which form in the flow-tube reach the passivation zone, where ligands and/or solvents (e.g., amines, alkanethiols, etc.) can be injected either directly as vapor or as an aerosol using a nebulizer spray (Misonix "Micromist"). Beyond the passivation zone a cold trap is utilized for isolating the passivated clusters. The cold trap consists of a standard two-neck 500 mL round-bottom flask immersed in liquid nitrogen and filled with ¼ inch diameter glass beads so that the flowing gas encounters many cold surfaces before exiting the trap to the pump. The cold trap can be sealed for removal without exposure of the samples to air. In the experiments described here, 30-60 minute runs yield milligram samples which are sufficient for mass spectrometry analysis.

After isolation, samples are sealed under argon until they can be analyzed.. A critical aspect of this research is the analysis of samples, which is done using the laser desorption time-of-flight mass spectrometer discussed in section 3.1. For mass spectrometry, one or two drops of solution are

applied to a 5 mm dia. stainless steel probe tip, which is then dried under an argon purge and inserted through a vacuum interlock into the mass spectrometer vacuum system. The Nd:YAG laser used for vaporization and ionization in the analysis of samples collected using the LVFR is attenuated greatly to limit sample fragmentation.

2.3 REFERENCES

(1) Comstock, Inc., 2006; Vol. 2006.

(2) R. M. Jordan Company, Inc., 2006; Vol. 2006.

(3) Wiley, W. C.; Mclaren, I. H. *Rev. Sci. Instrum.* **1955**, *26*, 1150.

(4) Dietz, T. G.; Duncan, M. A.; Powers, D. E.; Smalley, R. E. *J. Chem. Phys.* **1981**, *74*, 6511.

(5) *Clusters of Atoms and Molecules I: Theory, Experiment, and Clusters of Atoms*; Haberland, H., Ed.; Springer-Verlag: Berlin, 1995, pp 422.

(6) Johnston, R. L. *Atomic and Molecular Clusters*; Taylor & Francis: New York, 2002.

(7) McElvaney, S. W.; Nelson, H. H.; Baronavski, A. P.; Watson, C. H.; Eyler, J. R. *Chem. Phys. Lett.* **1987**, *134*, 214.

(8) Ayers, T. M.; Westlake, B. C.; Duncan, M. A. *J. Phys. Chem. A* **2004**, *108*, 9805.

(9) Ayers, T. M.; Westlake, B. C.; Preda, D. V.; Scott, L. T.; Duncan, M. A. *Organometallics* **2005**, *24*, 4573.

(10) Bowles, R. S.; Kolstad, J. J.; Calo, J. M.; Andres, R. P. *Surf. Sci.* **1981**, *106*, 117.

(11) Mahoney, W.; Andres, R. P. *Mater. Sci. Eng. A* **1995**, *A204*, 160.

(12) Mahoney, W.; Kempe, M. D.; Andres, R. P. *Mater. Res. Soc. Symp. Proc.* **1996**, *400*, 65.

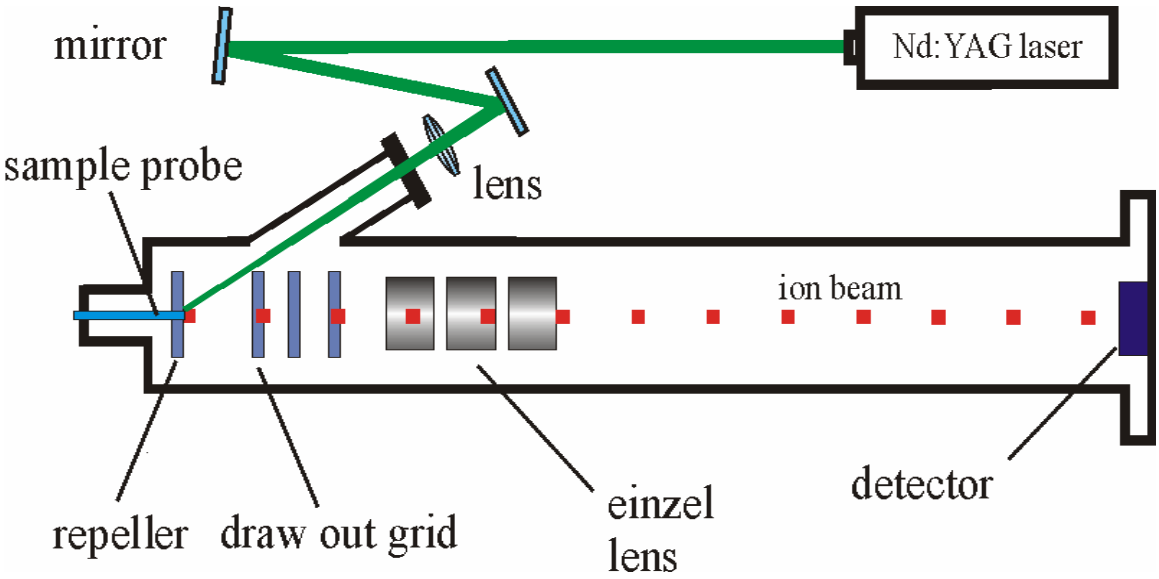

Figure 1. Schematic of a laser desorption time-of-flight mass spectrometer. An Nd:YAG laser is used as the vaporization and ionization source.

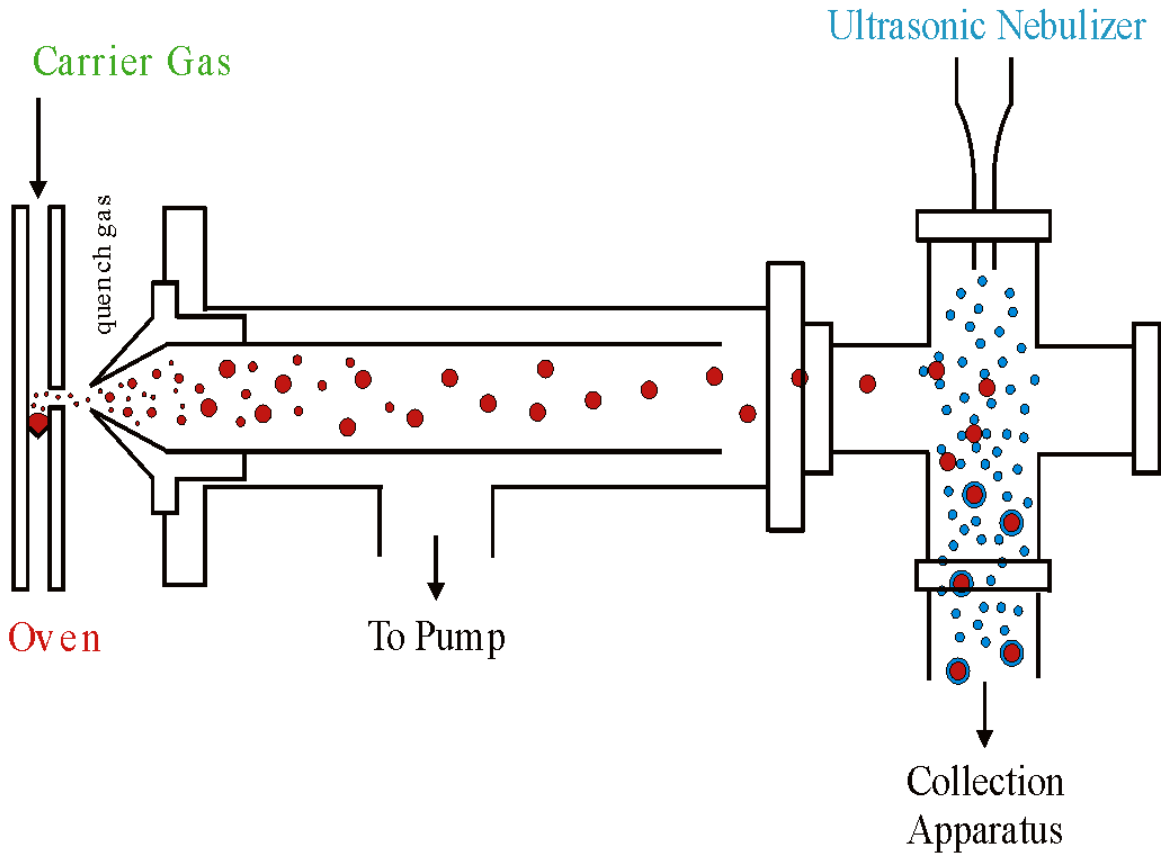

Figure 2. LVFR constructed by Andres and coworkers which utilizes an oven cluster source.

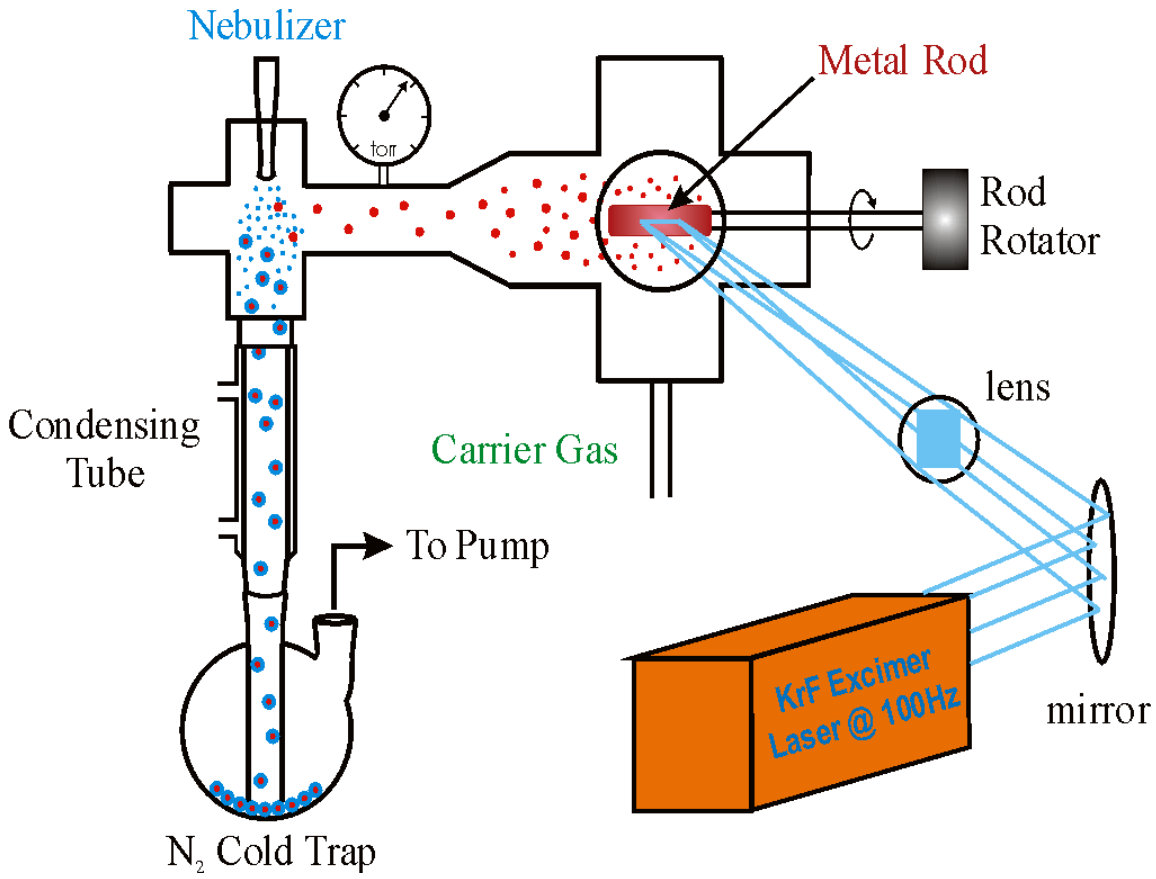

Figure 3. LVFR as initially constructed in the Duncan laboratory.

CHAPTER 3

CLUSTER EDUCATION

3.1 BACKGROUND

Mass spectrometry is one of the oldest and most common analytical techniques employed in industrial, government and university laboratories. This technique has become invaluable for the detection and identification of compounds throughout chemistry. Fortunately, there are a wide variety of mass spectrometers from which to choose, depending on the application. Time-of-flight (TOF) instruments like those employed for this laboratory possess many advantages over other forms of mass spectrometry.[1] These instruments are relatively simple in design and inexpensive to produce. Furthermore, the principles of operation are straightforward and consequently can be conveyed to undergraduate students without difficulty. As demonstrated here, a TOF instrument can be combined with a laser vaporization ion source to produce unusual mass spectra of atomic nanoclusters.

Time-of-flight mass spectrometry is used for many different applications in chemistry. It is often coupled with matrix assisted laser desorption ionization (MALDI), which has become one of the most popular methods for the detection of biomolecules such as amino acids, enzymes and proteins. MALDI makes it possible to ionize these species with little fragmentation, and time-of-flight mass spectrometry provides the necessary high mass range for detection of these species. Several examples of undergraduate experiments using MALDI are reported in the literature.[2-4] In contrast to MALDI, the laser desorption time-of-flight experiments discussed in this article focus on the vaporization of inorganic materials and the growth of cluster species from their gas phase atoms. Like biological species, nanoclusters have high molecular masses, and a TOF instrument is ideally suited to analyze these materials. We present here examples of inorganic and organic clusters, produced through direct laser vaporization of powder samples with a pulsed Nd:YAG laser, which are detected with a basic time-of-flight mass spectrometer.

Sulfur, phosphorus, bismuth, and an indium-sulfur mixture all produce unusual mass spectra and cluster growth patterns. Furthermore, each system illustrates interesting chemical bonding concepts.

3.2 EXPERIMENTAL AND SAFETY

The laser desorption/ionization time-of-flight mass spectrometer used in these experiments is described in Chapter 3.1. In the laser desorption experiments here, the samples are solid powders that are pressed into a 1/8 in. dia. hole on the end of a stainless steel rod probe tip. In the case of the indium-sulfur experiment, the powders are mixed in a 1:1 ratio by mass. Unlike MALDI-TOF mass spectrometry, no matrix is used in these experiments. Once inside the mass spectrometer, the chosen sample is vaporized and ionized using repeated pulses (2 Hz) from the focused output (20 cm lens) of a Nd:YAG laser (Continuum MiniLite) operating at either 532 or 355 nm. The fluence of the laser is adjusted with a variable attenuator and/or iris diaphragm prior to focusing to optimize production of the desired clusters, so that energies less than 1 mJ/pulse are employed for most of these experiments.

The main hazards associated with this lab include exposure to laser light and to high voltages associated with the mass spectrometer. The instructor in charge should have completed appropriate safety training for laser usage. With careful preparation, student exposure to the laser can be minimized so that similar training is not required for them. The instructor should align the laser into the mass spectrometer and subsequently cover the laser beam path with appropriate boxes, beam blocks or curtains to enclose the main beam and its scattered light. The second area of concern involves the high voltages used on the mass spectrometer. In commercial instruments, high voltage cables are enclosed, but in homemade instruments this is not always

the case. Students are warned against touching any cable or connector associated with the power supplies. Last, but equally important, is the proper handling of the chemicals used in this laboratory. Students should be required to access MSDS forms related to this laboratory and identify hazards and proper disposal of the chemicals used.

3.3 INORGANIC CLUSTERS

Sulfur

Figure 2 shows the mass spectra measured for both cations (bottom) and anions (top) when a sulfur powder sample is vaporized with the laser at 355 nm. Sulfur cluster cations of the form S_n^+, for n = 2-8, are observed with appreciable intensity. There is essentially no signal for the S^+ atomic ion, but the S_2^+ and S_5^+ mass peaks are quite prominent. The mass spectrum extends out to S_8^+ with good intensity, but the larger cluster ions, S_9^+ and S_{10}^+, are much smaller by comparison. The anion mass spectrum is noticeably different from that for the cations. Only the mass peaks for n = 1-4 are observed, with S_3^- being by far the most intense. These observations agree with previous results reported by Johnson and coworkers.[15]

The interpretation of these mass spectra should stimulate speculation about what exact atomic or molecular species are desorbed. In particular, it is interesting to consider whether there is growth of larger species and whether or not there is fragmentation in the desorption/ionization process. It is well-known that solid sulfur primarily contains the S_8 allotrope,[16] although approximately thirty other allotropes have been reported.[17] It is therefore possible that the laser vaporization process produces significant amounts of molecular S_8 which are desorbed directly into the gas phase. It is then conceivable that the spectrum observed represents a series of masses resulting from the ionization of fragmentation products from this

molecular species. However, another possibility is that desorbed sulfur atoms recombine to form these clusters, and that the growth processes end at about the S_8 species. Unfortunately, there is no way of determining from these experiments which is the predominant mechanism of cluster production, nor can we exclude either process. However, either mechanism suggests the likely importance of eight-membered rings in the gas phase cations. It is interesting to note that these results for sulfur cation clusters vary noticeably from corresponding experiments reported by Martin and coworkers.[18] In this earlier work, the clusters were formed by heating the powder in an oven source followed by quenching the vapor in helium gas and ionizing it with electron impact. In that case, masses corresponding to multiples of the S_8 species were observed. It is perhaps understandable that different vapor production methods and ionization processes would lead to different mass spectral patterns.

It is tempting to conclude that the most prominent ions in the two spectra, S_5^+ and S_3^-, result from fragmentation of the S_8 allotrope by direct dissociation of ion-pairs, since S_5^+ plus S_3^- equals S_8. This same mechanism was in fact suggested by Johnson and coworkers.[15] However, an ion-pair dissociation mechanism like this requires an extremely high energy and is usually not efficient. It is more likely that growth and fragmentation processes are different for anions and cations, and that the prominent stoichiometries represent those that are relatively more stable. For example, in the cluster cation mass spectrum of tellurium (isoelectronic to sulfur), the same prominent ions at M_2^+ and M_5^+ are found.[19] This suggests that the number of electrons present in these species plays an important role in their stability. The details of ion formation and cluster growth in laser vaporization processes are not well understood, and therefore speculation about these processes is entirely acceptable. Students should be encouraged to propose structures and bonding configurations for both the prominent cation and anion species to attempt to rationalize

why certain clusters are produced more efficiently. In particular, they should notice and question why all the most prominent clusters in this study (S_3^-, S_2^+ and S_5^+) have an *odd* number of total electrons.

Phosphorus

A mass spectrum obtained by the vaporization of red phosphorus powder is presented in Figure 3. Other research groups have performed similar laser desorption experiments on phosphorous and have obtained similar results.[20,21] Unlike sulfur, phosphorus forms much larger clusters in these laser vaporization experiments; ions as large as P_{51}^+ are observed. The most interesting details in this spectrum are the prominence of the P_3^+, P_4^+, P_5^+ and P_7^+ ions and the strong preference for the formation of odd numbered cation species that begins after a cluster size of n = 11.

As always, we consider growth from vaporized atoms versus desorption of larger intact molecular species. Since the red phosphorus crystal structure is primarily made of polymeric phosphorus chains,[22] it is tempting to conclude that the phosphorus clusters are produced by direct desorption and ionization of these large chain-like structures. However, it unlikely that long phosphorus chains could be desorbed efficiently in this way. These chains are likely to be entangled in the solid matrix with significant interactions (van der Waals) with the solid structure. Therefore, desorption of atoms or small molecules, which would require the breaking of fewer bonds, seems more likely. On the other hand, it remains difficult to understand how such large clusters could grow on the timescale of the vaporization process without a collision gas present. Distributions of large phosphorus clusters have been observed previously by Martin and coworkers[23] and were interpreted to grow from atomic vapor. Additionally, McElvaney and

coworkers have shown that large clusters of other elements can grow efficiently without an added collisional gas.[12] If enough vapor density can be produced in the vaporization process, there can be enough atom-atom and atom-molecule collisions to promote large cluster growth.

The most interesting issue raised here is the preference for odd numbered over even numbered phosphorus cluster cations, where P_7^+ is the most prominent of these. This situation is in fact often found in cluster science, and it is now recognized that there is usually an increased stability for clusters that have an even number of valence electrons.[23] Having an even number of valence electrons ensures that all electrons are paired. In the case of phosphorus, electron pairing can only occur for a cation cluster that has an odd number of atoms. However, while this rule explains the preference for odd-numbered clusters, it does not explain the prominence of the P_3^+, P_5^+ and P_7^+ ions compared to other odd-numbered species. Popular electron counting rules found in the Polyhedral Skeletal Electron Pair Theory, also known as Wade's Rules, may offer an explanation.[24,25] These rules relate the number of skeletal electrons in many clusters of the main group elements to specific polyhedral structures with delocalized electron clouds in their interior volumes that provide enhanced stability through three-dimensional aromaticity. Clusters that are electron deficient are able to achieve added stability by more extensive sharing of electrons in this way. The bonding in these clusters only involves valence electrons in the *p* orbitals, and an *N*-atom cluster achieves stable electron configurations when there are $2N + 2$, $2N + 4$ or $2N + 6$ skeletal electrons, representing the "closo," "nido" and "arachno" polyhedral structures, respectively. P_3^+, P_5^+ and P_7^+, which have 8, 14 and 20 valence electrons respectively, meet the criteria for "closo," "nido" and "arachno" structures, providing these three specific cluster cations with an increased stability. The same behavior has been observed previously in experiments involving antimony and bismuth,[26] which are also group VA elements. Further

theoretical research has been employed in order to explain the stability of both small and larger phosphorus cluster cations.[20,27,28] However, no experiments have been reported that were able to measure and confirm any proposed structures.

Students should be able to compare and contrast the sulfur and phosphorus spectra and understand that although the two elements are side by side on the periodic table, their properties can be dramatically different. A multitude of allotropes exist for both elements, however, those of phosphorus are polymeric crystalline structures, whereas, those of sulfur are typically cyclic molecular crystalline structures.[29] Consequently, the clusters sulfur and phosphorus produce in a laser plasma are dramatically different.

Bismuth Oxide

A mass spectrum of bismuth oxide cluster cations (bottom) and anions (top) is presented in Figure 5. Our group[30] as well as others[31] have observed similar mass spectra previously for these systems. The most fascinating observation in these spectra is that the metal oxide stoichiometries generated in the laser plasma are not purely random or statistical. A variety of possible oxide stoichiometries are simply not observed. Instead, for each number of bismuth atoms there is one specific metal oxide stoichiometry detected (e.g. $Bi_3O_4^+$). This apparent stoichiometric preference must be related to either the geometric or electronic stability of these particular cluster sizes.[30] Additional insight is provided by a comparison of the corresponding cation and anion spectra. If only geometric effects are important, clusters containing the same number of bismuth atoms should exhibit the same oxide stoichiometry, i.e., the stoichiometry should be charge-independent. However, if the specific number of bonding electrons is more important, clusters containing the same number of bismuth atoms might have different oxide

stoichiometries depending on the charge. Inspection of the mass spectra for cations and anions reveals that the latter case is true. Different oxides are observed for the same number of bismuth atoms throughout the two spectra (e.g. $Bi_3O_4^+$ versus $Bi_3O_5^-$). Electronic stabilization is therefore apparently the primary consideration here. Students should be encouraged to explain these oxide patterns in terms of specific bonding configurations for each of the atoms in these clusters. As discussed previously,[30] reasonable configurations can be obtained in terms of M-O-M network structures having localized two-electron bonds everywhere. Wade's Rules are not necessary here, since there is a balance in the number of electrons between bismuth and oxygen in the stoichiometries seen. As in the case of phosphorus, delocalized bonding occurs primarily for electron deficient systems.

Indium Sulfur

A mass spectrum of indium-sulfur mixed clusters is presented in Figure 4. A thorough literature search reveals that no other research group has reported these clusters previously. Similar to the case of bismuth oxide clusters, only specific stoichiometries are observed in the mass spectrum. If one looks closely at the stoichiometries represented in the spectrum, a pattern becomes visible. The number of sulfur atoms in the cluster is often two less than the number of indium atoms. For the smaller clusters, In_3S^+ and $In_3S_2^+$ are both prominent as are $In_5S_3^+$ and $In_5S_4^+$. At larger sizes, $In_7S_5^+$ and $In_7S_6^+$ are detected with comparable intensity, as are $In_9S_7^+$ and $In_9S_8^+$. Surprisingly, no cluster cations are detected that have an even number of indium atoms.

If consideration is given to the valence *p* electrons for indium and sulfur, then each of the prominent indium-sulfur clusters observed in the spectrum has an even number of electrons as a

cation. Because sulfur has four valence *p* electrons, an odd-number of indium atoms produces an overall even number of electrons in cation clusters, perhaps explaining the preference for clusters containing an odd number of indium atoms. However, there are many other stoichiometries containing an odd number of indium atoms that would also have an overall even number of electrons that are not observed in this experiment.

If we try to treat these systems like we did for the bismuth oxide clusters, we find that there are not enough electrons to provide two-electron bonds and reasonable oxidation states throughout all the atoms. Wade's Rules also fails to explain the apparent stability of the smaller clusters. The In_3S^+ species, for example, is highly deficient with a valence count of 2N-2 *p* electrons. However, it is possible to rationalize the bonding in this species using a simple Lewis dot structure as shown below:

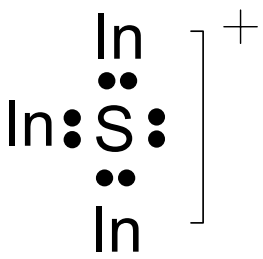

However, this structure makes sense if only the *p* electrons are considered for indium.

$In_3S_2^+$ and $In_5S_3^+$ have a count of 2N electrons. Wade's Rules therefore also fails to explain the stability of these systems. However, in the larger clusters the electron counting configurations fit better in the scheme of Wade's Rules. For example, $In_5S_4^+$ has a 2N+2 "closo" electron count and $In_7S_5^+$, $In_7S_6^+$ and $In_9S_7^+$ all have 2N+4 "closo" configurations. Thus, the idea of delocalized shared electron clouds exemplified by Wade's Rules can also be used to rationalize the stability of the larger indium-sulfide cluster cations.

3.4 CONCLUSIONS

The experiments described here show how laser vaporization in a time-of-flight mass spectrometer can be employed to explore a variety of inorganic nanocluster systems. By the conclusion of this laboratory, undergraduates will have been exposed to vacuum systems, lasers and pulsed-timing electronics that are utilized in this kind of experiment. By sampling a variety of materials, students will find that the stoichiometry of inorganic clusters grown within a laser plasma can vary greatly depending on an element's chemistry. Systems like sulfur, may produce small molecular clusters, whereas others, like phosphorus, may produce very large distributions of clusters. The bismuth oxide and the indium sulfur experiments illustrate how inorganic compounds can prefer different stoichiometries depending on the size and electronic configuration of the cluster. In some cases (bismuth oxide), there is a balance of electron density and the stoichiometries can be explained via localized two-electron bonding. In other systems that are electron deficient (phosphorous, larger indium-sulfides) there is a tendency for delocalized bonding and more extensive electron sharing. The electron counting rules can help to rationalize the clusters seen. Finally, in other systems (small indium-sulfides), the explanation for specific abundant clusters remains elusive. These experiments provide valuable exposure to modern instrumentation and an introduction to concepts and issues now important in inorganic nanocluster chemistry.

3.5 REFERENCES

(1) Cotter, R. J. *Time-of-Flight Mass Spectrometry: Instrumentation and Applications in Biological Research*; American Chemical Society: Washington D.C., 1997.

(2) Muddiman, D. C.; Bakhtiar, R.; Hofstadler, S. A.; Smith, R. D. *J. Chem. Ed.* **1997**, *74*, 1288.

(3) Counterman, A. E.; Thompson, M. S.; Clemmer, D. E. *J. Chem. Ed.* **2003**, *80*, 177.

(4) Reimann, C. T.; Mie, A.; Nilsson, C.; Cohen, A. *J. Chem. Ed.* **2005**, *82*, 1215.

(5) Cornett, D. S.; Amster, I. J.; Duncan, M. A.; Rao, A. M.; Eklund, P. C. *J. Phys. Chem.* **1993**, *97*, 5036.

(6) Comstock, Inc., 2006; Vol. 2006.

(7) R. M. Jordan Company, Inc., 2006; Vol. 2006.

(8) Wiley, W. C.; Mclaren, I. H. *Rev. Sci. Instrum.* **1955**, *26*, 1150.

(9) Dietz, T. G.; Duncan, M. A.; Powers, D. E.; Smalley, R. E. *J. Chem. Phys.* **1981**, *74*, 6511.

(10) *Clusters of Atoms and Molecules I: Theory, Experiment, and Clusters of Atoms*; Haberland, H., Ed.; Springer-Verlag: Berlin, 1995, pp 422.

(11) Johnston, R. L. *Atomic and Molecular Clusters*; Taylor & Francis: New York, 2002.

(12) McElvaney, S. W.; Nelson, H. H.; Baronavski, A. P.; Watson, C. H.; Eyler, J. R. *Chem. Phys. Lett.* **1987**, *134*, 214.

(13) Ayers, T. M.; Westlake, B. C.; Duncan, M. A. *J. Phys. Chem. A* **2004**, *108*, 9805.

(14) Ayers, T. M.; Westlake, B. C.; Preda, D. V.; Scott, L. T.; Duncan, M. A. *Organometallics* **2005**, *24*, 4573.

(15) Hearley, A. K.; Johnson, B. F. G.; McIndoe, J. S.; Tuck, D. G. *Inorg. Chim. Acta* **2002**, *334*, 105.

(16) Steudel, R.; Holz, B. *Z. Naturforsch., B: Chem. Sci.* **1988**, *43*, 581.

(17) Steudel, R.; Eckert, B. *Top. Curr. Chem.* **2003**, *230*, 1.

(18) Martin, T. P. *Angew. Chem. Int. Edit.* **1986**, *25*, 197.

(19) Willey, K. F.; Cheng, P. Y.; Taylor, T. G.; Bishop, M. B.; Duncan, M. A. *J. Phys. Chem.* **1990**, *94*, 1544.

(20) Chen, M. D.; Li, J. T.; Huang, R. B.; Zheng, L. S.; Au, C. T. *Chem. Phys. Lett.* **1999**, *305*, 439.

(21) Bulgakov, A. V.; Bobrenok, O. F.; Kosyakov, V. I. *Chem. Phys. Lett.* **2000**, *320*, 19.

(22) Corbridge, D. E. C. *The Structural Chemistry of Phosphorus*; Elsevier Scientific Publishing Co.: Amsterdam, 1974.

(23) Martin, T. P. *Zeitschrift fur Physik D - Atoms, Molecules and Clusters* **1986**, *3*, 211.

(24) Wade, K. *Adv. Inorg. Chem. Radiochem.* **1976**, *18*, 1.

(25) Cotton, F. A.; Wilkinson, G.; Murillo, C.; Bochmann, M. *Advanced Inorganic Chemistry, 6th ed.*; John Wiley & Sons, Inc.: New York, 1999.

(26) Geusic, M. E.; Freeman, R. R.; Duncan, M. A. *J. Chem. Phys.* **1988**, *89*, 223.

(27) Baird, N. C. *Can. J. Chem.* **1984**, *62*, 341.

(28) Chen, M. D.; Huang, R. B.; Zheng, L. S.; Zhang, Q. E.; Au, C. T. *Chem. Phys. Lett.* **2000**, *325*, 22.

(29) *Elemental Sulfur*; Meyer, B., Ed.; John Wiley & Sons: New York, 1965, pp 390.

(30) France, M. R.; Buchanan, J. W.; Robinson, J. C.; Pullins, S. H.; Tucker, J. L.; King, R. B.; Duncan, M. A. *J. Phys. Chem. A* **1997**, *101*, 6214.

(31) Struyf, H.; van Vaeck, L.; van Grieken, R. *Rapid Commun. Mass Sp.* **1996**, *10*, 551.

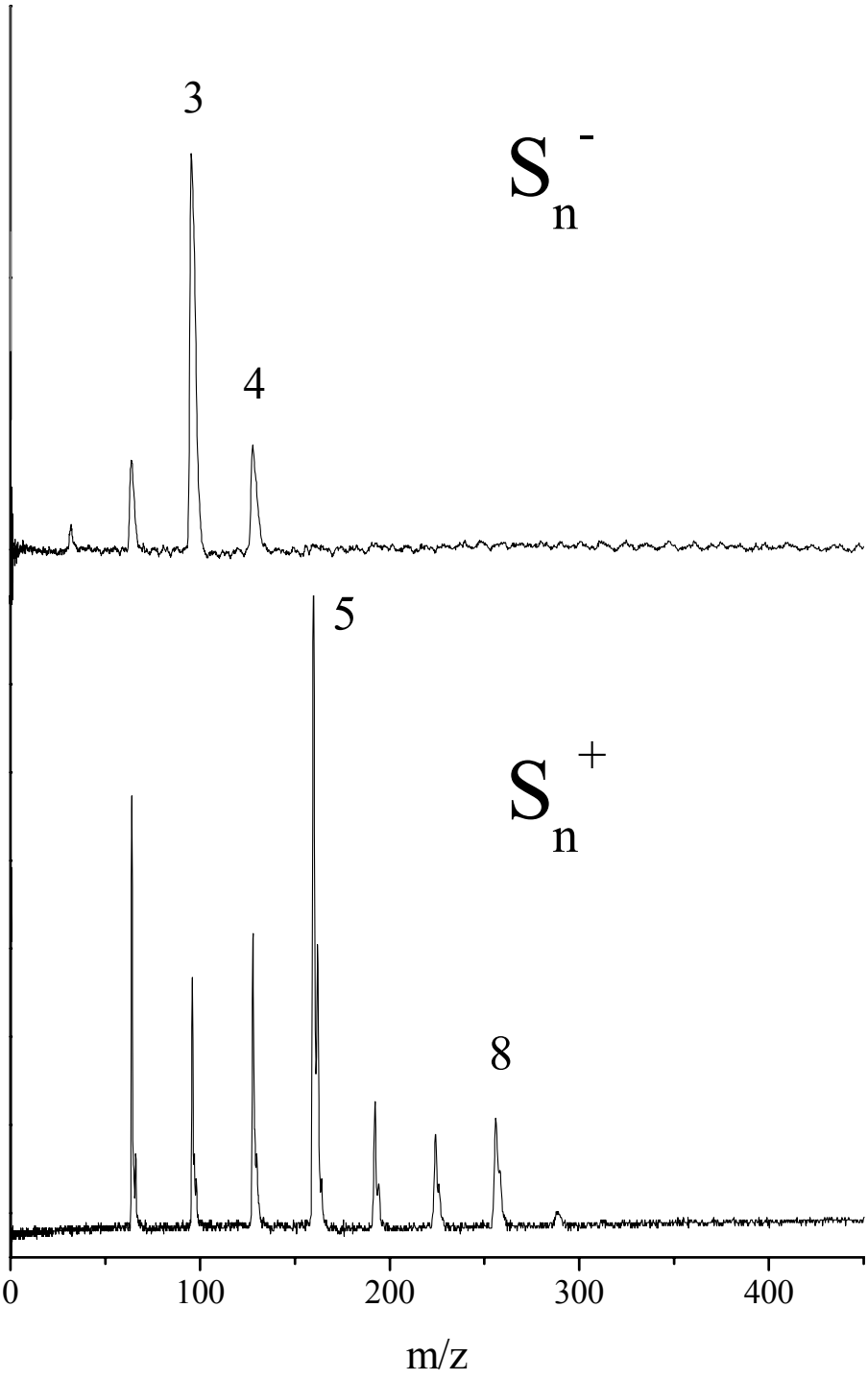

Figure 1. Mass spectra of sulfur cluster cations (bottom) and anions (top) using 355 nm laser vaporization.

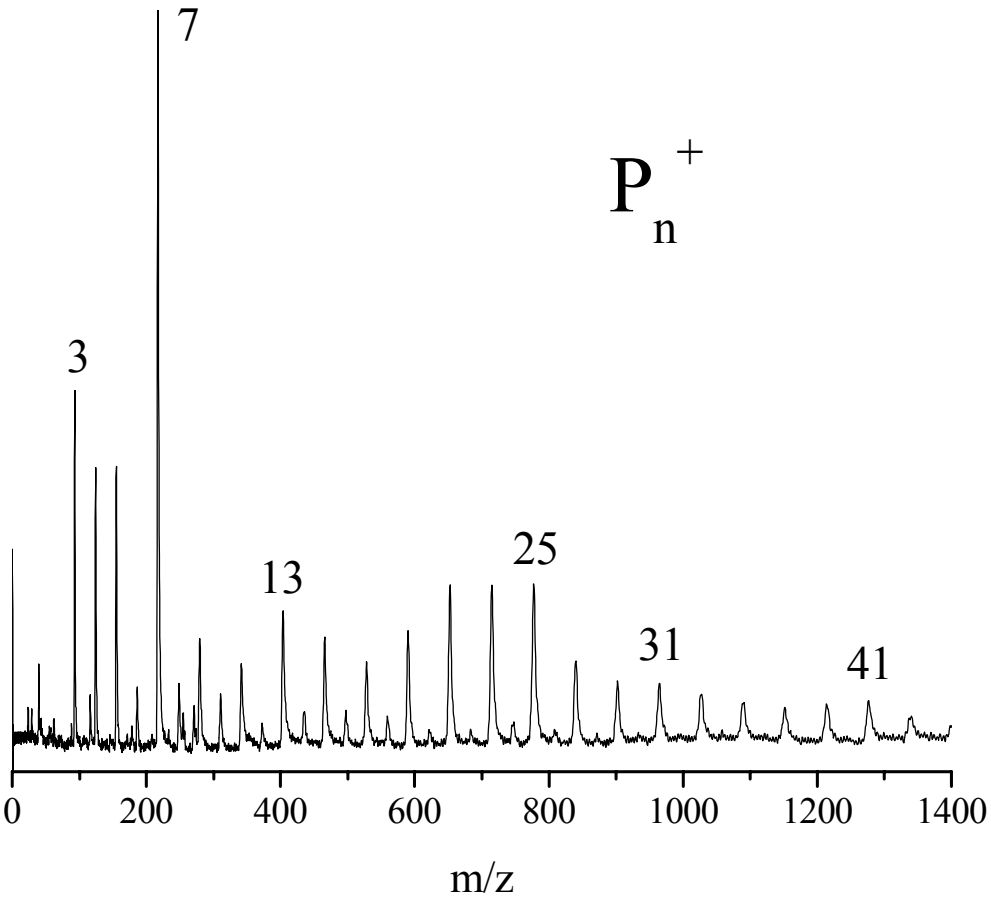

Figure 2. Mass spectrum of phosphorus clusters obtained using 355 nm laser vaporization.

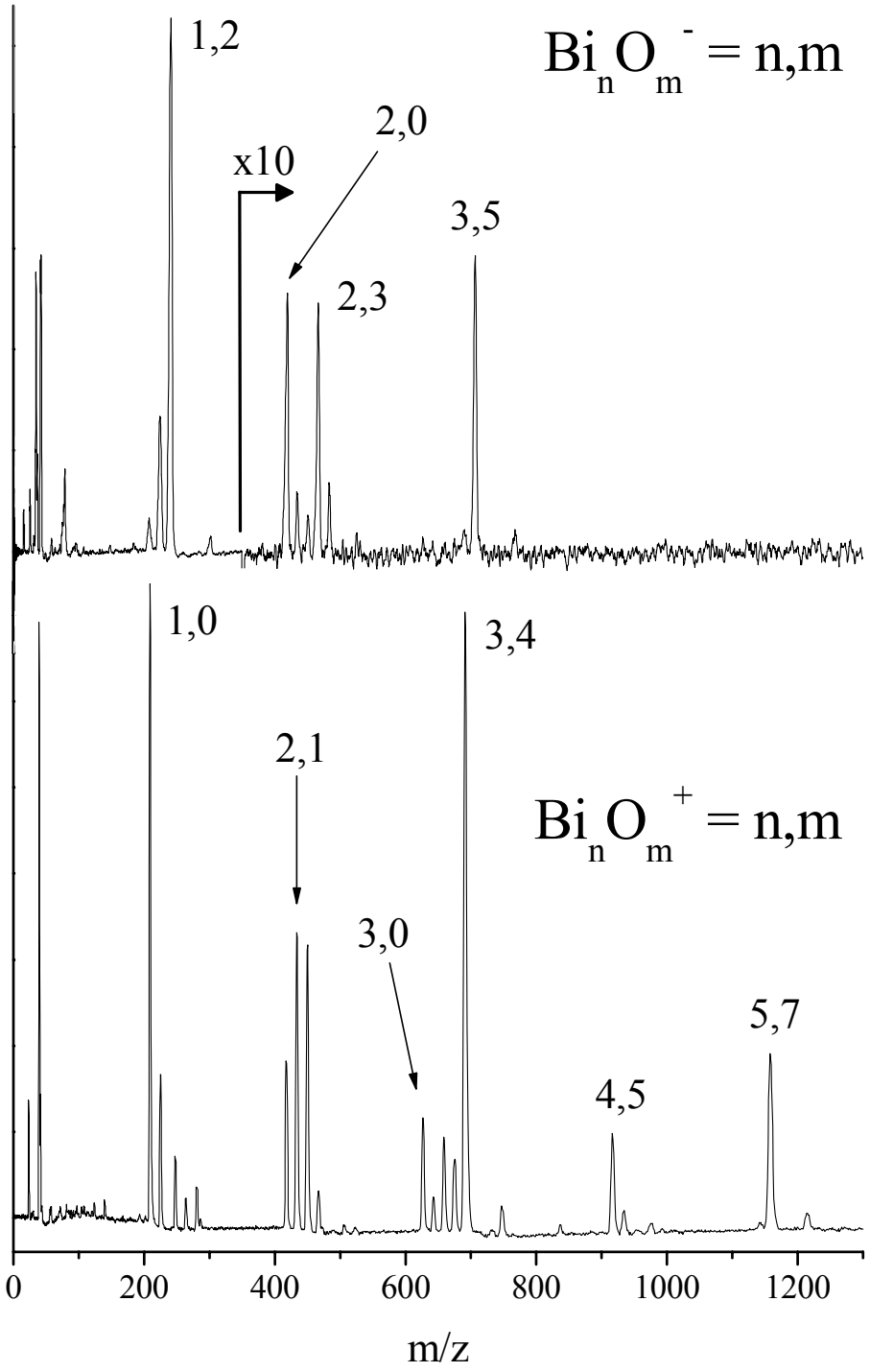

Figure 3. Mass spectra of bismuth oxide cluster cations (bottom) and anions (top) obtained from an oxidized sample of pure bismuth using 532 nm laser vaporization.

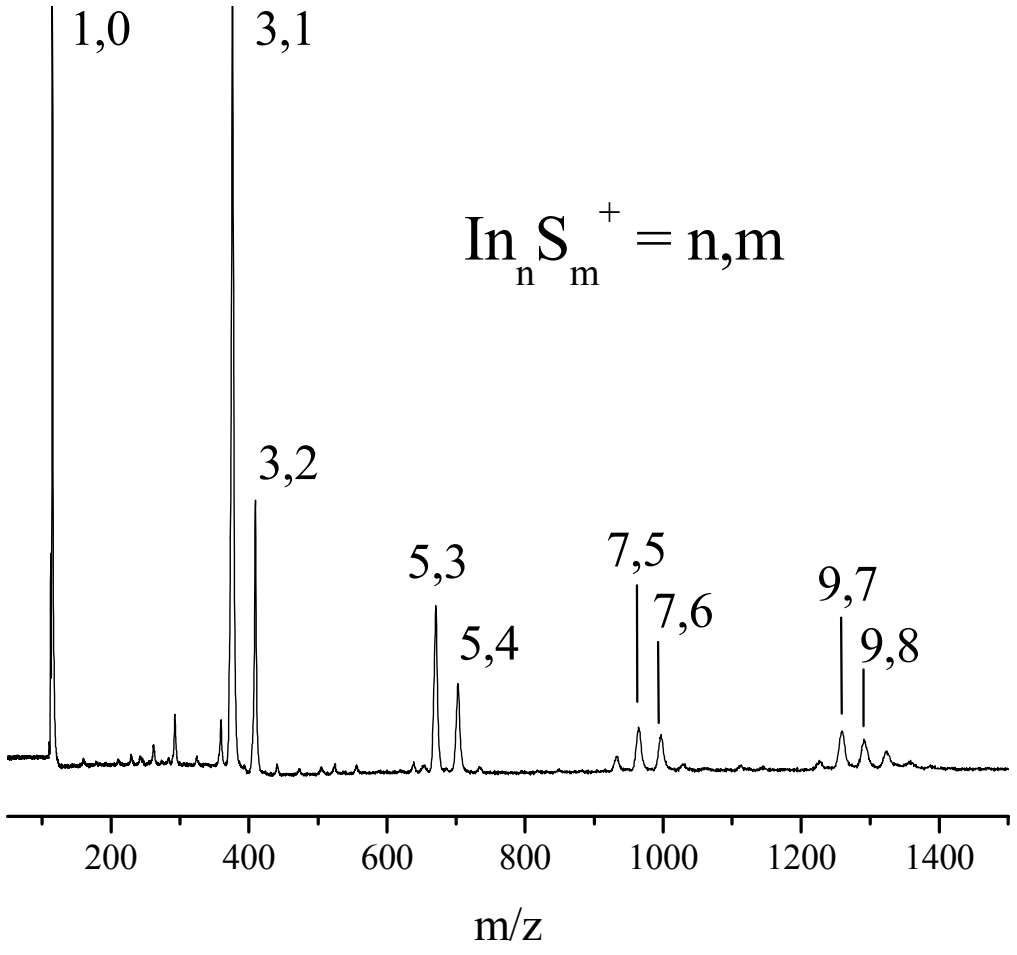

Figure 4. Mass spectrum resulting from the covaporization of an indium and sulfur mixture using 532 nm laser vaporization.

CHAPTER 4

TRANSITION METAL – PAH COMPLEXES

4.1 BACKGROUND

New techniques for metal vapor production and ligand aggregation schemes have made it possible to produce a fascinating variety of metal-aromatic complexes in the gas phase.[1] Clusters and complexes synthesized in these environments include metal-polycyclic aromatic hydrocarbon (PAH) complexes,[2-8] metal-fullerene complexes,[8-14] multi-metal coated fullerenes[15-19] and transition metal-aromatic multi-decker sandwich networks.[20-28] Although numerous examples of metal-aromatic complexes have been described, there is still much to learn about the structure and bonding of these systems. In this chapter, we describe the production of a variety of metal complexes with the planar PAH molecules coronene ($C_{24}H_{12}$) and pyrene ($C_{16}H_{10}$), as well as the bowl-shaped corannulene molecule ($C_{20}H_{10}$).[29-32]

PAH's occur naturally in environments wherever carbon is found. They are primarily formed in combustion processes including the burning of fossil fuels, forest fires and cigarettes. Many PAH's are known carcinogens and have been linked to cancers of the respiratory and digestive systems.[33,34] Due to their prevalence in nature, the properties of PAH molecules have been explored extensively. The absorption, fluorescence and phosphorescence of gas phase PAH molecules and thin films are well documented.[35-37] In astrophysics, PAH's have been implicated as components of dust grains in the interstellar medium (ISM). Ionized PAH's and metal-PAH complexes have also been suggested as possible carriers of the optical diffuse interstellar bands (DIB's)[38-43] and the unidentified infrared bands (UIB's).[43-46]

Theoretical models of intercalated graphite and carbon nanotubes often use PAH's to represent a finite section of the carbon surface.[47-50] Specifically, coronene is the smallest PAH molecule that possesses the essential structural elements of graphite. Some of the most important catalytic processes involve metal atoms or clusters attached to supports. Metal atoms

and/or clusters bonded to the surface of a PAH molecule can provide models of such supported catalysts. Residual metal from the catalysts employed for carbon nanotube synthesis affect the binding of nanotubes in bundles, and metal binding to nanotube walls will be necessary to make wire connections in carbon nanotube circuits. Metal-PAH complexes also provide convenient models for these processes.[47,50] There is also evidence that metal-PAH complexes may be constituents of interstellar gas clouds; they have been implicated in the depletion of atomic metal and silicon in the ISM[51] and as contributors to the DIB's and UIB's.[52]

Increasing interest in metal-PAH systems has thus motivated many groups to produce these species in laboratory experiments. Dunbar and coworkers were the first to observe metal-PAH ion complexes in gas phase experiments using FT-ICR mass spectrometry.[53] From these experiments, they determined the binding kinetics of a variety of metal and nonmetal cations with PAH's. Our group has produced a variety of metal and multimetal-PAH sandwich complexes using laser vaporization of film-coated metal samples in a molecular beam cluster source.[2-5] Competitive binding and photodissociation experiments were successful in determining structural information and relative bonding strengths of metals with benzene, C_{60} and coronene.[8] Experimental work has stimulated new theoretical studies investigating metal binding sites and bond energies on PAH's. Dunbar,[54] Klippenstein and coworkers,[55] and Jena and coworkers[56,57] have been active in this area.

Coronene is a symmetrical, planar molecule composed of seven aromatic rings (Figure 1). NMR ring currents have indicated that electron density lies primarily on alternating outside rings.[58] Likewise, the four aromatic rings in pyrene (Figure 1) are also not equivalent, with the highest electron density lying in the outer rings.[59] Therefore binding of electron accepting

species may occur at these sites, and furthermore, binding of electron donating species may occur at the remaining outside ring sites and the center ring which are electron deficient.

Corannulene can be viewed as one third of a C_{60} molecule with the perimeter carbons terminated with hydrogens [Figure 1]. Scott and coworkers discovered a simple and efficient synthetic route to corannulene,[31,32] allowing for thorough exploration of its properties. Corannulene's unique bowl shape offers a variety of bonding possibilities for metal cations. Both η^5 and η^6 ring sites exist on the concave and convex sides of the molecule. Recent theoretical studies have shown that there is little preference for transition metal binding to the convex versus the concave sides of the molecule,[54,57] in part because there is a low activation energy (0.43 eV) for bowl inversion.[60] However, cation binding to outside-ring η^6 sites is clearly preferred over binding to the central η^5 site. Several examples of synthetic inorganic complexes with corannulene derivatives illustrate this bonding preference.[61-63] Bohme and coworkers have recently studied the reactivity of a variety of ligands with the iron-corannulene complex using a selected ion flowtube apparatus.[64] On the macroscale, Siegel and coworkers grew co-crystal polymeric arrays of silver perchlorate and other silver salts with corannulene.[65] However, the bonds formed between silver and corannulene in the crystal are readily broken when this material is re-dissolved into solution. To our knowledge, the only other examples of metal-corannulene complexes that have been synthesized or reported in gas phase experiments are those of Scott and coworkers.[66] The present work explores a general methodology for producing metal-PAH ion-molecule complexes that may facilitate further studies of their properties.

4.2 EXPERIMENTAL

The metal powders studied in this experiment consist of the first row transition metals titanium and chromium of varying grain sizes (Aldrich, Alfa Aesar). No care is taken to prevent

these metals from oxidizing since it is also of interest to study metal oxide complexes with PAH's. Uranium is used as a representative of the actinide series; the source of uranium is the salt uranyl acetate, $UO_2(CH_3CO_2)_2 \cdot 2H_2O$. The organometallic tested is iron cyclopentadienyl benzene $[Fe(cp)(bz)]PF_6$. Sodium and potassium cations are present as impurities in some experiments resulting from the handling of samples. Corannulene samples needed for this experiment were synthesized and purified by Scott and coworkers using previously described synthetic techniques.[32] Coronene (cor), $C_{24}H_{12}$, and pyrene [67], $C_{16}H_{10}$, are used as received without further purification (Aldrich, Alfa Aesar). All spectra were recorded using the basic methodology presented in Chapter 3.1.

4.3 RESULTS AND DISCUSSION

Transition Metal Powders + PAH

To explore a potentially facile method for the production of metal-PAH complexes, we investigated co-vaporization of samples composed of pure metal powder mixed with PAH powder. These experiments were carried out on all of the first-row transition metals with coronene and selected experiments were also done with pyrene and corannulene. Figure 2 shows a representative mass spectrum obtained from the vaporization (532 nm) of chromium/coronene powder (upper trace) and chromium powder mixed with both pyrene and coronene (1:1 molar). Several atomic ions are present in the low mass range of these spectra (not shown), including sodium, potassium, aluminum, and chromium (sodium and potassium are common impurities in many laser desorption experiments). The aluminum comes from the sample probe tip used in this experiment. No sodium- or potassium-PAH complexes were observed, but aluminum-PAH complexes are formed in addition to the desired chromium complexes. In both spectra,

chromium-PAH mono-ligand and di-ligand complexes are present in large abundance. The di-ligand complexes here are presumed to be sandwiches because only small amounts of PAH dimers are observed without metal. Very little fragmentation of the PAH species is observed, probably because of the low laser power (0.5-1.0 mJ/pulse) used for these experiments. The only coronene fragment detected in this spectrum corresponds to the loss of one C_2 unit. This fragment ion is observed in nearly all experiments. The small intensity peak assigned as $Cr^+(cor)_2 - C_2$ could conceivably be assigned to an $Al^+(cor)_2$ complex, because these two ions differ by only one amu. However, this peak is also observed in other experiments using different sample probes when no aluminum is present. It is therefore assigned to the chromium sandwich fragment ion. Results similar to these chromium data are obtained for other transition metals, except that the efficiency of complex formation varies with the metal, as discussed below. We tried experiments using either the 532 nm or 355 nm output of the YAG laser for vaporization, but obtained useable signals only with the 532 nm wavelength. This was not an issue of laser power, because a wide variety of pulse energies were explored for both 532 and 355 nm. The 532 nm excitation worked best at lower laser pulse energy (0.5-1.0 mJ/pulse), and 355 nm excitation did not produce comparable results at any pulse energy level. At higher pulse energies, metal ions were detected, but complexes did not form efficiently, presumably because the plasma conditions were too hot.

Chromium shows no preference for forming coronene versus pyrene complexes, as the relative ion abundances are virtually equivalent for the Cr^{+67} and $Cr^+(cor)$ ions. The same holds true for both chromium coronene and pyrene homo-ligand sandwich complexes and the $Cr^{+67}(cor)$ mixed-ligand sandwich. Unlike our previous molecular beam experiments on chromium-coronene complexes,[4] we observe no multiple-metal complexes here with either

coronene or pyrene and no complexes with more than two PAH molecules. In the molecular beam experiments, we employed a metal rod sample which was coated with a sublimed film of coronene. This film-coated rod sample was mounted in a normal laser vaporization cluster source with a pulsed nozzle expansion gas, and complexes were allowed to grow in a channel extending beyond the vaporization position. The present configuration has no expansion gas and no growth channel. The only opportunity for metal-PAH collisions is in the plume from the vaporization, where conditions are substantially hotter than room temperature. It is therefore understandable that smaller complexes, on average, result from the present conditions. Also, due to these conditions we expect that any complexes which do form must have substantial bond energies. The complexes produced here are similar to those reported by Dunbar in FT-ICR experiments, where metal ions produced by laser vaporization were reacted with PAH vapor.[53,68]

In the spectrum shown in Figure 2, aluminum-PAH mono-ligand complexes are observed to form in amounts comparable to the chromium-PAH complexes. However, while good intensities are observed for di-ligand (sandwich) complexes of chromium, no such sandwich complexes are observed for aluminum. Dunbar and coworkers also reported that Al-coronene and Mg-coronene cations did not form sandwiches in their FT-ICR experiments.[53,68] This surprising observation can be understood by consideration of the binding tendencies and bond energies observed previously for many other ion-molecule complexes of aluminum and magnesium. The unusual clustering behavior of these cations was first investigated in theoretical studies by Bauschlicher and coworkers.[69-72] Their calculations suggested that di-ligand complexes for these ions with small molecules such as water or carbon dioxide would be bent instead of linear. This trend arises because the binding in Al^+ and Mg^+ ligands complexes is primarily electrostatic and the 3s electrons on Al^+ and Mg^+ are highly polarizable. Table 1

presents a list of metal cation-benzene binding energies obtained from collision induced dissociation experiments by Armentrout and coworkers.[73-75] With the exception of the manganese cation, magnesium cation has a lower binding energy to benzene than any of the 1st row transition metal cations. This is indication that the Mg^+(bz) binding is primarily electrostatic in nature.

When the first ligand binds to a magnesium or aluminum cation, it induces a charge polarization, pushing electron density toward the opposite side of the metal ion. Since the bonding in these complexes is primarily electrostatic, additional ligands are repelled by this back-side negative region, and tend to bind more on the same side of the cation as the first. Recent infrared photodissociation experiments performed by our group on $M^+(CO_2)_n$, M = Al or Mg, complexes found vibrational spectra consistent with those predicted for such bent structures.[76,77] Infrared spectra revealed that the $M^+(CO_2)_2$ complex is bent (C_{2v}) and the $M^+(CO_2)_3$ complex has a trigonal pyramid structure. Likewise, Nishi and coworkers recently observed similar bent structures for $Mg^+(H_2O)_n$ complexes.[78,79] Following this same kind of logic, the binding of a PAH π cloud to Mg^+ or Al^+ should polarize these cations in the same way. If this polarization occurs, then a negative charge region would form on the metal ion on the side opposite the first PAH. In the PAH systems, however, the steric hindrance prevents binding of a second ligand on the same side of the cation as the first. The negative charge repels the second PAH, and therefore di-ligand complexes cannot form efficiently.

Figure 3 shows a graph summarizing the tendency for different transition metal ions to form mono-ligand and di-ligand complexes with coronene in these studies. A similar plot would be obtained for the selected metal-pyrene complexes studied. In all of these experiments, the intensity of the PAH cation mass peak is 2-3 times greater than that of any of the metal

containing ion peaks. We can therefore assume that PAH concentration is not a limiting factor in these studies. However, metal ion concentration may vary from one system to another because of the different laser ablation efficiencies for different metals and their yield for ions as opposed to neutrals. The relative amounts of the complex ions are therefore normalized to the intensities of the respective atomic ion mass peaks for each metal. After this scaling, the relative amounts of the complexes shown in the figure can be associated approximately with the tendency for each metal ion to form complexes. For both the early transition metals, titanium through chromium, and the late transition metals, nickel and cobalt, both mono-ligand complexes and sandwiches were produced with good abundance. Manganese produced an abundance of the mono-ligand complex, but no sandwich was observed for this metal. Also to our surprise, no iron or cobalt complexes with coronene were observed by this method, even though large amounts of the atomic cations were produced. In contrast to this result, $Fe^+(cor)_{1,2}$ and $Co^+(cor)_{1,2}$ complexes were produced in large abundance in our molecular beam experiments.[2,8] Likewise, similar experiments combining iron or cobalt powders with pyrene also produced no complexes.

The main difference between these studies and the molecular beam work is that a pulsed nozzle expansion gas is present in the molecular beam experiments. This collision gas can stabilize more weakly bound complexes. It is therefore interesting to consider if the iron and cobalt complexes are not seen here because they are too weakly bound to survive under the rather hot growth conditions. Bond energies for transition metal cation complexes with PAH species are not generally available. However, in our previous experiments using competitive ligand binding, we estimated that the bond energy for $Fe^+(cor)$ was greater than 48 kcal/mol.[8] To compare the binding energy of iron to those of other transition metal ions, we use the theoretical results of Klippenstein.[80] Figure 3 compares the complex binding tendencies to the binding

energies calculated for M^+(cor) mono-ligand complexes. The calculated binding energies follow a trend not unlike those seen for other metal ion-ligand complexes, with a minimum in bond energy for the Mn^+ complex.[80] However, we find significant amounts of Mn^+(cor) in our experiment. For the problematic metals, iron has a lower binding energy than some other metals, but its binding energy to coronene is still predicted to be substantial, consistent with our previous experiment. On the other hand, cobalt ion has one of the highest predicted binding energies to coronene. Therefore, it does not seem that binding energy trends can explain the poor yields for iron and cobalt complexes. Additionally, even for the other metals that form complexes, the tendency to bind to coronene does not track with the relative bond energies that are calculated. Apparently, the kinetics and dynamics in the plasma growth process are also quite important in the yield of complexes by this method.

Figure 4 shows a representative mass spectrum obtained from the vaporization (532 nm) of a mixed powder sample containing chromium and corannulene (upper trace) and chromium powder mixed with both corannulene and pyrene (lower trace). Only one atomic ion, chromium, is present in abundance in both spectra. Normally sodium and potassium atomic ions are present as a result of sample handling, however, no significant amounts are present in any of the spectra presented here. Also present in large abundance are chromium-PAH mono-ligand and di-ligand complexes. The di-ligand complexes here are presumed to be sandwiches because the PAH dimer intensities are always smaller in abundance than corresponding $M^+(PAH)_2$ intensities. Results similar to the chromium data are obtained for other transition metals (e.g. vanadium and cobalt); the efficiency of complex formation varies with the metal used as shown in the results for metal coronene. Again, we tried experiments using both the 532 nm and 355 nm outputs of the YAG laser for vaporization, but obtained useable signals only with the 532 nm wavelength.

A wide variety of pulse energies were explored for both wavelengths, indicating that this was not an issue of power. Though 355 nm vaporization produced corannulene and corannulene dimer ions in large abundance, it was not successful in producing transition metal cations efficiently, which consequently prevents formation of metal-corannulene complexes. 532 nm vaporization performed best at low pulse energies (0.5 – 1.0 mJ/pulse). At higher pulse energies, metal ions were detected, but complexes did not form efficiently, presumably because plasma conditions were too hot for efficient condensation reactions.

As shown in the lower trace, complexes are produced that contain either corannulene or pyrene as well as the mixed complexes containing both corannulene and pyrene, i.e., Cr^{+67}(cora). As in the coronene and pyrene experiments described previously, chromium shows no obvious preference for forming corannulene versus pyrene complexes, though the relative abundances in the spectrum presented are not equivalent for the $Cr^{+67}{}_n$ and $Cr^{+}(cora)_n$ ions. Experiments which varied the relative amounts of each PAH did show larger abundances for corannulene complexes versus pyrene complexes (not shown), although it is difficult to be quantitative about this trend because the vaporization efficiency of the organics cannot be determined. In contrast to previous molecular beam experiments on transition metal-PAH complexes,[2-6] we observe no multiple-metal complexes here with either corannulene or pyrene and the production of complexes with more than two PAH molecules is inefficient.

Transition Metal Salts + PAH

To further investigate the clustering behavior of iron and cobalt, experiments were performed with vaporization of *metal salts* instead of pure metal powders in mixtures with the PAH's. Figure 5 shows a representative mass spectrum for the covaporization of $FeCl_2 \cdot 4H_2O$

with coronene (lower trace), and a similar spectrum resulting from the covaporization of $CoCl_2 \cdot 6H_2O$ with pyrene (upper trace). As indicated, both metal salt experiments produced PAH mono- and di-ligand complexes efficiently. In addition to the complexes with the bare metal ions, *metal chloride*-PAH complexes are also produced for both systems. Higher laser power is required for these experiments, which produces carbon fragment ions above and below the mass of coronene and coronene dimer (near 600 amu). These fragments are also seen without metal whenever high laser power is employed. There is thus a significant difference in the tendency to make the desired metal-PAH complexes depending on the source of the metal. Because the overall concentrations of metal and PAH are comparable in the pure metal versus metal salt experiments, there must be some difference in the reactivity of the metal species produced in these different experiments. To investigate this further, we must consider the mechanism of growth of these complexes under our conditions.

The laser vaporization/ablation process is well known to produce both neutral and ionized species of both metal and organics. However, there is no post-ionization in our experiment, and we measure only the ions that are produced directly. The complexes can result from the combination of metal cations with neutral PAH species, or vice-versa. The electrostatic interactions are much favored for the former case, due to the ionization potential differences between the metals and the PAH species. It is conceivable that complexes could form initially as neutrals and then be ionized by an electron collision in the plasma. However, electron mobility is much greater than atomic or molecular values, and therefore the density of electrons in the growth region with enough energy to ionize drops very quickly because of the acceleration fields present. Likewise, photoionization of neutral complexes is also unlikely because of the low photon energy at 532 nm and because of the laser pulse duration (5 nsec), which is short

compared to the movement of atoms and molecules. In our previous molecular beam experiments, ionization of neutral PAH complexes produced much lower signal levels than direct sampling of cations.[20-24] Therefore, the most likely mechanism for complex growth here is the combination of metal cations with neutral PAH species. We should therefore focus on the possible differences between cobalt and iron metal ions produced directly by metal vaporization as opposed to those produced by vaporization of metal salts.

The most obvious difference between metal ions produced from pure metal or metal salts is the oxidation state in the precursor material. If metal cations from salts are produced in higher charge states, then it would not be surprising that these ions would have a stronger attraction for PAH surfaces and therefore be more reactive. However, there is no evidence in any of these mass spectra for doubly charged metal ions. It is noticeable that the metal salt samples provide higher yields of singly charged metal, but the yield of metal ion in the neutral powder experiments was large enough so that we could have seen complexes. The next possible issue is the *electronic state* of the metal cations produced. It is well known in transition metal ion-molecule chemistry that reactivity can depend dramatically on the electronic state of the cations.[81-85] In particular, Fe^+ and Co^+ produced by various ionization methods are known to exist in a distribution of ground and excited states, and some of the excited states are metastable so that they survive for long periods. Fe^+ has the d^6s^1 (^6D) ground state, with relatively low lying ^4F and ^4D excited states, while Co^+ has a d^8 (^3F) ground state and low-lying ^5F and ^3F excited states. In both cases, state specific studies show that the excited states are much more reactive than the ground states.[81-85] A simple explanation for our experiment, therefore, is that metal powder vaporization produces larger quantities of ground state metal ions, while metal salt vaporization produces higher yields of the more reactive excited states. It is not clear why these

trends would occur, but it might be possible to test this hypothesis with emission experiments on these plasmas. In light of this result, it is also apparent that the distribution of metal ion electronic states generated in the laser vaporization process and the relative reactivity of these states probably affect all of the metal-PAH complex growth processes. This helps to explain why the tendencies to form complexes do not follow the same trend as complex binding energies.

Another interesting observation is that metal chloride-PAH complexes are formed in the metal salt experiments. Figure 5 shows clearly the presence of $FeCl^+$(cor), $CoCl^+$[67] and Co_2Cl^+(cor) mono-ligand complexes. There are also large signals for $M^+(PAH)_2$ sandwiches, and even some small signals for $M_2^+(cor)_2$ sandwiches. However, no $MCl^+(PAH)_2$ sandwich ions are detected. This behavior is apparently similar to the situation discussed previously, where no $Al^+(PAH)_2$ sandwiches are observed, and a similar explanation makes sense here too. The first PAH molecule would most likely bind to the positive end of the metal chloride ion, i.e., on the metal. This places the negative chlorine on the side of the MCl^+ species opposite the PAH. If a sandwich species is to form, the second PAH must approach the metal center from this side, and it encounters the strong negative region of the chlorine. The negatively charged chlorine would interact repulsively with the π-cloud of the PAH, in much the same way suggested for the negatively charged region of polarized Al^+ ions. The chloride species effectively limits sandwich growth by providing an unfavorable bonding interaction to the second ligand.

Transition Metal Oxides and Carbides + PAH

If the mechanism discussed for inhibition of sandwich growth is valid, then other metal compounds that exhibit ionic bonding should behave in the same way. We therefore decided to examine the clustering behavior of metal oxides or carbides with PAH systems. The early transition metals, titanium, vanadium and zirconium, produce metal oxide-PAH complexes efficiently in these experiments. Figure 6 shows mass spectra obtained using titanium oxide or zirconium carbide powders in mixtures with coronene. In the upper frame, titanium and various titanium oxide ions are prevalent at low masses. Both titanium mono-ligand complexes and sandwiches are observed. The most abundant complex produced is the titanium oxide mono-ligand complex, TiO^+(cor). Other oxide complexes are also seen corresponding to the stoichiometries $Ti_2O_x^+$(cor), with x = 1-3. Like the chlorides, however, there are no oxide sandwiches. The data in the lower frame was acquired by covaporizing zirconium carbide and coronene. Surprisingly, there is no indication for any zirconium carbide cluster ion formation. Instead, the ions occurring at low masses include zirconium and zirconium oxide. Apparently, the oxygen comes from gas adsorbed on the surface of the powder samples, which were handled in air. In contrast to the titanium oxide system, the most abundant mono-ligand complex formed here is the bare metal Zr^+(cor) complex. Other zirconium oxide complexes are formed with the stoichiometry ZrO_x(cor), with x =1,2. The last prominent mass appearing in the spectrum corresponds to the $Zr^+(cor)_2$ sandwich. As seen for the chloride systems above, there is no evidence here for oxide sandwiches. Similar behavior is found (data not shown) for iron and vanadium oxide clustering with coronene.

The early first row transition metals titanium and vanadium also produce metal oxide-corannulene complexes efficiently. Figure 7 shows a mass spectrum obtained using titanium powder mixed with corannulene. Titanium and various titanium oxide ions are prevalent at low

masses. Both titanium mono-ligand and di-ligand complexes are observed, as are prominent adducts with Na^+, even though the sodium is only present as an impurity. However, the most abundant complex produced is the titanium oxide mono-ligand complex, TiO^+(cora). The abundance of this ion can be rationalized to some degree because of the higher concentration of TiO^+ compared to Ti^+. Additionally, it is likely that the metal oxide ion, which has partial ionic Ti^{2+},O^- or Ti^{3+},O^{2-} character and a strong dipole moment, has a higher affinity for the organic π cloud than the bare metal ion. In contrast to these intensities observed for mono-ligand complexes, the spectrum shows a much larger abundance for the $Ti^+(cora)_2$ di-ligand complex compared to that for the metal oxide ion.

The clustering behavior of oxide species with these PAH systems follows the same pattern that we saw with aluminum and the metal chlorides. The negative end of the metal oxide apparently behaves in the same way as the chlorides or the polarized valence electron cloud of aluminum, inhibiting the addition of a second PAH molecule. Another related observation is that these trends apply not only for MO^+ diatomics, but also for larger oxides. Titanium and iron produced small amounts of *multimetal* oxide complexes such as Fe_2O^+-cor, and $Ti_2O_x^+$-cor, for x = 1-3. Again, no multimetal oxide sandwiches are observed in either experiment. With these multiple metal oxides, it is natural to wonder if both metals are bound to the same side of coronene, as opposed to two additions of metal and/or oxide on opposite sides of the ring system. Likewise, if binding occurs on the same side of the PAH, are the metals connected or bound separately at different ring sites? However, the same multimetal oxide stoichiometries are observed in the mass spectrum without the PAH present. Therefore, it is likely that they exist first in the gas phase and then are bound to the PAH as a single unit. This also makes sense in light of the strong metal oxide bonding. Titanium and iron oxide bond energies are 159.8

kcal/mol and 78.4 kcal/mol respectively,[62] which is much greater than the calculated titanium and iron binding energies to coronene (52.1 kcal/mol and 56.0 kcal/mol respectively),[68,80] or the iron binding to corannulene. The simplest assumption then is that the metal oxide attaches as a single unit to the PAH molecule.

Lanthanides and Actinides + PAH

To investigate other interesting metals and their oxides, we examined neodymium and uranium as representatives of the lanthanide and actinide metals. Figure 8 shows the mass spectra for experiments on the covaporization of neodymium oxide and pyrene (upper trace) and on the covaporization of uranyl acetate and pyrene. Large amounts of atomic metal and oxide ions are produced in both spectra. Pure metal mono-ligand complexes and sandwich species are observed for both neodymium and uranium. Mono-ligand metal oxide-PAH complexes, $MO^+(PAH)$, are prevalent in these spectra, like those observed for titanium, vanadium, and zirconium. However, one major difference between the rare earths and transition metal species becomes apparent. Significant amounts of metal oxide-PAH sandwich complexes, $MO^+(PAH)_2$, are observed for both neodymium and uranium.

Figure 9 shows the mass spectrum for covaporization experiments of uranyl acetate and corannulene. Large amounts of atomic uranium and uranium oxide ions are produced in the low mass range as well as the complex ion, uranium oxide acetate [$UO^+(OAc)$]. Mono-corannulene complexes of these low mass range ions are also observed; the abundances of the smaller uranium ions correlate well with the abundances of mono-corannulene complexes produced. Uranium-corannulene di-ligand complexes are produced, however, the abundances observed do not match the abundances of the small mass range uranium ions as seen for the mono-

corannulene complexes. In this series, pure metal di-corannulene, $U^+(cora)_2$, is the most abundant ion with uranium oxide corannulene di-ligand ions, $UO^+(cora)_2$, occurring in lower abundance. As in the case of the transition metal oxide complexes, the exposed oxygen from the metal oxide-corannulene adduct apparently inhibits the binding of additional corannulene molecules.

It is interesting to consider why oxide PAH sandwiches form in these experiments, while those of the transition metals do not. A possible explanation for this behavior lies in the different ionic radii of the metals, which would affect the ability of oxygen to screen the second ligand from the charge of the metal. The ionic radii of first and second row transition metals in the +1 oxidation state, which is probably appropriate to consider for these MO^+ species, all fall in the range of 0.8-1.0 Å.[86] If the appropriate picture is more like M^{2+},O^-, then the positively charged volume would have an even smaller size. The size of the transition metals is apparently not large enough to offset the region of negative charge coming from the oxygen atoms, and consequently, the second PAH ligands do not bind effectively to these oxides. Information on the ionic radii of the +1 or +2 oxidation states of neodymium or uranium is not generally available because these are not the common oxidation states for these metals. However, the +3 oxidation states for these metals have radii of 1.12 and 1.16 Å, respectively.[86] The size of the metal atoms in the partially oxidized NdO^+ and UO^+ ions are almost certainly larger than this. Therefore, these heavier metal ions would occupy a larger volume of positive charge, and it is conceivable that this metal atom size would outweigh the oxygen atom charge screening from the standpoint of ligand interactions. This size effect could explain why the binding of second ligands in these sandwich species occurs more readily. It is also conceivable that the different strengths of attractive forces in these metal ions comes into play. Unlike the transition metals, the heavier systems could have

more M^{3+},O^{2-} character in their diatomic oxides, since it is much easier to ionize these metals to higher oxidation states. This higher charge density would result in a greater long-range attraction for a second PAH ligand, perhaps also contributing to the improved sandwich formation in these systems.

Another interesting aspect of this spectrum is the observation of uranium-corannulene fragment ions. Fragment ions corresponding to the loss of acetylene (C_2H_2) are observed for both the uranium mono- and di-ligand complexes. On the other hand, no significant amounts of fragment ions are detected from the uranium oxide complex ions. Similar behavior was also observed recently in molecular beam experiments in our lab for the photodissociation of uranium-benzene complex ions.[87] Benzene dissociation was found to occur when pure uranium-benzene complexes were photodissociated using 355 nm laser light, while photodissociation of uranium oxide-benzene complexes did not cause benzene fragmentation. Of the photo-fragments formed from uranium-benzene species, $U^+(C_2H_4)$ was the most abundant, presumably occurring by elimination of neutral C_2H_4 (ethylene), followed by $U^+(C_2H_2)$, corresponding to elimination of two acetylenes. However, in the case of corannulene, elimination of ethylene is less likely than elimination of acetylene, since C_2H_2 is a component of the PAH structure. As a result, only the latter channel is seen here. As seen in the benzene complexes, the oxide ions are apparently less reactive, because fragmentation in this way does not occur. It is also important to note that no corannulene fragments are observed for any of the other metals studied in these experiments and no coronene or pyrene fragments were observed in previous experiments This suggests that uranium ion is more reactive with corannulene than the other metals used in this study.

Organometallics + PAH

Having seen that metal salts and oxides produce PAH complexes, we decided to investigate the covaporization of PAH powders with organometallic complexes. These species are of interest because they could form mixed-ligand sandwich complexes. A number of mixed-ligand complexes of iron have been produced in conventional synthetic chemistry.[58,88,89] However, these synthesis methods are problematic because of the poor solubility of PAH systems. It is therefore interesting to see if covaporization methods would produce similar mixed-ligand complexes. Initial experiments employing ferrocene mixtures with coronene or pyrene were unsuccessful, presumably because of the high stability of ferrocene.[90] A strong ferrocene parent ion was observed, but no reaction products. Presumably, dissociation in the plasma is required for reaction, and ferrocene does not dissociate efficiently. We next examined iron cyclopentadienyl benzene, $Fe(cp)(bz)^+$, a molecule similar to ferrocene but with one of the cyclopentadiene ligands replaced by benzene. While ferrocene is an 18-electron species as a neutral complex, $Fe(cp)(bz)^+$ is an 18-electron species as a cation. Even so, the latter complex has a lower stability than ferrocene,[75] and it dissociates easily under our conditions. Figure 10 shows a mass spectrum of the covaporization of a mixed powder sample of $Fe(cp)(bz)^+$ and coronene. The primary fragments of $[Fe(cp)(bz)]^+$ include Fe^+ and $Fe(cp)^+$ under all laser power conditions. Coronene and ferrocene appear as the largest ions in abundance; decomposition of $Fe(cp)(bz)^+$ is the most likely source of ferrocene. The main complexes produced by the decomposition/reaction process in the plasma include $Fe^+(cp)(cor)$ and $Fe^+(cor)_2$, while a minor amount of $Fe^+(bz)(cor)$ is also detected.

Figure 11 shows a mass spectrum of the covaporization of a mixed powder sample of $[Fe(cp)(bz)]^+(PF_6)^-$ and corannulene. The primary fragments of the $Fe^+(cp)(bz)$ cation include

Fe^+ and $Fe^+(cp)$ under all laser power conditions. Again, the $Fe^+(cp)(bz)$ cation and ferricenium appear as the largest ions in abundance. The main complexes produced by the decomposition/reaction process in the plasma include $Fe^+(cora)$, $Fe^+(cp)(cora)$ and $Fe^+(cora)_2$. Similar to the behavior discussed for $Fe^+(cp)(cor)$ complexes, mixed-ligand complexes with corannulene can indeed be produced with good yields.

This approach therefore provides yet another method of producing metal-PAH complexes. The relative abundance of the different mixed-ligand and mono-ligand complexes can be rationalized simply on the basis of metal-ligand bond energies. The $Fe^+(cp)$ bond energy (91 kcal/mol)[90] is far greater than that of $Fe^+(bz)$ (37.8-44.7 kcal/mol),[75] so therefore benzene is more likely to be eliminated first in the plasma dissociation of $Fe(cp)(bz)^+$. Consistent with this, the reaction products $Fe^+(cp)(PAH)$ is also produced in much larger abundance than $Fe^+(bz)(PAH)$. Since the ratio of $Fe^+(cp)$ to $Fe^+(bz)$ is similar to the ratio of $Fe^+(cp)(cor)$ to $Fe^+(bz)(cor)$, it can be assumed that the primary mechanism of coronene complex production involves the reaction of the fragments of $Fe(cp)(bz)^+$ with coronene vapor created in the vaporization process. The amount of coronene or corannulene vapor present upon vaporization should be much greater than the amount of benzene and cyclopentadiene produced by the fragmentation of $Fe(cp)(bz)^+$. Therefore, the principle reaction of the iron cation produced by continued fragmentation must be with coronene or corannulene. This same reasoning explains why no $Fe^+(bz)_2$ is present in the spectrum. Very little $Fe^+(bz)$ is produced in the dissociation process, and only a low concentration of benzene is available for reaction. The large amount of PAH vapor present in the environment makes this pathway unlikely. Additionally, the iron benzene bond is the weakest of the metal ligand interactions investigated here at 37.8-44.7 kcal/mol.[75] Klippenstein has previously calculated the $Fe^+(cor)$ bond energy to be approximately

56 kcal/mol.[80] and Jena and coworkers have recently calculated the Fe^+(cora) bond energy to be approximately 84 kcal/mol,[57] which are significantly greater than the Fe^+(bz) bond energy. Our previous photodissociation experiments also found that iron binding to benzene was weaker than iron binding to coronene.[91]

In contrast to the ferrocene result, the reaction of dibenzene chromium, $Cr(bz)_2$, with coronene proved to be less interesting. A laser vaporization experiment performed in the absence of PAH showed that $Cr(bz)_2$ fragments in the laser plasma by losing both benzenes, producing a strong Cr^+ ion in the mass spectrum. The bond dissociation energy in this sandwich system (47.0-55.3 kcal/mol) is much lower than that for ferrocene (91 kcal/mol),[80,90] allowing more efficient dissociation of the complex in the plasma. When $Cr(bz)_2$ was combined with coronene (data not shown), no Cr^+(bz) or Cr^+(bz)(cor) ions were detected, but a substantial amount of $Cr^+(cor)_2$ was formed. The calculated Cr^+(cor) bond energy (46.2 kcal/mol),[80] is larger than that of Cr^+(bz) (36.4 kcal/mol),[80] which can explain the strong tendency for chromium ions to bind to coronene instead of benzene in this experiment.

4.4 STRUCTURES AND GROWTH TRENDS

Having discussed the variety of metal-PAH complexes that can be formed, it is natural to consider the structures of these systems. We have discussed some of these previously.[2-4,6,8] In intercalated graphite[92] and in other organometallic complexes, metals bind in η^6 ring sites, and therefore we assume that the same will be true here. However, theory has discussed that other binding sites, such as the metal localized over a double bond, may also be possible.[56] In coronene, previous experiments on synthetic analogs show that metal binds to the outer ring sites.[58,88,89] Futhermore, NMR spectroscopy shows that the highest electron density is found in

alternate outer ring sites.[58] Likewise, the rings in pyrene are also not equivalent with the highest electron density lying in the outer rings.[59] Complexes of various types would therefore likely have metal, metal halide or metal oxide species binding to these outer ring sites. If we accept the predictions of theory and existing experimental results, then metal ion binding to corannulene should take place on the convex side in one of the outer η^6 ring sites rather than on the η^5 interior site.[54,57,61-63] If this is true, then $M^+(PAH)_2$ sandwich complexes are also unlikely to be symmetrical. Since the metal ion will likely induce significant polarization in the organic π system, the ends of the PAH molecules opposite the metal sites should become more electron deficient, and consequently, these like-charged objects would tend to avoid each other in space. Sandwich complexes of the form $M^+(PAH)_2$ would therefore likely have staggered structures rather than parallel because of the coulombic repulsion of ring systems away from the metal.[8] Figures 12 and 13 show schematic structures that would result from these considerations. Also shown in Figure 12 is the sandwich structure of $NdO^+(cor)_2$, with the atoms drawn approximately to scale. This structure shows one way in which the sandwich structure can form for this complex, and how the size of Nd minimizes the effect of the repulsive interaction of the oxygen.

Taken together, these various experiments identify a number of general tendencies for the formation of metal-PAH complexes using laser vaporization methods. Complexes can be produced from the vaporization of mixed powders containing pure metal and PAH species, from the vaporization of mixed powders containing PAH and metal salts or oxides, and from mixed powders containing PAH and organometallic complexes. In all cases, metal cation complexes form rather efficiently in general. However, an anomaly in complex growth occurs for iron and cobalt, where complexes do not form from pure metal powders, but do form easily from metal

salts, oxide or organometallics. The formation of complexes in the laser vaporization process is not simple, and therefore it is not easy to probe the mechanism of this process. Additionally, we only detect the positive ions that form, and are not able to observe neutrals in these experiments. Negative ions of these metal-PAH systems have been produced previously in our molecular beam experiments,[5] but we did not investigate these species in this work. The most likely mechanism consistent with our data is that metal ions are produced in the gas phase following the initial laser impact, and then these cations react with neutral PAH species, producing the complexes. The iron and cobalt data can be explained if laser vaporization of pure metal produces mostly unreactive ground state cations, while other vaporization processes produce more reactive excited states.

In addition to the electronic state of the metal cations produced, complex formation also depends on other factors such as the metal-organic bond energies. Consistent with this idea, we are able to make mixed PAH sandwiches of iron with cyclopentadiene, but not with benzene. However, energetics alone are not enough to understand the growth processes. For example, calculations by Klippenstein indicate that the Fe^+(cor) bond energy is stronger than those predicted for the early transition metals.[80] Surprisingly, early transition metals in our experiments produced complexes more efficiently than iron. Ionization potentials of the metals play an direct role in the production of these complexes. The early first row transition metals (Sc to Cr) have IP's on average 1 eV lower than all of the later transition metals. This likely explains the more efficient production of atomic metal cation for these metals, which in turn results in more efficient production of PAH complexes. Similarly, atomic metal cations were also produced more efficiently in experiments with metal salts, oxides and organometallics than from pure metals, presumably due to their oxidation states in these compounds. Consequently,

complex formation was also efficient in these experiments, even for systems other than iron and cobalt which had no apparent electronic state issues.

No multimetal-PAH complexes were observed in these experiments except for the Fe_2O^+, Co_2Cl^+ and $Ti_2O_x^+$ species. This is in contrast to molecular beam experiments performed by our group, where many multi-metal complexes are seen.[2-4,6,8] The simplest explanation for this difference is the absence of a collision gas in the present experiments. In these experiments, temperatures generated in the cluster source are much higher than in pulsed nozzle experiments, and the vaporized species also experience fewer collisions. Thus, only small clusters with relatively high bond energies will survive. The multi-metal species best able to survive these extreme conditions are the strongly-bound oxides, and therefore complexes with these species are understandable.

It is interesting to speculate on the implications of this work for interstellar condensation processes that might lead to the formation of metal-PAH species. Iron, magnesium and aluminum are some of the most abundant metals in these environments.[93] Apparently, aluminum and magnesium ions may condense on PAH surfaces to form mono-ligand complexes, but sandwich species are unlikely to form with these metals. Likewise, iron cations may be unreactive unless they are produced in excited states, and therefore condensation with PAH's may not be efficient in the interstellar environment. Because metal oxides are so strongly bound, they are one of the first molecular species to form in stellar outgrowths,[93] and the condensation of these species on PAH surfaces appears to be relatively efficient.

In the experiments discussed in this chapter, we have employed pyrene, coronene, and corannulene because of their convenient low vapor pressures. We found similar efficiencies for complex formation with all of these systems. In our molecular beam experiments, we also found

similar efficiencies for several other PAH systems. It is therefore reasonable to expect that a variety of metal ion-PAH complexes could be produced with the methods described here. We were therefore surprised to find that these methods were unsuccessful for the production of metal-C_{60} complexes. In selected experiments combining C_{60} with Cr powder, iron chloride, titanium oxide or zirconium carbide, we were not able to observe any metal-C_{60} complexes. On the other hand, in our previous molecular beam work, many metal-C_{60} complexes were produced,[13,91] including mixed sandwiches with PAH's.[8] However, we did show that metal-C_{60} complexes were not as strongly bound as corresponding metal cation-coronene complexes or even M^+-benzene complexes.[8] Apparently, this weaker binding tendency limits the efficiency of formation of metal-C_{60} complexes in these experiments without a collision gas present.

4.5 REFERENCES

(1) Martin, T. P. *Z. Phys. D Atom. Mol. Cl.* **1986**, *3*, 211.

(2) Buchanan, J. W.; Reddic, J. E.; Grieves, G. A.; Duncan, M. A. *J. Phys. Chem. A* **1998**, *102*, 6390.

(3) Buchanan, J. W.; Grieves, G. A.; Flynn, N. D.; Duncan, M. A. *Int. J. Mass Spectrom.* **1999**, *187*, 617.

(4) Foster, N. R.; Grieves, G. A.; Buchanan, J. W.; Flynn, N. D.; Duncan, M. A. *J. Phys. Chem. A* **2000**, *104*, 11055.

(5) Duncan, M. A.; Knight, A. M.; Negishi, Y.; Nagao, S.; Judai, K.; Nakajima, A.; Kaya, K. *J. Phys. Chem. A* **2001**, *105*, 10093.

(6) Foster, N. R.; Buchanan, J. W.; Flynn, N. D.; Duncan, M. A. *Chem. Phys. Lett.* **2001**, *341*, 476.

(7) Ayers, T. M.; Westlake, B. C.; Duncan, M. A. *J. Phys. Chem. A* **2004**, *108*, 9805.

(8) Buchanan, J. W.; Grieves, G. A.; Reddic, J. E.; Duncan, M. A. *Int. J. Mass Spectrom.* **1999**, *183*, 323.

(9) Wan, Z. M.; Christian, J. F.; Anderson, S. L. *Phys. Rev. Lett.* **1992**, *69*, 1352.

(10) Kan, S. Z.; Byun, Y. G.; Freiser, B. S. *J. Am. Chem. Soc.* **1994**, *116*, 8815.

(11) Kan, S. Z.; Byun, Y. G.; Freiser, B. S. *J. Am. Chem. Soc.* **1995**, *117*, 1177.

(12) Basir, Y.; Anderson, S. L. *Chem. Phys. Lett.* **1995**, *243*, 45.

(13) Reddic, J. E.; Robinson, J. C.; Duncan, M. A. *Chem. Phys. Lett.* **1997**, *279*, 203.

(14) Basir, Y. J.; Anderson, S. L. *Int. J. Mass Spectrom.* **1999**, *187*, 603.

(15) Martin, T. P.; Malinowski, N.; Zimmermann, U.; Naher, U.; Schaber, H. *J. Chem. Phys.* **1993**, *99*, 4210.

(16) Zimmermann, U.; Malinowski, N.; Naher, U.; Frank, S.; Martin, T. P. *Phys. Rev. Lett.* **1994**, *72*, 3542.

(17) Zimmermann, U.; Malinowski, N.; Burkhardt, A.; Martin, T. P. *Carbon* **1995**, *33*, 995.

(18) Martin, T. P.; Zimmermann, U.; Malinowski, N.; Heinebrodt, M.; Frank, S.; Tast, F. *Phys. Scripta* **1996**, *T66*, 38.

(19) Tast, F.; Malinowski, N.; Frank, S.; Heinebrodt, M.; Billas, I. M. L.; Martin, T. P. *Z. Phys. D Atom. Mol. Cl.* **1997**, *40*, 351.

(20) Hoshino, K.; Kurikawa, T.; Takeda, H.; Nakajima, A.; Kaya, K. *Surf. Rev. Lett.* **1996**, *3*, 183.

(21) Yasuike, T.; Nakajima, A.; Yabushita, S.; Kaya, K. *J. Phys. Chem. A* **1997**, *101*, 5360.

(22) Kurikawa, T.; Takeda, H.; Hirano, M.; Judai, K.; Arita, T.; Nagao, S.; Nakajima, A.; Kaya, K. *Organometallics* **1999**, *18*, 1430.

(23) Nakajima, A.; Nagao, S.; Takeda, H.; Kurikawa, T.; Kaya, K. *J. Chem. Phys.* **1997**, *107*, 6491.

(24) Nagao, S.; Kurikawa, T.; Miyajima, K.; Nakajima, A.; Kaya, K. *J. Phys. Chem. A* **1998**, *102*, 4495.

(25) Kurikawa, T.; Negishi, Y.; Hayakawa, F.; Nagao, S.; Miyajima, K.; Nakajima, A.; Kaya, K. *J. Am. Chem. Soc.* **1998**, *120*, 11766.

(26) Miyajima, K.; Kurikawa, T.; Hashimoto, M.; Nakajima, A.; Kaya, K. *Chem. Phys. Lett.* **1999**, *306*, 256.

(27) Nagao, S.; Kato, A.; Nakajima, A.; Kaya, K. *J. Am. Chem. Soc.* **2000**, *122*, 4221.

(28) Nakajima, A.; Kaya, K. *J. Phys. Chem. A* **2000**, *104*, 176.

(29) Barth, W. E.; Lawton, R. G. *J. Am. Chem. Soc.* **1966**, *88*, 380.

(30) Lawton, R. G.; Barth, W. E. *J. Am. Chem. Soc.* **1971**, *93*, 1730.

(31) Scott, L. T.; Hashemi, M. M.; Meyer, D. T.; Warren, H. B. *J. Am. Chem. Soc.* **1991**, *113*, 7082.

(32) Scott, L. T.; Cheng, P. C.; Hashemi, M. M.; Bratcher, M. S.; Meyer, D. T.; Warren, H. B. *J. Am. Chem. Soc.* **1997**, *119*, 10963.

(33) Guillen, M. D.; Sopelana, P.; Partearroyo, M. A. *Rev. Environ. Health* **1997**, *12*, 133.

(34) Armstrong, B.; Hutchinson, E.; Unwin, J.; Fletcher, T. *Environ. Health Persp.* **2004**, *112*, 970.

(35) Birks, J. B. *Photophysics of Aromatic Molecules*; John Wiley: London, 1970.

(36) Klessinger, M.; Michl, J. *Excited States and Photochemistry of Organic Molecules*; VCH Publishers: New York, 1995.

(37) Harvey, R. G. *Polyaromatic Hydrocarbons*; Wiley-VCH: New York, 1996.

(38) Bohme, D. K. *Chem. Rev.* **1992**, *92*, 1487.

(39) *The Diffuse Interstellar Bands*; Tielens, A. G. G. M.; Snow, T. P., Eds.; Kluwer Academic Publishers: Dordrecht, 1995.

(40) Salama, F.; Bakes, E. L. O.; Allamandola, L. J.; Tielens, A. G. G. M. *Astrophys. J.* **1996**, *458*, 621.

(41) Henning, T.; Salama, F. *Science* **1998**, *282*, 2204.

(42) Salama, F. *Origins Life Evol. B* **1998**, *28*, 349.

(43) Ruiterkamp, R.; Halasinski, T.; Salama, F.; Foing, B. H.; Allamandola, L. J.; Schmidt, W.; Ehrenfreund, P. *Astron. Astrophys.* **2002**, *390*, 1153.

(44) Allamandola, L. J.; Tielens, A. G. G. M.; Barker, J. R. *Astrophys. J.* **1985**, *290*, L25.

(45) Allamandola, L. J.; Tielens, A. G. G. M.; Barker, J. R. *Astrophys. J. Suppl. S.* **1989**, *71*, 733.

(46) Leger, A.; Dhendecourt, L.; Defourneau, D. *Astron. Astrophys.* **1989**, *216*, 148.

(47) *Intercalation Chemistry*; Whittingham, M. S.; Jacobson, A., Eds.; Academic Press: New York, 1982.

(48) *Science of Fullerenes and Carbon Nanotubes*; Dresselhaus, M. S.; Dresselhaus, G.; Eklund, P. C., Eds.; Academic Press: San Diego, 1996.

(49) Dresselhaus, M. S.; Dresselhaus, G. *Adv. Phys.* **2002**, *51*, 1.

(50) *Graphite Intercalation Compounds and Applications*; Enoki, T.; Suzuki, M.; Endo, M., Eds.; Oxford U. Press: New York, 2003.

(51) Klotz, A.; Marty, P.; Boissel, P.; Serra, G.; Chaudret, B.; Daudey, J. P. *Astron. Astrophys.* **1995**, *304*, 520.

(52) Klotz, A.; Marty, P.; Boissel, P.; deCaro, D.; Serra, G.; Mascetti, J.; deParseval, P.; Derouault, J.; Daudey, J. P.; Chaudret, B. *Planet. Space Sci.* **1996**, *44*, 957.

(53) Dunbar, R. C.; Uechi, G. T.; Asamoto, B. *J. Am. Chem. Soc.* **1994**, *116*, 2466.

(54) Dunbar, R. C. *J. Phys. Chem. A* **2002**, *106*, 9809.

(55) Klippenstein, S. J.; Yang, C. N. *Int. J. Mass Spectrom.* **2000**, *201*, 253.

(56) Senapati, L.; Nayak, S. K.; Rao, B. K.; Jena, P. *J. Chem. Phys.* **2003**, *118*, 8671.

(57) Kandalam, A. K.; Rao, B. K.; Jena, P. *unpublished work* **2005**.

(58) Schmitt, G.; Keim, W.; Fleischhauer, J.; Walbergs, U. *J. Organomet. Chem.* **1978**, *152*, 315.

(59) Steiner, E.; Fowler, P. W.; Jenneskens, L. W.; Havenith, R. W. A. *Eur. J. Org. Chem.* **2002**, 163.

(60) Scott, L. T.; Hashemi, M. M.; Bratcher, M. S. *J. Am. Chem. Soc.* **1992**, *114*, 1920.

(61) Seiders, T. J.; Baldridge, K. K.; O'Connor, J. M.; Siegel, J. S. *J. Am. Chem. Soc.* **1997**, *119*, 4781.

(62) Alvarez, C. M.; Angelici, R. J.; Sygula, A.; Sygula, R.; Rabideau, P. W. *Organometallics* **2003**, *22*, 624.

(63) Vecchi, P. A.; Alvarez, C. M.; Ellern, A.; Angelici, R. J.; Sygula, A.; Sygula, R.; Rabideau, P. W. *Angew. Chem. Int. Edit.* **2004**, *43*.

(64) Caraiman, D.; Koyanagi, G. K.; Scott, L. T.; Preda, D. V.; Bohme, D. K. *J. Am. Chem. Soc.* **2001**, *123*, 8573.

(65) Elliott, E. L.; Hernandez, G. A.; Linden, A.; Siegel, J. S. *Org. Biomol. Chem.* **2005**, *3*, 407.

(66) Petrukhina, M. A.; Andreini, K. W.; Mack, J.; Scott, L. T. *Angewandte Chemie-International Edition* **2003**, *42*, 3375.

(67) Cartier, S. F.; Chen, Z. Y.; Walder, G. J.; Sleppy, C. R.; Castleman, A. W., Jr. *Science* **1993**, *260*, 195.

(68) Ho, Y. P.; Yang, Y. C.; Klippenstein, S. J.; Dunbar, R. C. *J. Phys. Chem.* **1997**, *101*, 3338.

(69) Bauschlicher, C. W.; Partridge, H. *J. Phys. Chem.* **1991**, *95*, 9694.

(70) Sodupe, M.; Bauschlicher, C. W. *Chem. Phys. Lett.* **1991**, *181*, 321.

(71) Sodupe, M.; Bauschlicher, C. W.; Partridge, H. *Chem. Phys. Lett.* **1992**, *192*, 185.

(72) Bauschlicher, C. W.; Sodupe, M.; Partridge, H. *J. Chem. Phys.* **1992**, *96*, 4453.

(73) Andersen, A.; Muntean, F.; Walter, D.; Rue, C.; Armentrout, P. B. *J. Phys. Chem. A* **2000**, *104*, 692.

(74) Amicangelo, J. C.; Armentrout, P. B. *J. Phys. Chem. A* **2000**, *104*, 11420.

(75) Meyer, F.; Khan, F. A.; Armentrout, P. B. *J. Am. Chem. Soc.* **1995**, *117*, 9740.

(76) Gregoire, G.; Brinkmann, N. R.; van Heijnsbergen, D.; Schaefer, H. F.; Duncan, M. A. *J. Phys. Chem. A* **2003**, *107*, 218.

(77) Walters, R. S.; Brinkmann, N. R.; Schaefer, H. F.; Duncan, M. A. *J. Phys. Chem. A* **2003**, *107*, 7396.

(78) Inokuchi, Y.; Ohshimo, K.; Misaizu, F.; Nishi, N. *Chem. Phys. Lett.* **2004**, *390*, 140.

(79) Inokuchi, Y.; Ohshimo, K.; Misaizu, F.; Nishi, N. *J. Phys. Chem. A* **2004**, *108*, 5034.

(80) Klippenstein, S. J.; Yang, C.-N. *Int. J. Mass Spectrom.* **2001**, *201*, 253.

(81) Fisher, E. R.; Elkind, J. L.; Clemmer, D. E.; Georgiadis, R.; Loh, S. K.; Aristov, N.; Sunderlin, L. S.; Armentrout, P. B. *J. Chem. Phys.* **1990**, *93*, 2676.

(82) Armentrout, P. B. *Annu. Rev. Phys. Chem.* **1990**, *41*, 313.

(83) Van Koppen, P. A. M.; Kemper, P. R.; Bowers, M. T. *J. Am. Chem. Soc.* **1992**, *114*, 10941.

(84) Van Koppen, P. A. M.; Kemper, P. R.; Bowers, M. T. *J. Am. Chem. Soc.* **1992**, *114*, 1083.

(85) Weisshaar, J. C. *Acc. Chem. Res.* **1993**, *26*, 213.

(86) Huheey, J. E.; Keiter, E. A.; Keiter, R. L. *Inorganic Chemistry: Principles of Structure and Reactivity, 4th edition*; Harper-Collins: New York, 1993.

(87) Pillai, E. D.; Molek, K. S.; Duncan, M. A. *Chem. Phys. Lett.* **2005**, *405*, 247.

(88) Morrison, W. H.; Ho, E. Y.; Hendrickson, D. N. *Inorg. Chem.* **1975**, *14*, 500.

(89) Astruc, D. *Tetrahedron* **1983**, *39*, 4027.

(90) Lewis, K. E.; Smith, G. P. *J. Am. Chem. Soc.* **1984**, *106*, 4650.

(91) Grieves, G. A.; Buchanan, J. W.; Reddic, J. E.; Duncan, M. A. *Int. J. Mass Spectrom.* **2001**, *204*, 223.

(92) Müller, U. *Inorganic Structural Chemistry*; John Wiley: Chichester, 1993.

(93) *The Molecular Astrophysics of Stars and Galaxies*; Hartquist, T. W.; Williams, D. A., Eds.; Clarendon Press: Oxford, 1998.

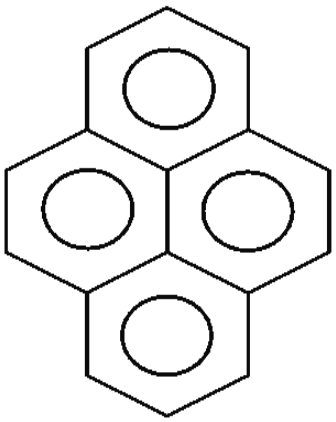

pyrene

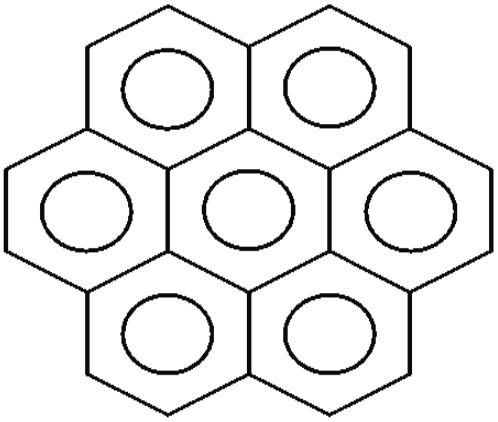

coronene

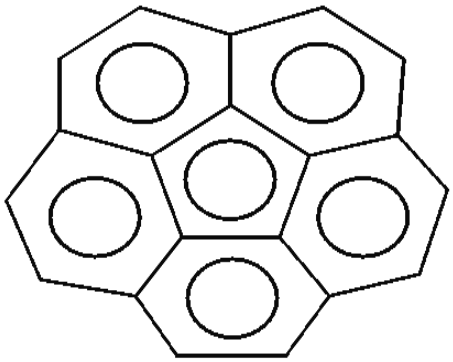

corannulene

Figure 1. Illustration of the PAH molecules, pyrene, coronene and corannulene

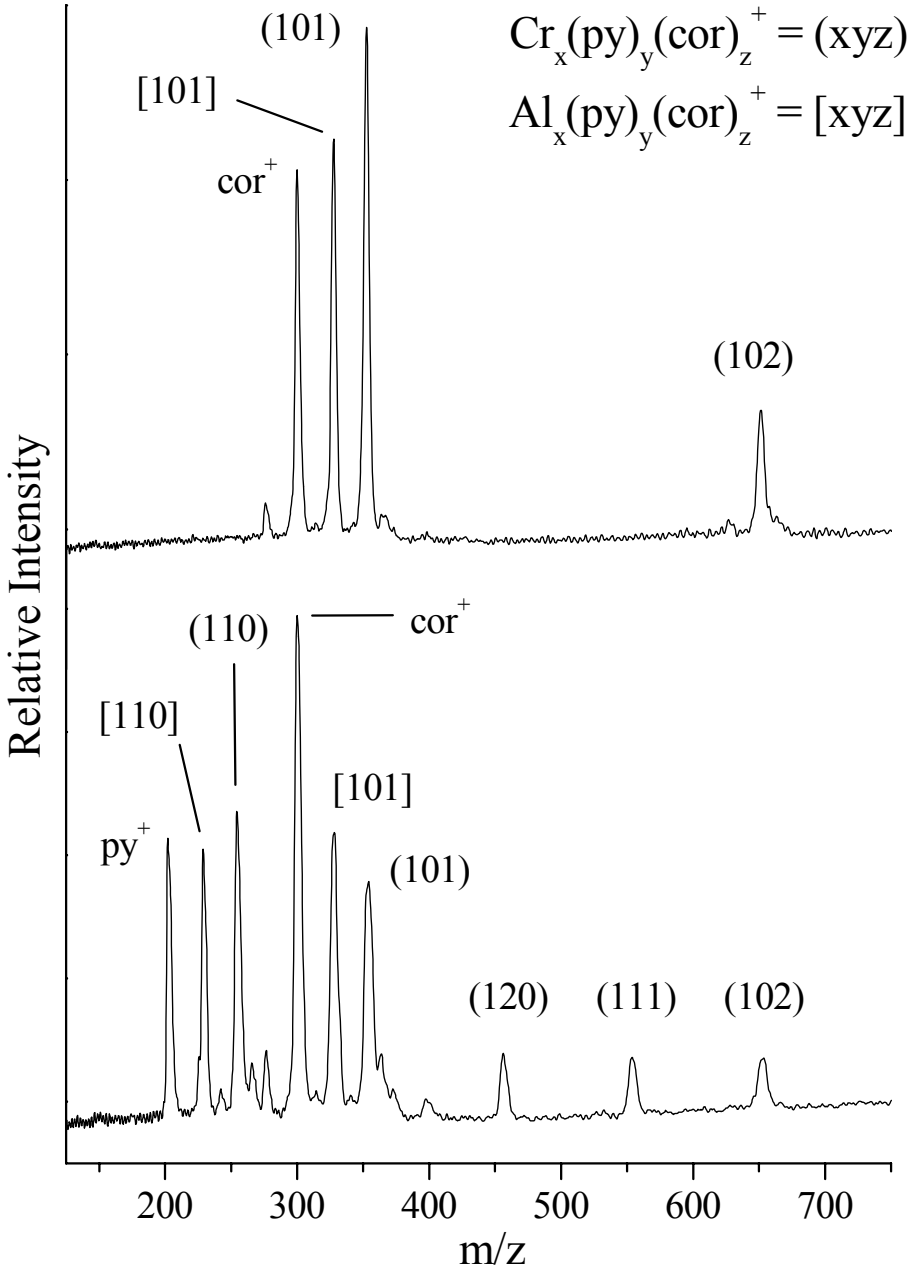

Figure 2. Mass spectra resulting from covaporization of chromium and coronene on an aluminum probe (upper trace) and chromium with a mixture of coronene and pyrene on an aluminum probe (lower trace). Complexes of the form $Cr_x{}^{67}{}_y(cor)_z^+$ are indicated as (xyz), while similar complexes with aluminum are indicated as [xyz].

Complex	x=1	x=2
$Mg^+(C_6H_6)_x$	1.39	-----
$Ti^+(C_6H_6)_x$	2.68	2.62
$V^+(C_6H_6)_x$	2.42	2.55
$Cr^+(C_6H_6)_x$	1.76	2.40
$Mn^+(C_6H_6)_x$	1.38	2.10
$Fe^+(C_6H_6)_x$	2.15	1.94
$Co^+(C_6H_6)_x$	2.65	1.73
$Ni^+(C_6H_6)_x$	2.52	1.52
$Cu^+(C_6H_6)_x$	2.26	1.61

Table 1. Metal ion-benzene bond energies (D_0; eV) determined by collision-induced dissociation.[73-75] The values shown are for the loss of one benzene ligand.

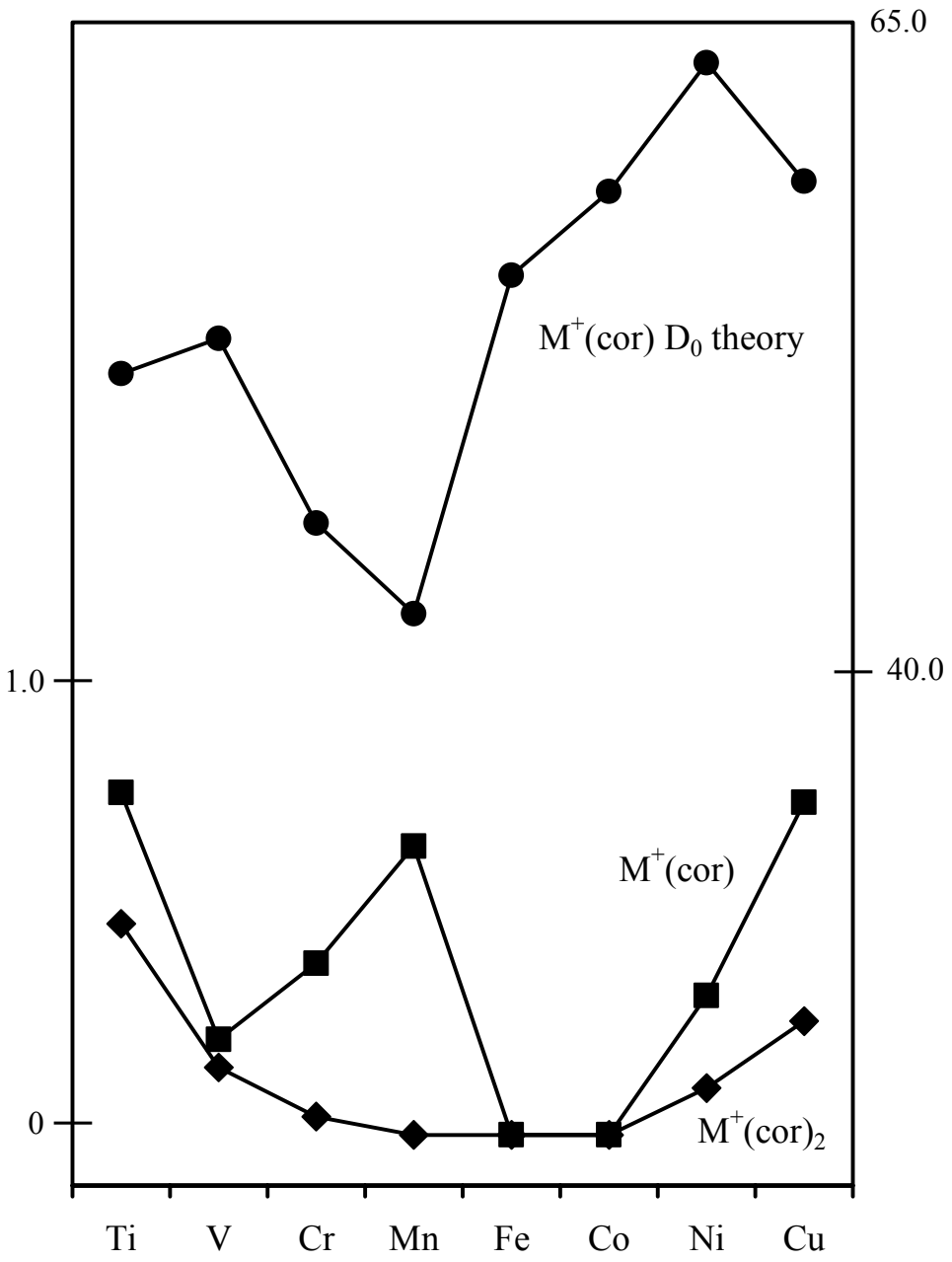

Figure 3. Graph displaying the relative abundances of the $M^+(cor)$ and $M^+(cor)_2$ complexes normalized to the abundance of metal ion, and the comparison to the calculated M^+-coronene bond energies.[47] The left vertical axis indicates the relative tendency to form complexes, while the right vertical axis indicates the calculated bond energy (kcal/mol).

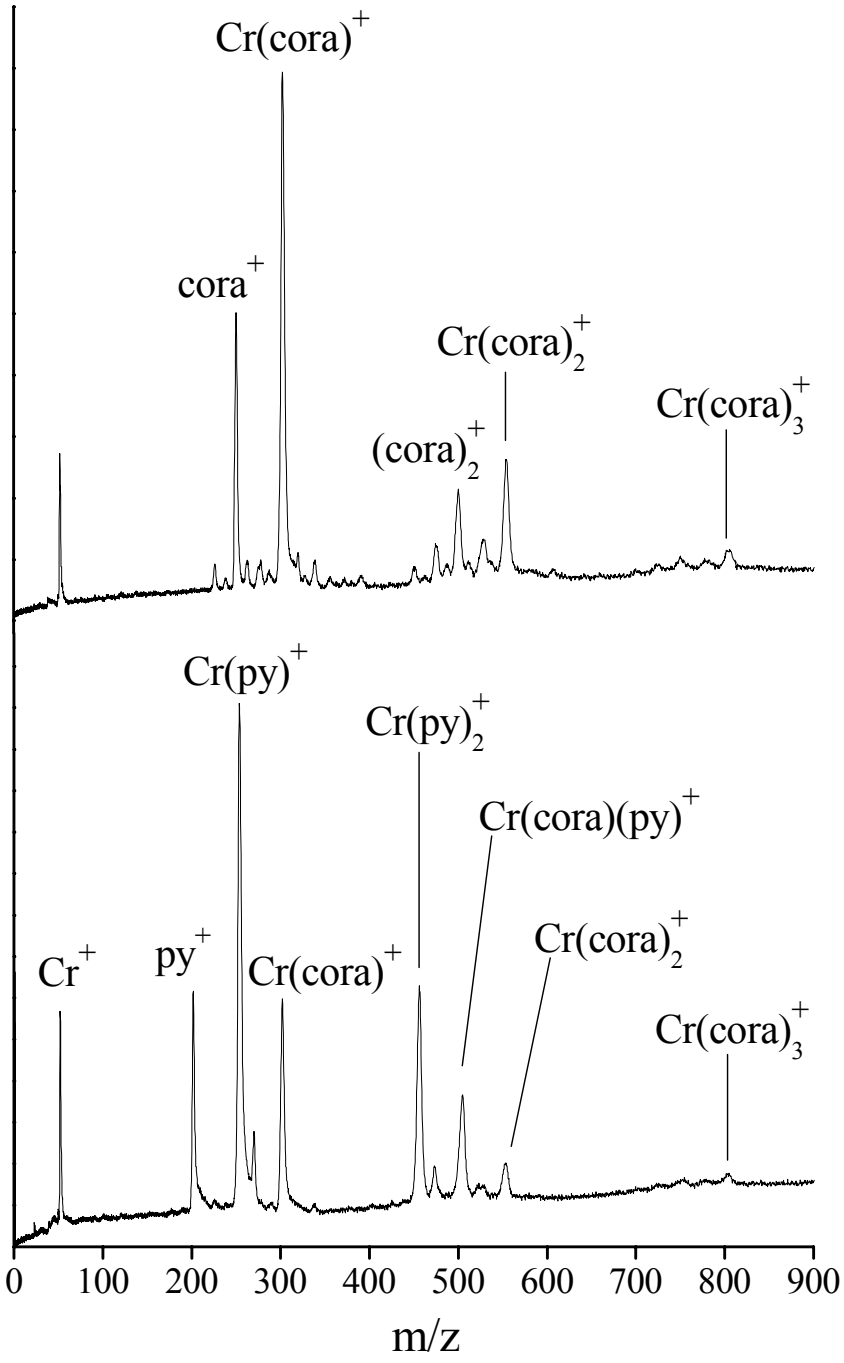

Figure 4. The mass spectrum resulting from covaporization of chromium powder and corannulene (top) and that resulting from covaporization of chromium powder and a mixture of corannulene and pyrene (bottom).

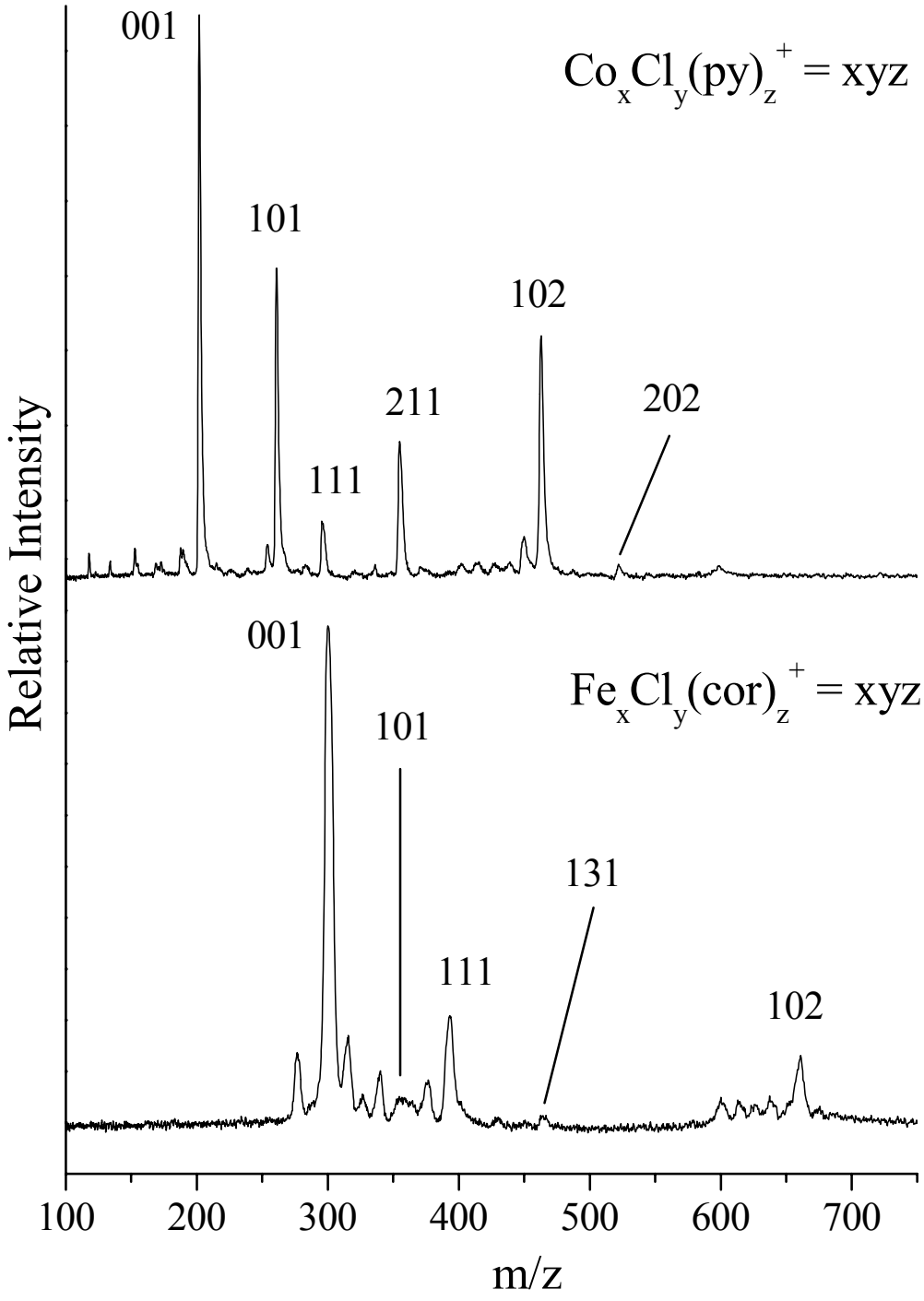

Figure 5. Mass spectra resulting from covaporization of $FeCl_2 \cdot 4H_2O$ or $CoCl_2 \cdot 6H_2O$ with coronene and pyrene.

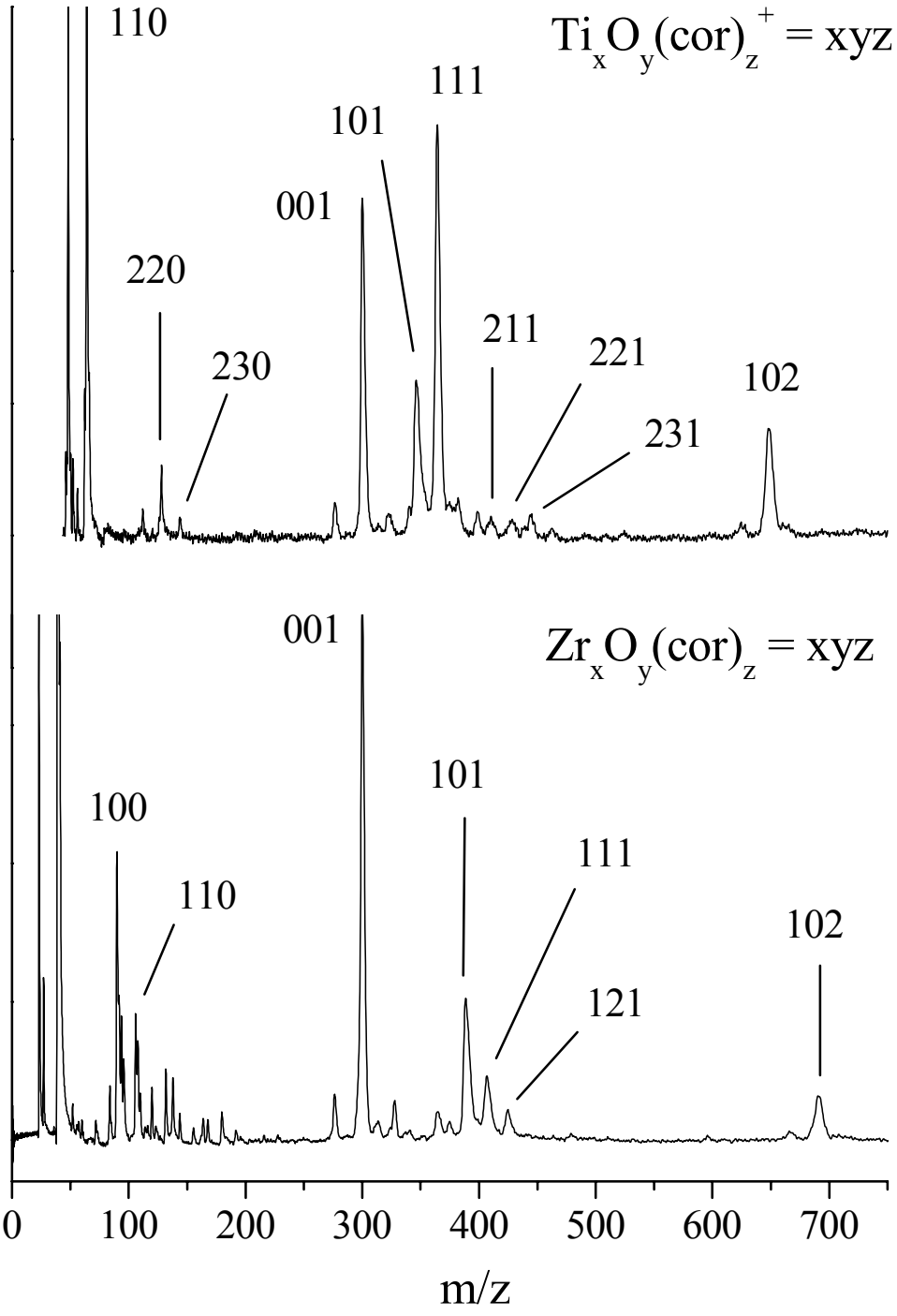

Figure 6. Mass spectra resulting from covaporization of titanium oxide with coronene and of zirconium carbide with coronene.

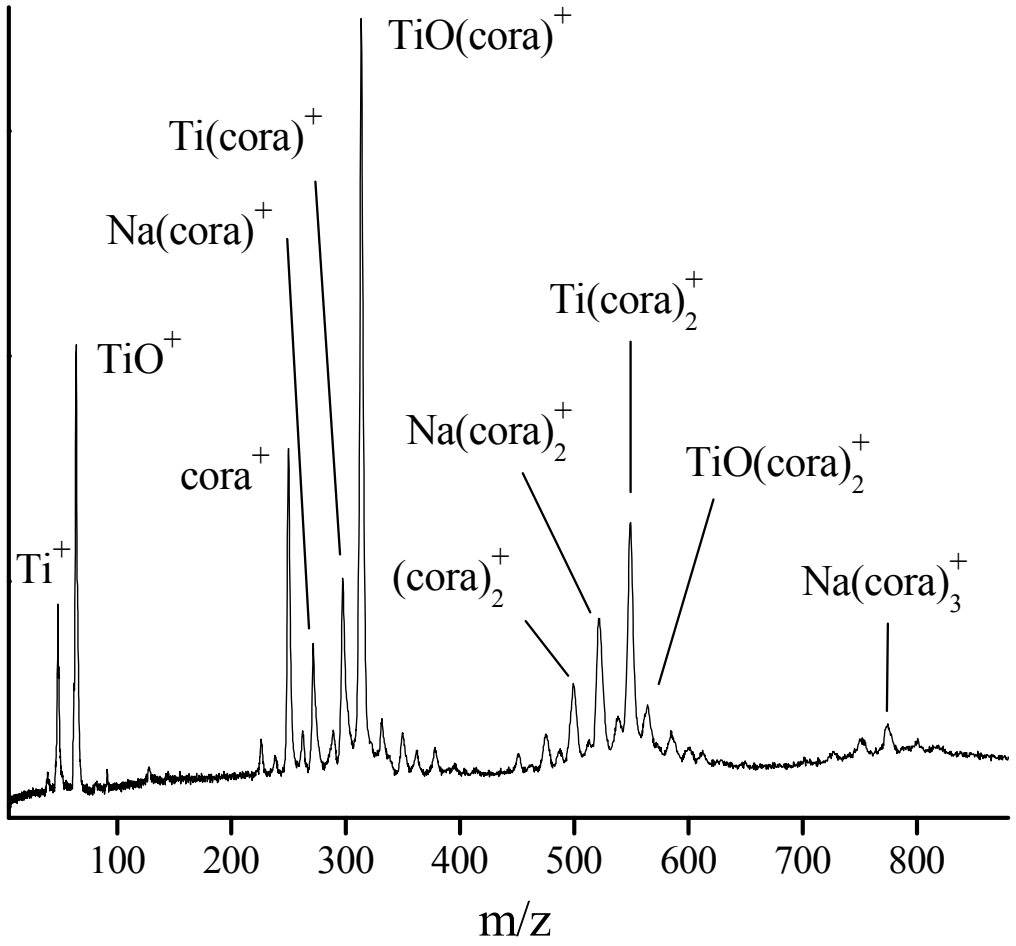

Figure 7. The mass spectrum resulting from covaporization of titanium powder and corannulene.

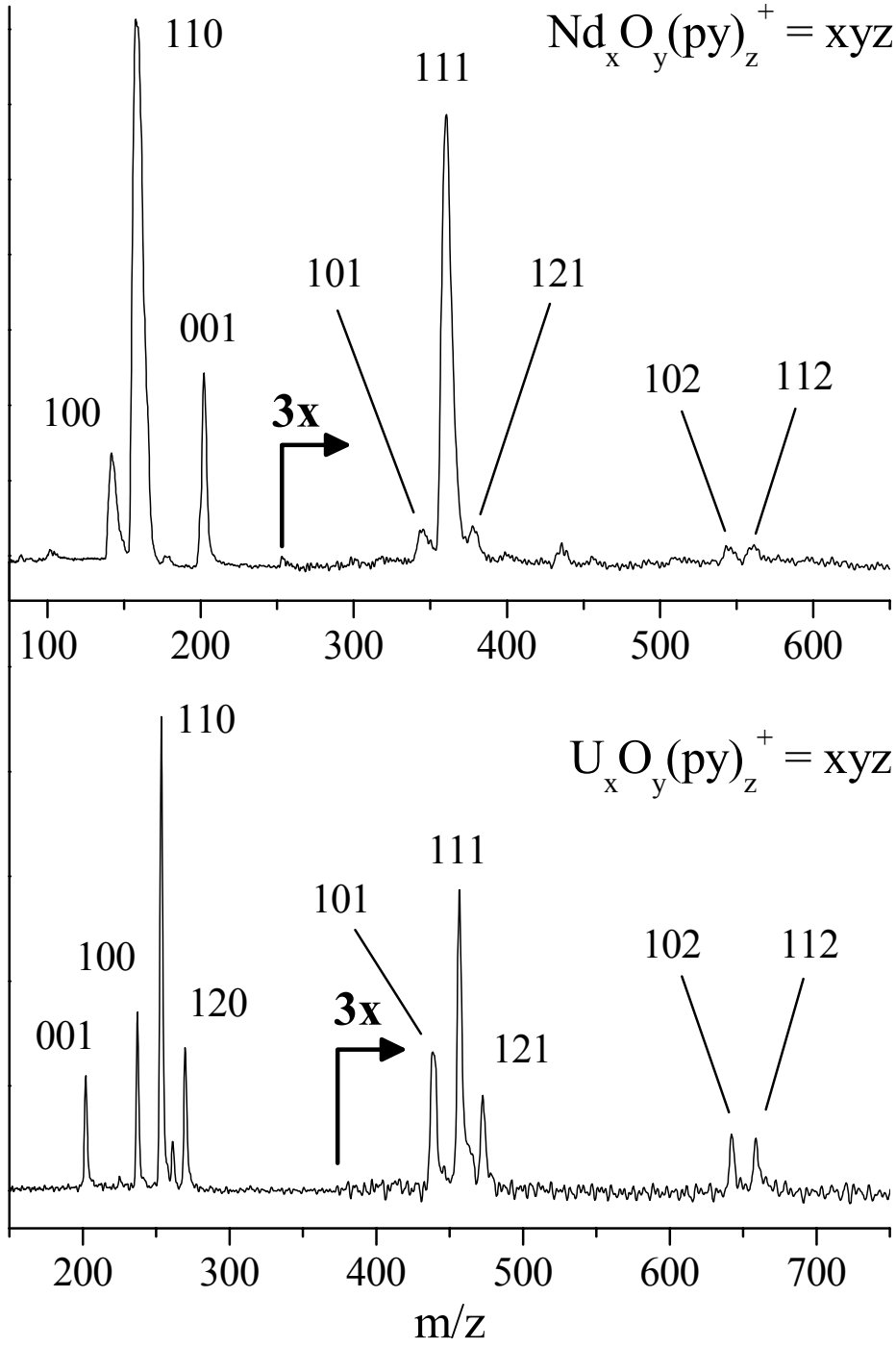

Figure 8. Mass spectra resulting from covaporization of neodymium oxide with pyrene and uranyl acetate (UAc) with pyrene.

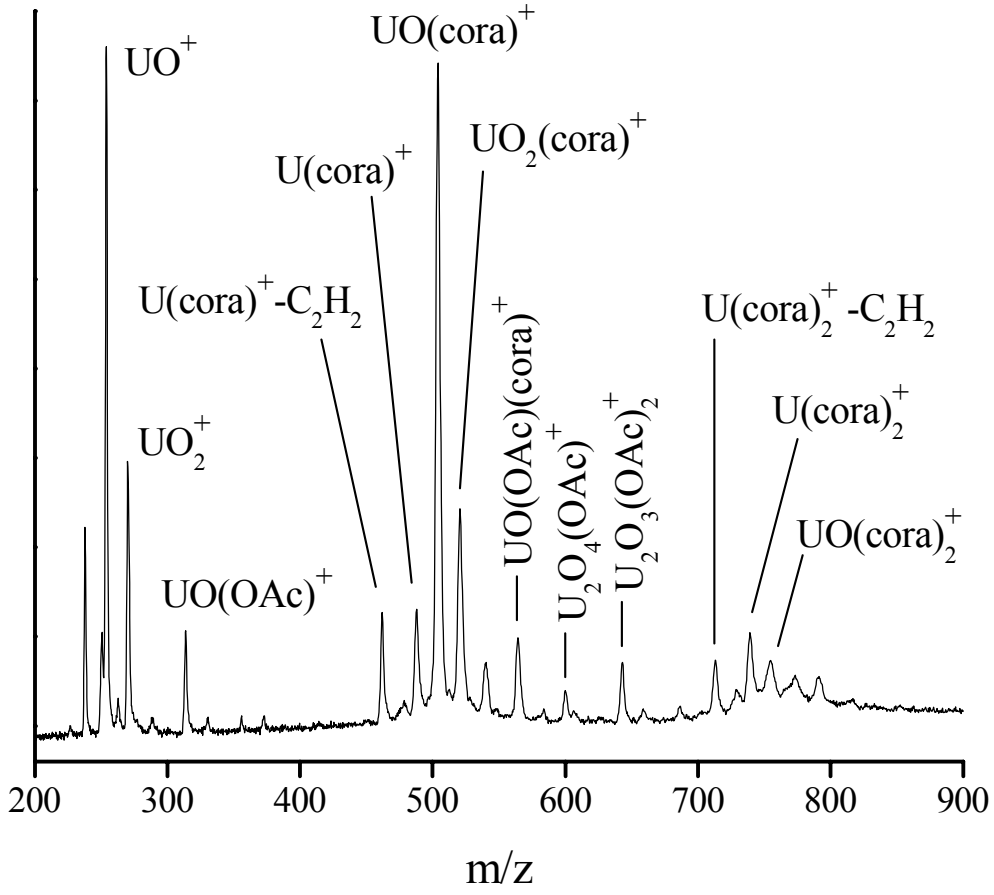

Figure 9. The mass spectrum resulting from covaporization of uranyl acetate and corannulene.

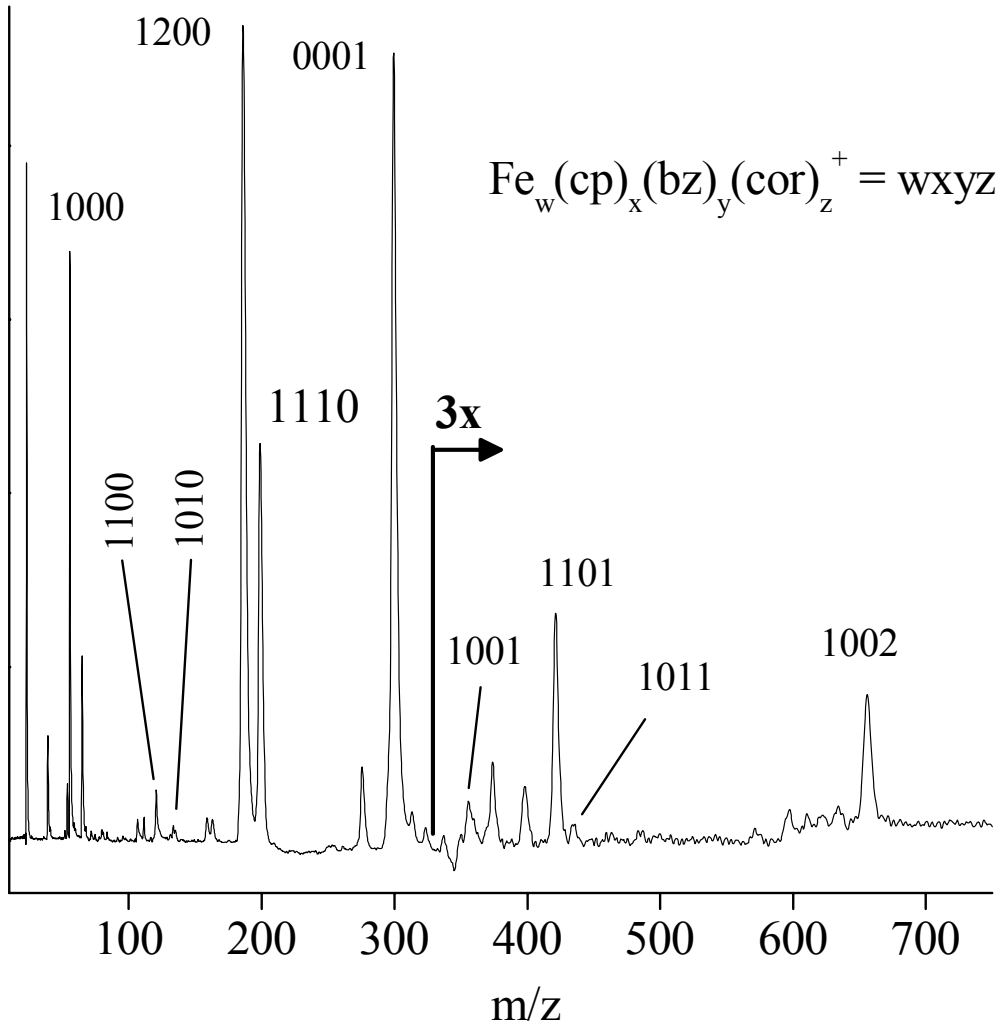

Figure 10. Mass spectra resulting from covaporization of iron cyclopentadienyl benzene and coronene.

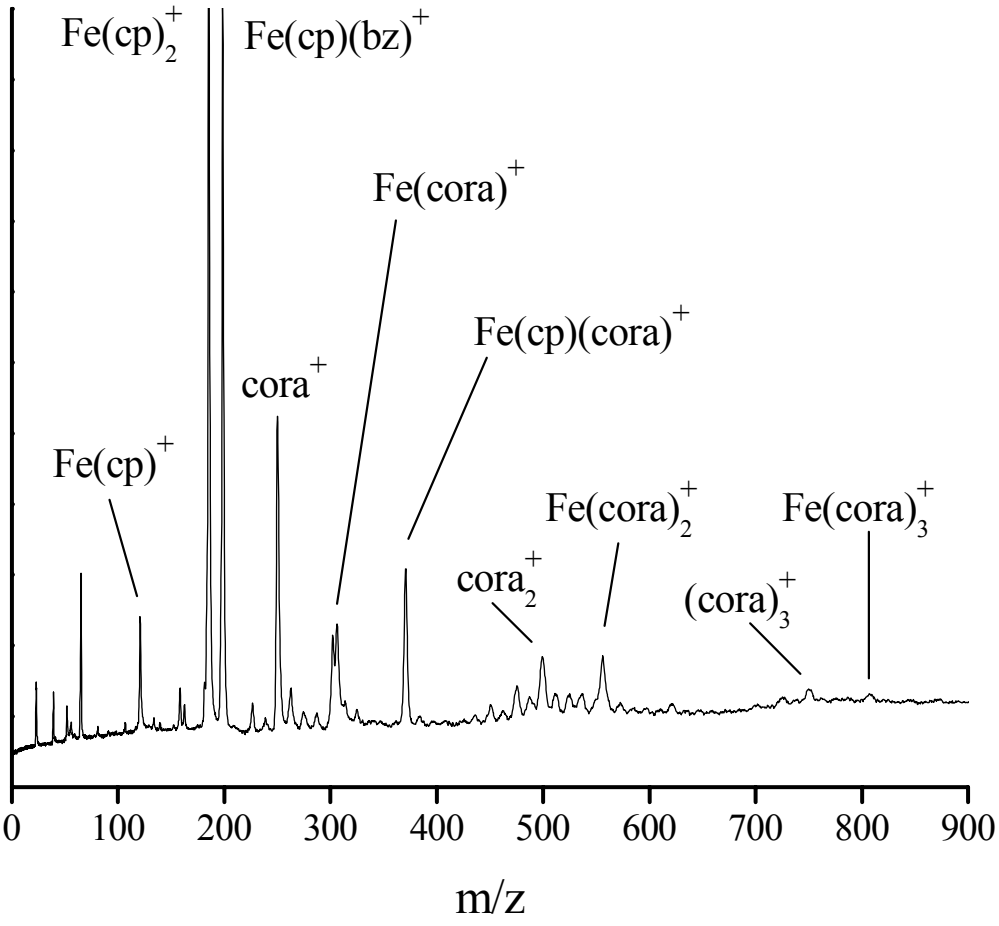

Figure 11. The mass spectrum resulting from covaporization of $Fe(cp)(bz)^+$ and corannulene.

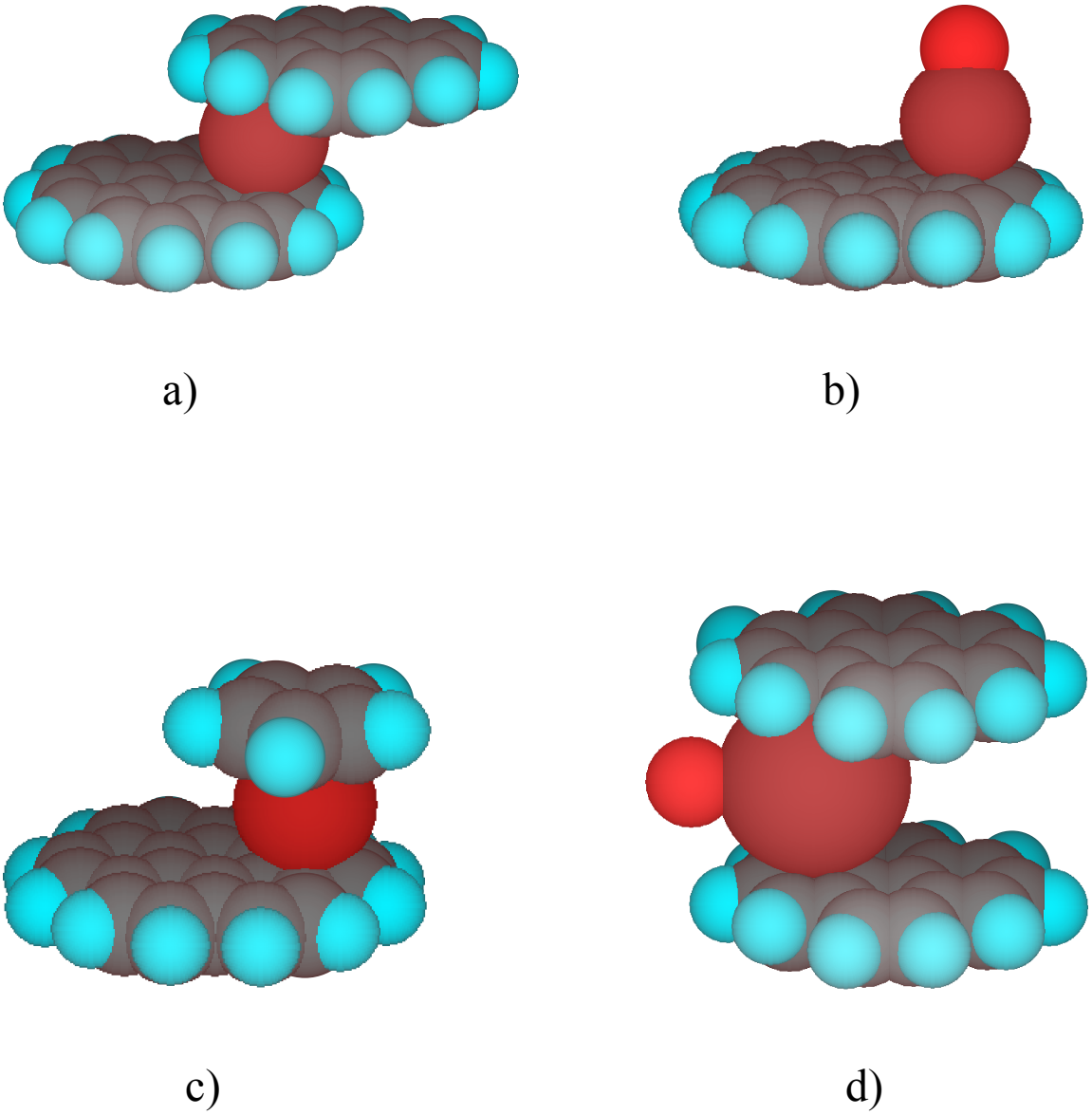

Figure 12. Schematic structures expected for various complexes studied here. In a), the mixed-ligand complex $M^{+}(cor)$[67] is shown. The binding to outer rings on both PAH species leads to an expected staggered sandwich structure. In b), the complex $MX^{+}(cor)$ is shown, for X=O, Cl, etc., with M binding downward to an outer ring site. c) shows the $Fe^{+}(cp)(cor)$ mixed sandwich, also with outer ring binding on the coronene. d) shows the complex $NdO^{+}(cor)_2$, with the metal oxide approximately to scale, and outer-ring binding on the coronene.

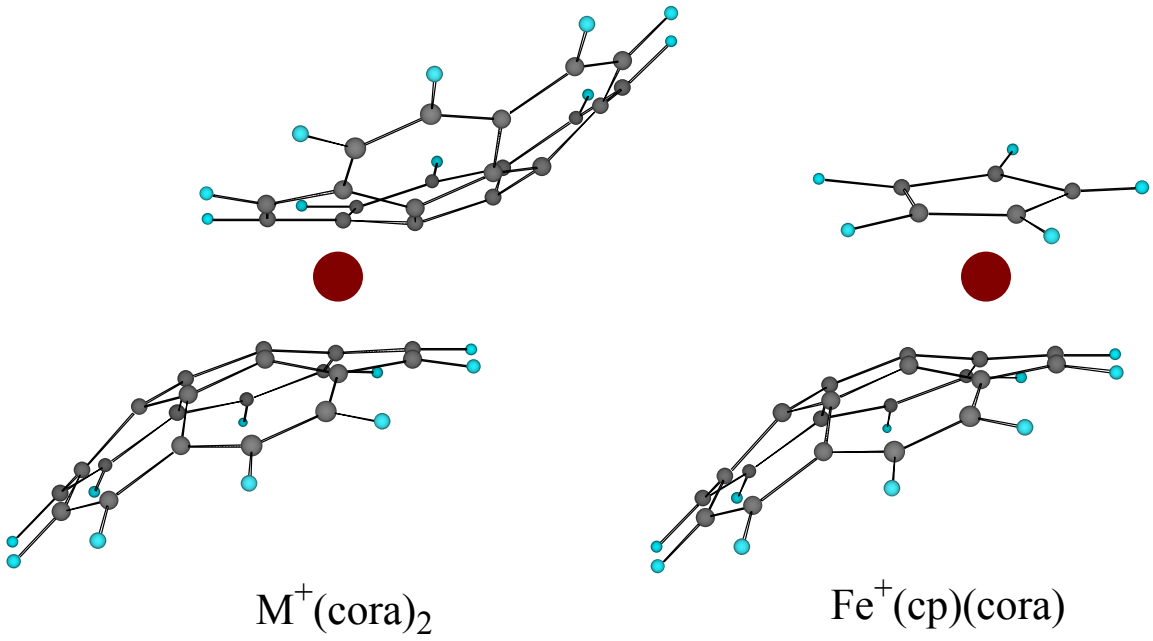

Figure 13. Schematic structures expected for various complexes studied here. In a), the di-ligand complex $M^+(cora)_2$ is shown. The binding to outer rings (convex η^6 sites) on both corannulene molecules leads to an expected staggered sandwich structure. In b) the $Fe^+(cp)(cora)$ mixed sandwich is shown, also with outer ring η^6 binding on corannulene.

CHAPTER 5

PRODUCTION OF TRANSITION METAL OXIDE NANO-CLUSTER MATERIALS

5.1 BACKGROUND

As mentioned previously, the first example of a cluster molecule to be discovered in gas phase experiments and isolated in bulk quantities was C_{60}.[1-4] This amazing discovery spawned a new field of cluster-based materials science. Since that time, a variety of systems have been investigated in the attempt to make cluster-based materials, including metallo-fullerenes, carbon nanotubes and metal-filled nanotubes.[5] However, there are many other examples of fascinating metal-containing clusters which have been detected in the gas phase (see Chapter 1.4), but have never been isolated. Gas phase techniques may provide significant advantages in the formation of transition metal containing clusters like these with unusual structures and unique properties. However, no generally applicable methodology has emerged with which to produce, isolate and characterize these kinds of materials. In this chapter, a new strategy for the isolation of metal-based clusters using a new laser vaporization flow-tube reactor device (LVFR) is presented.

Many kinds of metal and semiconductor clusters can be produced in solution using conventional synthetic methods. For example, noble metal colloids have been known since the time of Faraday,[6] and the same general kind of chemistry employed by Faraday is now used to form clusters of silver, gold, platinum, palladium, etc.[7-17] These particles can cover a wide size range, but all are stabilized and soluble because of various kinds of ligand or surfactant coatings. Semiconductor quantum dots may also be produced by similar methods.[18-25] However, these procedures are not general for all metals or metal compounds. Although solution-based synthetic methods for clusters of transition metals and their compounds exist,[26-28] these methods have difficulty with these systems because of their reactivity.

On the other hand, the laser vaporization method is applicable to any metal, and gas phase cluster sources avoid reactions with ligands and/or solvent species in the critical phase of particle

growth. By subsequent ligand addition downstream in a flowing gas tube, it should be possible to achieve passivation after particle growth has reached a desired level. However, no one to our knowledge has yet combined a laser cluster source with a separate ligand injection method to approach the synthesis of ligand-coated metal clusters. Our strategy to address these issues is to produce clusters in the gas phase using the laser vaporization method,[29] followed by coating with the appropriate ligand, as is already done in solution-based synthetic procedures. After gas phase processing in the flowtube system, the stabilized clusters are trapped in solution where they can be treated with more conventional chemistry techniques.

Andres and coworkers have previously described a method of gas phase cluster synthesis in a flowtube with downstream ligand addition, which was used to produce ligand-coated gold clusters.[30-32] Their source employed an arc discharge or oven source, which cannot be applied to all metals. We have expanded on this concept by using the more general laser source, while employing the proven method demonstrated by Andres for cluster passivation and recovery. This new combination of features should make it possible to produce a variety of new cluster materials. In particular, we have been successful in producing ligand-coated titanium and vanadium oxide clusters in the initial tests of the LVFR system.

Transition metal oxides exhibit a variety of structures and properties. This diversity makes these systems ideal for demonstrating relationships between structure and properties and for showing how these relationships may aid scientists in designing and producing new materials.[33] The crystal structures of transition metal oxides may vary from a simple rock salt structure (TiO,VO) to more complex crystals such as rutile (TiO_2, VO_2) and corundum (Ti_2O_3, V_2O_3).[33] The electronic and magnetic properties of oxides can vary greatly as well; they may act as conductors, semi-conductors, insulators, diamagnetic, or paramagnetic materials depending on composition and

stoichiometry. For instance, TiO is a paramagnetic, conducting material, whereas TiO_2 is a diamagnetic, semiconductor material.[33] Their unique range of structures and properties have thus made transition metal oxide materials useful in catalysis, optics and electronics.

5.2 EXPERIMENTAL

The LVFR instrument which combines a laser vaporization cluster source with the flowtube reactor and ligand spray for cluster stabilization is described in Section 2.2. The metal samples for these experiments are ½ inch diameter rods of titanium or vanadium metal which are polished prior to the experiment. The metal rod is rotated slowly by a synchronous motor as it is vaporized with the KrF excimer laser. A continuous expansion of helium gas for collisional quenching and cooling of the laser generated vapor flows over the sample surface; the pressure in this flowtube when the experiment is in operation is 20-40 torr. In the passivation zone, tetrahydrofuran (THF, C_4H_8O) is injected either directly as vapor in an argon gas flow or as an aerosol via a nebulizer spray (Misonix "Micromist"). In the experiments described here, thirty minute runs lead to milligram samples sufficient for subsequent analysis. After collection, the samples are sealed under argon until they could be analyzed using mass spectrometry. For mass spectrometry, one or two drops of the solution are applied to a 5 mm dia. stainless steel probe tip, which is then dried under an argon purge and inserted through a vacuum interlock into the laser desorption mass spectrometer described in section 2.1.

5.3 TITANIUM OXIDE – THF

In order to build up to the production and isolation of more complex cluster systems such as ligand-coated met-cars, we first attempted more simple experiments to determine what products

could be produced by vaporizing titanium with no carbon source present. LVFR runs using these conditions, where a titanium rod is vaporized and THF is injected as the ligand/solvent, produce a clear liquid that includes an aggregate of small dark particles. The same type of sample is isolated and similar mass spectra are obtained in analysis when THF is injected using the nebulizer spray or when the vapor present in equilibrium with liquid THF is entrained in argon gas flow and introduced into the flowtube in the gas phase. If the sample is allowed to warm to room temperature, the particles turn light brown in color and eventually decompose, presumably because they have dissolved, but the solution remains clear. However, if the samples are sealed under argon, the particles retain their color and are stable for extended periods (1-2 days). Also, if the particles are dried in air, they first change color (black, to brown to white) and then disappear. This suggests that the sample is volatile and has either evaporated or decomposed. On the other hand, if the particles are dried under an argon flow, then they remain on the probe tip long enough to insert it into the laser desorption mass spectrometer for analysis. In vacuum, the particles on the probe tip are stable for extended periods (days), indicating that reactivity with air is the primary problem.

The top trace of Figure 1 shows a mass spectrum measured for a sample produced using the nebulizer spray for THF addition, while the bottom trace is for a sample generated with THF vapor added as vapor in an argon flow. In the upper trace, there are two prominent masses observed at 416 and 544 amu with an intermediate peak with strong intensity at 432 amu. These masses can all be assigned to various $Ti_xO_y(THF)_z^+$ species, as indicated in the figure by the labels (x, y, z). As noted above, our mass resolution is not good enough to assign the number of titanium atoms in a definitive way with the isotopic pattern of these peaks. In making the mass assignments, we recognize the coincidence between Ti and O_3 at 48 amu, and we therefore chose stoichiometries and structures with reasonable valences for all atoms. Alternative mass assignments would produce

clusters with one fewer titanium atom and three additional oxygen atoms, which produce no chemically reasonable stoichiometries or structures for these low mass clusters. The best assignments for the main peaks are consequently 416 amu = $Ti_2O_2(THF)_4$, 432 amu = $Ti_2O_3(THF)_4$ and 544 amu = $Ti_2O(THF)_6$. In the lower trace, these same mass peaks are present, but the 2,1,6 peak is much less prominent compared to the 2,2,4 and 2,3,4 peaks. Careful studies show that the formation of titanium oxides here is not caused by an air leak in the vacuum system, but rather through reactions with THF.

Figure 2 shows simple structures that can be deduced from the prominent (2,3,4) and (2,1,6) species that have reasonable chemical connectivity. As illustrated, they both consist of a Ti-O-Ti core surrounded by THF ligands. However, the (2,3,4) species represents a structure terminated by oxygen at the ends, while the (2,1,6) represents a structure terminated with THF. The 416 amu peak assigned to the 2,2,4 stoichiometry, can then be seen to correspond to the 2,3,4 cluster that has fragmented by the loss of one terminal oxygen. The lower mass ions seen in Figure 1 can all be rationalized as fragments of these basic units. For example, mass 288 (2,3,2) can be formed by fragmentation of two THF units from mass 432, and 184 represents the loss of all but one THF from mass 544. The structures suggested here for these linear Ti-O-Ti based complexes have not been observed previously, but they are reasonable chemically. In fact, there are several known synthetic organometallic complexes that have the same kind of linear Ti-O-Ti-O connectivity proposed here, but with other ligands protecting the core structure.[34-37]

Figure 3 shows another mass spectrum of titanium-oxygen-THF clusters in which the THF was added with the nebulizer and a higher laser desorption was employed. The higher concentrations of THF under these conditions apparently led to more efficient production of the 544 mass (2,1,6), THF-terminated structures. However, an interesting series of larger clusters also

occurs in the mass range above 600 amu. Masses at 623 and 824 are apparent, as well as a progression of larger masses. The 624 amu peak can be assigned to the $Ti_3O_3(THF)_6$ stoichiometry (3,3,6), which could be the next larger member in the series having the same type of structure as the 416 mass (2,2,4), but extended by one $Ti(THF)_2O$ unit. Likewise, the cluster at mass 824 could be assigned the stoichiometry of 5,5,7, which could have a similar structure that lost several THF units by fragmentation. In these larger masses, it again becomes important to note the mass coincidence between Ti and O_3. With this in mind, the 824 mass can alternatively be assigned to a stoichiometry of 4,8,7, which can also be written as $(TiO_2)_4(THF)_7$. If this stoichiometry is correct, then the larger series of clusters may have switched from a 1:1 Ti/O linear structural pattern observed in the clusters in Figure 1, to one with three-dimensional structures having the 1:2 Ti/O ratio that is more characteristic of bulk titanium oxide.

The regular pattern of larger clusters in the 1000-2000 amu range is particularly notable. It is interesting to consider whether the $Ti_xO_y(THF)_z$ structural patterns suggested in Figure 2 could be extended to produce a family of polymers that might fall in this higher mass range. The two polymer families that can be generated are $Ti_xO_{x+1}(THF)_{2x}$ (Figure 2, upper) and $Ti_xO_{x-1}(THF)_{2x+2}$ (Figure 2, lower), for various values of x. For both cases, each member in the polymer family would increase by one formula unit of $TiO(THF)_2$, which corresponds to a mass increment of 208 amu. For the first family, The x=1 cluster with the formula $TiO_2(THF)_2$ has the index number 1,2,2 and is found at mass 224, as seen in the lower trace of Figure 1. The x=2 species is the mass 432 cluster represented in Figure 2. However, larger members of this series that would be predicted at masses of 640, 848, 1056, etc. are not observed, i.e. none of these masses correspond to the higher masses observed in Figure 3. For the second family, the x=1 member of this family would be $Ti(THF)_4$, which we do not see. The x=2 cluster is the mass 544 species, but other members of this

polymer family predicted at masses 752, 960, 1168, etc. are not observed. Therefore, the linear polymeric Ti-O-Ti-O species suggested at lower mass cannot explain the full pattern of higher mass clusters, and consequently other assignments must be considered for these species.

The most prominent of the peaks in the progression at higher mass appear to be spaced by constant intervals of approximately 76 amu. This is initially puzzling, since intervals of 76 amu cannot be assigned to any multiple of Ti, O or THF. However, if we remember the possibility of TiO_2 (mass 80) units in these clusters, as we discussed above for the 824 amu species, then a possible pattern emerges. We can understand these spectra if we note that our resolution is limited in this higher mass region leading to peak widths that correspond to ±8 amu. Considering this, the intervals at 76 could be an average of roughly equal intensity mass peaks occurring at the intervals of 72 (THF) and 80 (TiO_2) amu, that are not resolved. We can therefore conclude that the masses in the higher region most likely correspond to various species of the general form $(TiO_2)_m(THF)_n$. The smaller multiplet peaks also seen in this region correspond to oxygen intervals above and below the central peak. Thus, the linear Ti-O-Ti-O growth pattern observed at low masses must switch to species with stoichiometries resembling the bulk material.

The specific stoichiometries that give rise to the higher masses seen are indicated as progressions of the form $(TiO_2)_m(THF)_n$ in Figure 3. As indicated by the numbering system, the main progression members seen correspond to clusters with either 10, 11, 12 or 13 units of TiO_2 and 3-8 THF ligands. Clusters with more TiO_2 units also have more THF ligands. Although this general behavior seems reasonable, to our knowledge this is the first report of such small titanium oxide clusters stabilized with ligand coatings. In the mass spectrum, it appears that only small particles with 10-13 units of TiO_2 are formed in the LVFR. However, it may be that clusters of this

size range are preferentially desorbed by the laser under these conditions and that larger particles are present but are fragmented or not detected.

5.4 VANADIUM OXIDE – THF

The success of producing THF coated titanium oxide clusters led us to also explore vanadium in hopes of observing similar behavior. Figure 4 is a representative mass spectrum obtained when vanadium is vaporized and THF is injected as vapor in an argon gas flow. The resulting products are then isolated and remain under an argon purge until analysis can be performed. Once again, a dark particulate matter is trapped which also apparently degrades when exposed to air, suggesting that the sample is volatile and has either evaporated or decomposed. Therefore, the solution (with particles) is placed on the laser desorption probe tip and dried under an argon purge before transferring to the laser desorption mass spectrometer. Once in vacuum, a thin film of crystals can be observed on the probe tip utilizing the attached camera. It remains unknown whether the mass spectrum observed (Figure 4) is due to the particles observed upon isolation or the thin film of material observed following the drying process. Filtration of the products isolated on the LVFR results in the loss of all material, presumably because the vanadium oxide particles stick to the filter paper.

As in the titanium oxide-THF experiments, we expected to isolate linear V-O-V-O chain structures surrounded by THF units or larger clusters more representative of bulk vanadium oxide also surrounded by THF. However, the mass spectrum observed is noticeably different. Figure 4 contains only one general progression of peaks in the mass region above 400 amu, spaced by approximately 61 amu (Figure 4). Uranyl acetate (UAc) was added to the probe tip for the purposes of mass calibration, resulting in the observed UO and UO_2 peaks. Figure 5

shows a zoomed in view of the 300-1300 mass region of interest. The masses represented by this progression do not correspond to either a $V_xO_{x+1}(THF)_{2x}$ or $V_xO_{x-1}(THF)_{2x+2}$ polymer family as observed in the titanium oxide-THF experiments. For a $V_xO_{x+1}(THF)_{2x}$ polymer family, clusters predicted at masses 277, 438, 649, etc. are not observed, and for a $V_xO_{x-1}(THF)_{2x+2}$ polymer family, clusters predicted at masses 339, 550, 761, etc. are also not observed. Therefore, we were forced to consider alternative assignments for this spectrum.

The 61 amu peak to peak spacing is also puzzling since it does not correspond to any multiple of V, O, or THF. Consequently, it can not be assigned to multiples of the bulk stoichiometries for vanadium oxides, i.e. VO, VO_2, V_2O_3, and V_2O_5.[33] Fortunately, previous work on vanadium oxide clusters performed by Castleman and coworkers and our group leads to a plausible answer. Figure 6 is a representative mass spectrum of vanadium oxide clusters produced by laser vaporization in a molecular beam. Surprisingly, the spectrum observed is not a statistical distribution of clusters but instead contains specific stoichiometries of vanadium oxide clusters.[38-44] The stoichiometries in each family found to be the most stable in fixed frequency laser fragmentation experiments are the clusters, $V_2O_4^+$, $V_3O_7^+$, $V_4O_9^+$, $V_5O_{12}^+$, and $V_7O_{17}^+$.[44] Therefore, we also might expect to isolate clusters with these same or similar stoichiometries possibly surrounded by THF units in our LVFR experiments. Tentative assignments for the $V_xO_y(THF)_z$ cluster progression are indicated in the figure using the labels (x,y,z). However, many different stoichiometeries could potentially explain each peak in the progression. For example, the cluster observed at mass 700 is within ±5 amu of many reasonable stoichiometries, including $V_2O_6(THF)_7$, $V_3O_7(THF)_6$, $V_5O_5(THF)_5$. Consequently, Figures 4 and 5 are labeled with stoichiometries which most agree with previous molecular beam results and produce rational structures.

Figure 7 presents reasonable structures for three of the clusters in the progression (masses 454, 649 and 697) with the V_2O_4, V_3O_4 and V_3O_7 core stoichiometries protected by THF molecules. Many researchers have calculated the structures of smaller vanadium oxide clusters[45-47] but more recently, Bernstein and coworkers performed an extensive theoretical study on the V_2O_4, V_3O_7, and V_4O_9 species. Thus, we utilized these results and added an appropriate number of THF molecules to each of the exposed vanadium atoms in each cluster. In the instance of $V_3O_4(THF)_6$, the terminal oxygen molecules are absent, resulting in a vanadium oxide core surrounded by THF molecules. The other two species illustrated in the figure, $V_2O_4(THF)_4$ and $V_3O_7(THF)_6$, are presented as calculated by Bernstein and coworkers with four and six THF molecules added, respectively, in order to minimize spatial interactions.

5.5 CONCLUSIONS

A new laser vaporization flowtube reactor is described and its performance is demonstrated for the first time in the synthesis and isolation of new titanium and vanadium oxide clusters with THF. We suggest that the titanium oxide-THF clusters contain linear metal oxide cores, which shift to produce three-dimensional TiO_2 clusters at larger cluster sizes. However, vanadium oxide-THF produced an entirely different result. In this case we suggest that the clusters adopt structures similar to "magic number" vanadium oxide clusters seen in other gas phase experiments. Thus, these are the first such examples of ligand-coated metal oxide clusters of such small size.

Although these experiments may be refined in the future, possibly utilizing IR, UV-VIS spectroscopy and/or electron microscopy for additional analysis, it is already clear that the laser vaporization flow reactor provides a new and effective method for the production and isolation of cluster materials. Unfortunately, many of the variables in these experiments have not been

optimized (laser pulse energy, gas flow rates, gas mixtures, ligand concentration, etc.). Using this LVFR method, only one of these variables may be altered per run, with feedback only coming following analysis of the samples that are isolated. Consequently, real-time analysis of the products being produced on the LVFR is desired, leading to the addition of an online reflectron time-of-flight mass spectrometer which will be discussed in greater detail in the concluding chapter.

5.6 REFERENCES

(1) Kroto, H. W.; Heath, J. R.; O'Brien, S. C.; Curl, R. F.; Smalley, R. E. *Nature* **1985**, *318*, 162.

(2) Kroto, H. W. *Science* **1988**, *242*, 1139.

(3) Curl, R. F.; Smalley, R. E. *Science* **1988**, *242*, 1017.

(4) Krätschmer, W.; Lamb, L. D.; Fostirpoulos, K.; Huffman, D. R. *Nature* **1990**, *347*, 354.

(5) *Science of Fullerenes and Carbon Nanotubes*; Dresselhaus, M. S.; Dresselhaus, G.; Eklund, P. C., Eds.; Academic Press: San Diego, 1996.

(6) Faraday, M. *Philos. Trans.* **1857**, *147*, 145.

(7) Schmid, G.; Emde, S.; Maihack, V.; Meyer-Zaika, W.; Peschel, S. *J. Mol. Catal. A* **1996**, *107*, 95.

(8) Schmid, G. *Nanostruc. Mater.* **1996**, *6*, 15.

(9) Schmid, G. *Prog. Colloid Polym. Sci.* **1998**, *111*, 52.

(10) Whetten, R. L.; Khoury, J. T.; Alvarez, M. M.; Murthy, S.; Vezmar, I.; Wang, Z. L. *Adv. Mater.* **1996**, *8*, 428.

(11) Petroski, J. M.; Wang, Z. L.; Green, T. C.; El-Sayed, M. A. *J Phys Chem B* **1998**, *102*, 3316.

(12) Wang, Z. L.; Mohamed, M. B.; Link, S.; El-Sayed, M. A. *Surf. Sci.* **1999**, *440*, L809.

(13) Mohamed, M. B.; Wang, Z. L.; El-Sayed, M. A. *J. Phys. Chem. A* **1999**, *103*, 10255.

(14) Petit, C.; Taleb, A.; Pileni, M. P. *J Phys Chem B* **1999**, *103*, 1805.

(15) Nikoobakht, B.; Wang, Z. L.; El-Sayed, M. A. *J Phys Chem B* **2000**, *104*, 8635.

(16) Filankembo, A.; Pileni, M. P. *Appl. Surf. Sci.* **2000**, *164*, 260.

(17) Pileni, M. P. *Pure Appl. Chem.* **2000**, *72*, 53.

(18) Steigerwald, M. L.; Alivisatos, A. P.; Gibson, J. M.; Harris, T. D.; Kortan, R.; Muller, A. J.; Thayer, A. M.; Duncan, T. M.; C., D. D.; Brus, L. E. *J. Am. Chem. Soc.* **1988**, *110*, 3046.

(19) Bawendi, M. C.; Steigerwald, M. L.; Brus, L. E. *Annu. Rev. Phys. Chem.* **1990**, *41*, 477.

(20) Brus, L. *Adv. Mater.* **1993**, *5*, 459.

(21) Brus, L. *J. Phys. Chem. Solids* **1998**, *59*, 459.

(22) Rockenberger, J.; Scher, E. C.; Alivisatos, A. P. *J. Am. Chem. Soc.* **1999**, *121*, 11595.

(23) Murray, C. B.; Kagan, C. R.; Bawendi, M. G. *Annu. Rev. Mater. Sci.* **2000**, *30*, 545.

(24) Mikulec, F. V.; Kuno, M.; Bennati, M.; Hall, D. A.; Griffin, R. G.; Bawendi, M. G. *J. Am. Chem. Soc.* **2000**, *122*, 2532.

(25) Manna, L.; Scher, E. C.; Alivisatos, A. P. *J. Clust. Sci.* **2002**, *13*, 521.

(26) Guzelian, A. A.; Banin, U.; Lee, J. C.; Alivisatos, A. P. *Adv. Metal Semiconductor Clusters* **1998**, *4*, 1.

(27) Crawford, N. R. M.; Hee, A. G.; Long, J. R. *J. Am. Chem. Soc.* **2002**, *124*, 14842.

(28) Yang, J. Y.; Shores, M. P.; Sokol, J. J.; Long, J. R. *Inorg. Chem.* **2003**, *42*, in press.

(29) Dietz, T. G.; Duncan, M. A.; Powers, D. E.; Smalley, R. E. *J. Chem. Phys.* **1981**, *74*, 6511.

(30) Bowles, R. S.; Kolstad, J. J.; Calo, J. M.; Andres, R. P. *Surf. Sci.* **1981**, *106*, 117.

(31) Mahoney, W.; Andres, R. P. *Mater. Sci. Eng. A* **1995**, *A204*, 160.

(32) Mahoney, W.; Kempe, M. D.; Andres, R. P. *Mater. Res. Soc. Symp. Proc.* **1996**, *400*, 65.

(33) Rao, C. N. R.; Raveau, B. *Transition Metal Oxides: Structure, Properties, and Synthesis of Ceramic Oxides*, 2nd ed.; Wiley-VCH: New York, 1998.

(34) Franceschi, F.; Gallo, E.; Solari, E.; Floriani, C.; Chiesi-Villa, A.; Rizzoli, C.; Re, N.; Sgamellotti, A. *Chem. Eur. J.* **1996**, *2*, 1466.

(35) Roth, A.; Floriani, C.; Chiesi-Villa, A.; Guastini, C. *J. Am. Chem. Soc.* **1986**, *108*, 6823.

(36) Andres, R.; Galakhov, M.; Martin, A.; Mena, M.; Santamaria, C. *Organometallics* **1994**, *13*, 2159.

(37) Alvarez, M. M.; Vezmar, I.; Whetten, R. L. *J. Aerosol Sci.* **1998**, *29*, 115.

(38) Bell, R. C.; Zemski, K. A.; Kerns, K. P.; Deng, H. T.; Castleman, A. W. *J. Phys. Chem. A* **1998**, *102*, 1733.

(39) Bell, R. C.; Zemski, K. A.; Castleman, A. W. *Abstr. Pap. Am. Chem. S.* **1999**, *218*, U335.

(40) Kooi, S. E.; Castleman, A. W. *J. Phys. Chem. A* **1999**, *103*, 5671.

(41) Bell, R. C.; Zemski, K. A.; Justes, D. R.; Castleman, A. W. *J. Chem. Phys.* **2001**, *114*, 798.

(42) Justes, D. R.; Mitric, R.; Moore, N. A.; Bonacic-Koutecky, V.; Castleman, A. W. *J. Am. Chem. Soc.* **2003**, *125*, 6289.

(43) Justes, D. R.; Moore, N. A.; Castleman, A. W. *J Phys Chem B* **2004**, *108*, 3855.

(44) Molek, K. S.; Jaeger, T. D.; Duncan, M. A. *J. Chem. Phys.* **2005**, *123*.

(45) Fielicke, A.; Mitric, R.; Meijer, G.; Bonacic-Koutecky, V.; Von Helden, G. *J. Am. Chem. Soc.* **2003**, *125*, 15716.

(46) Calatayud, M.; Andres, J.; Beltran, A. *J. Phys. Chem. A* **2001**, *105*, 9760.

(47) Calatayud, M.; Silvi, B.; Andres, J.; Beltran, A. *Chem. Phys. Lett.* **2001**, *333*, 493.

(48) Matsuda, Y.; Bernstein, E. R. *J. Phys. Chem. A* **2005**, *109*, 3803.

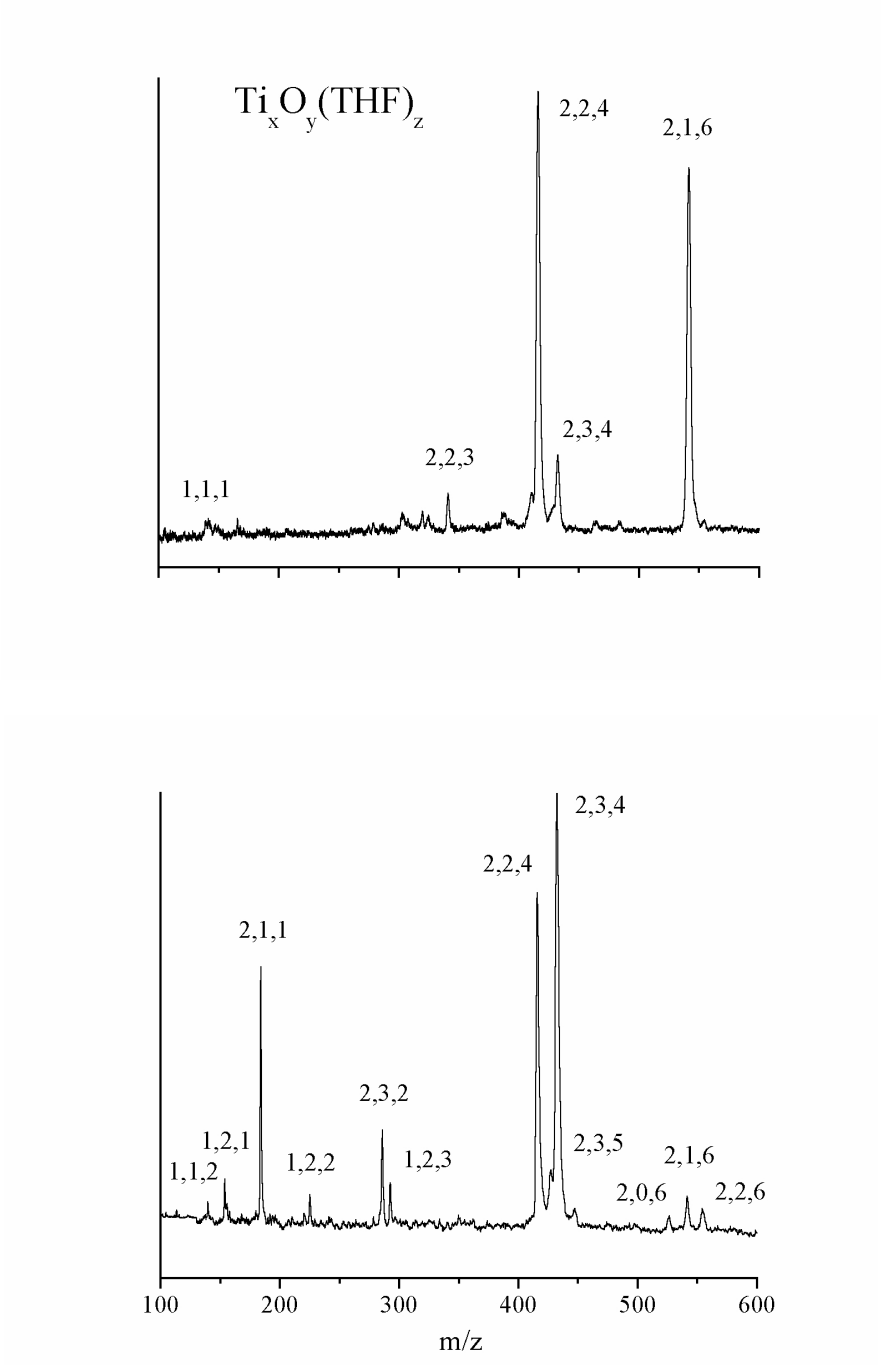

Figure 1. Mass spectra of clusters isolated from the LVFR of titanium with a aerosol spray of THF (upper trace) compared to an experiment in which the ligand was added entrained at its ambient partial pressure in argon. Masses of the form $Ti_xO_y(THF)_z$ are indicated with an x,y,z index.

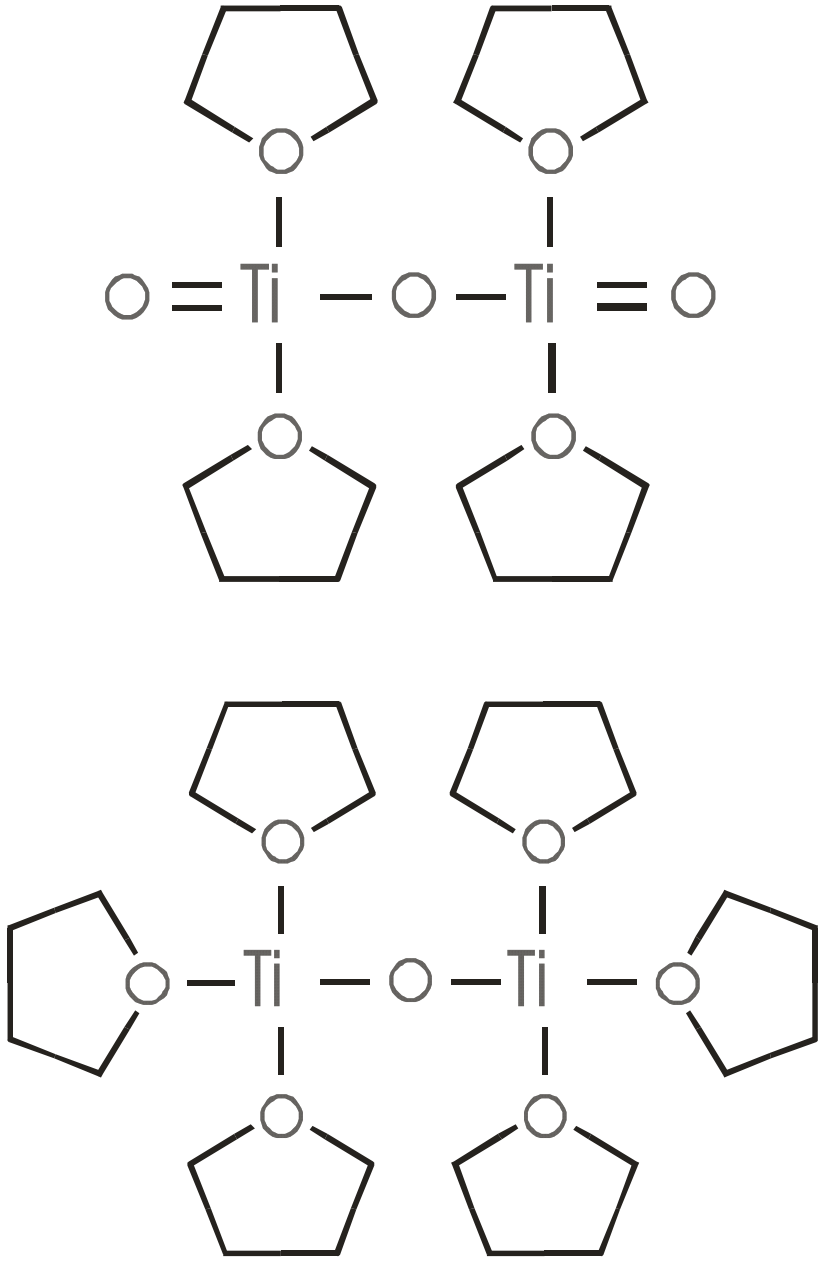

Figure 2. Structures proposed for the titanium oxide-THF clusters having masses of 432 and 544. Both contain the same linear titanium oxide core, with oxide (upper) versus THF (lower) termination.

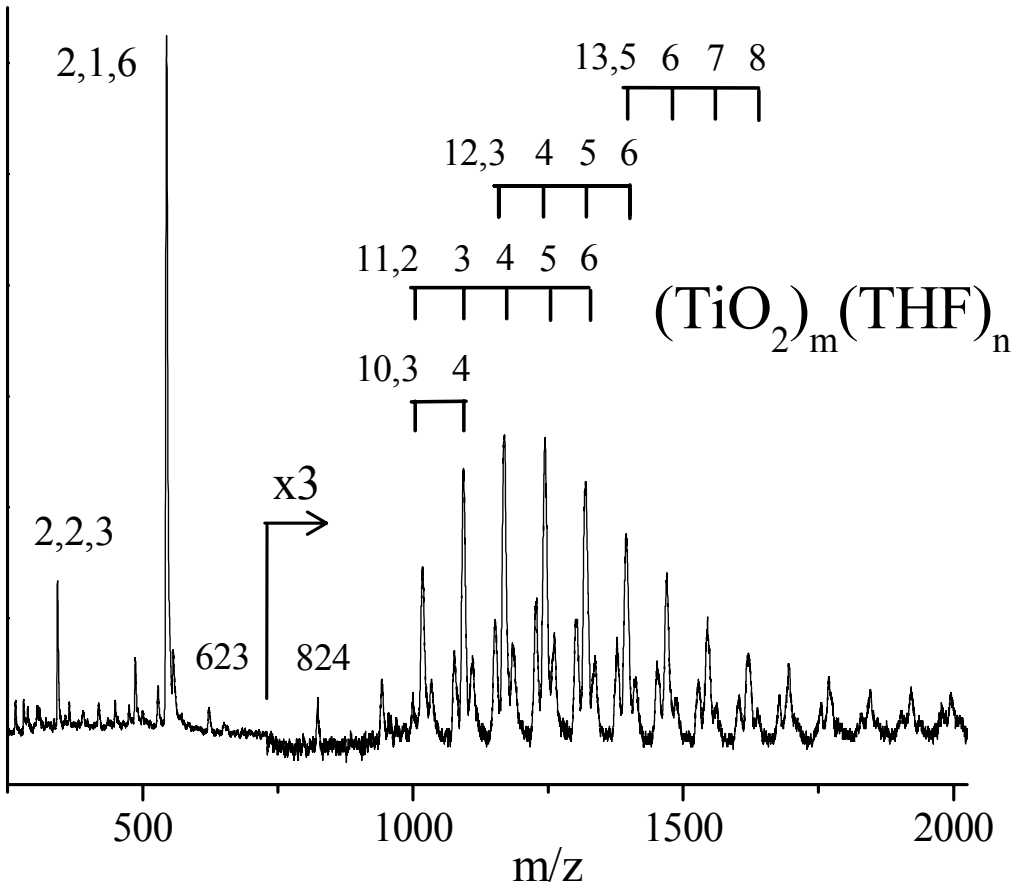

Figure 3. Mass spectrum of titanium oxide-THF clusters when THF is added as a ligand spray from the nebulizer and a higher desorption laser power (~2 mJ/pulse) is employed in analysis of the products. Larger clusters are assigned to $(TiO_2)_m(THF)_n$ masses.

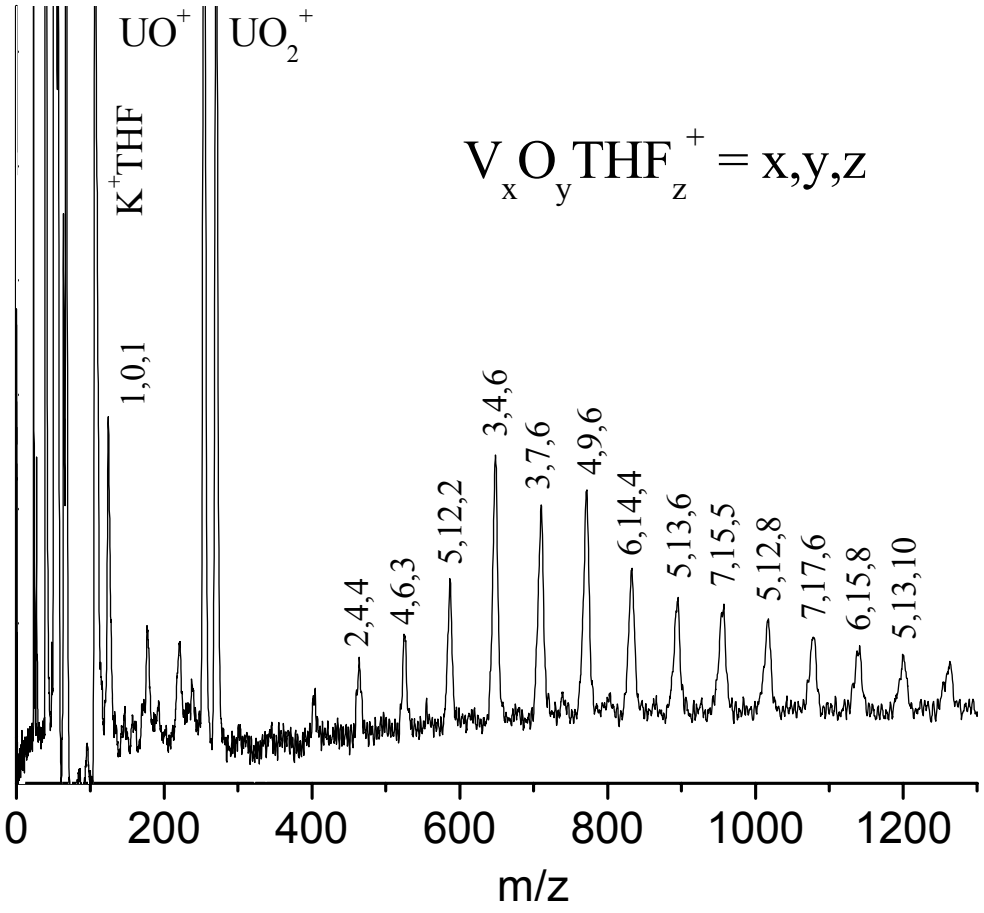

Figure 4. Mass spectrum of vanadium oxide-THF clusters when THF is added directly as vapor in an argon gas flow. Larger clusters are assigned to $V_xO_yTHF_z$ masses.

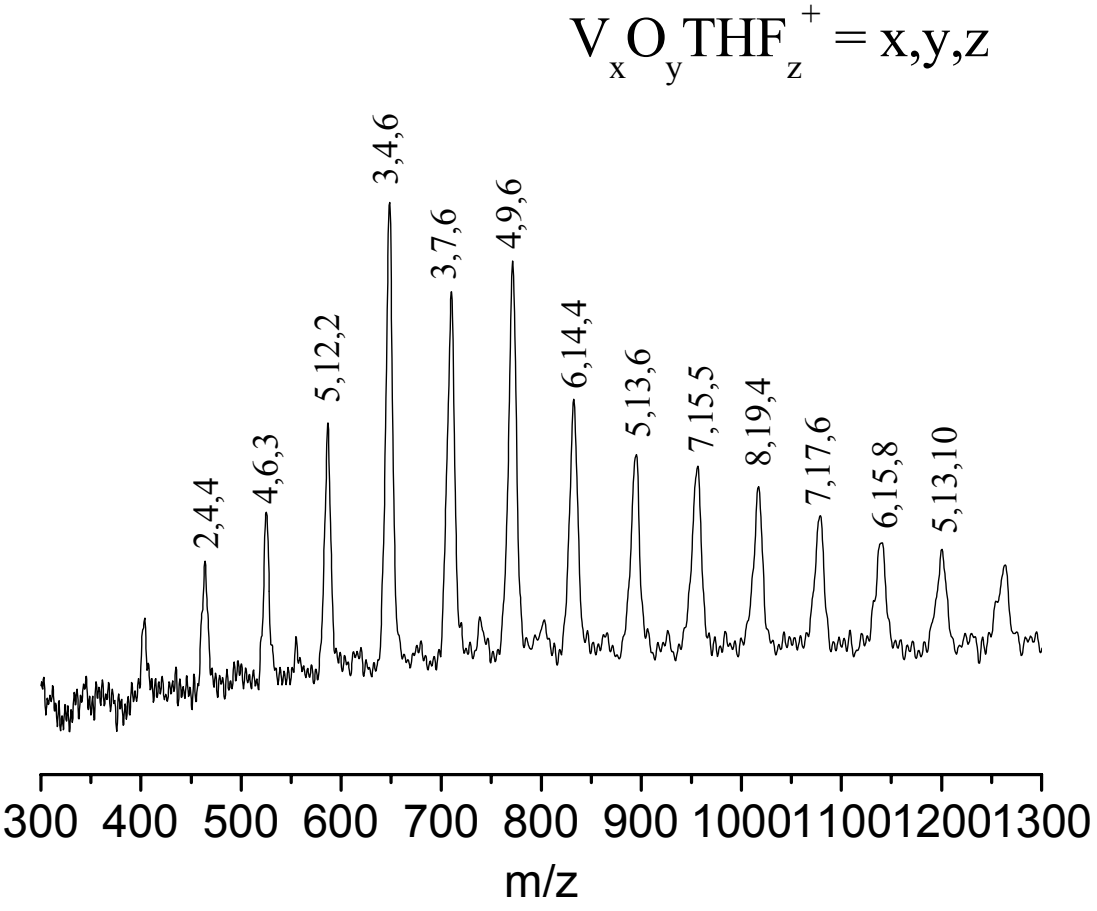

Figure 5. Zoom for the mass region between 300 amu and 1300 amu showing the distribution of vanadium oxide – THF clusters of the form $V_xO_yTHF_z$

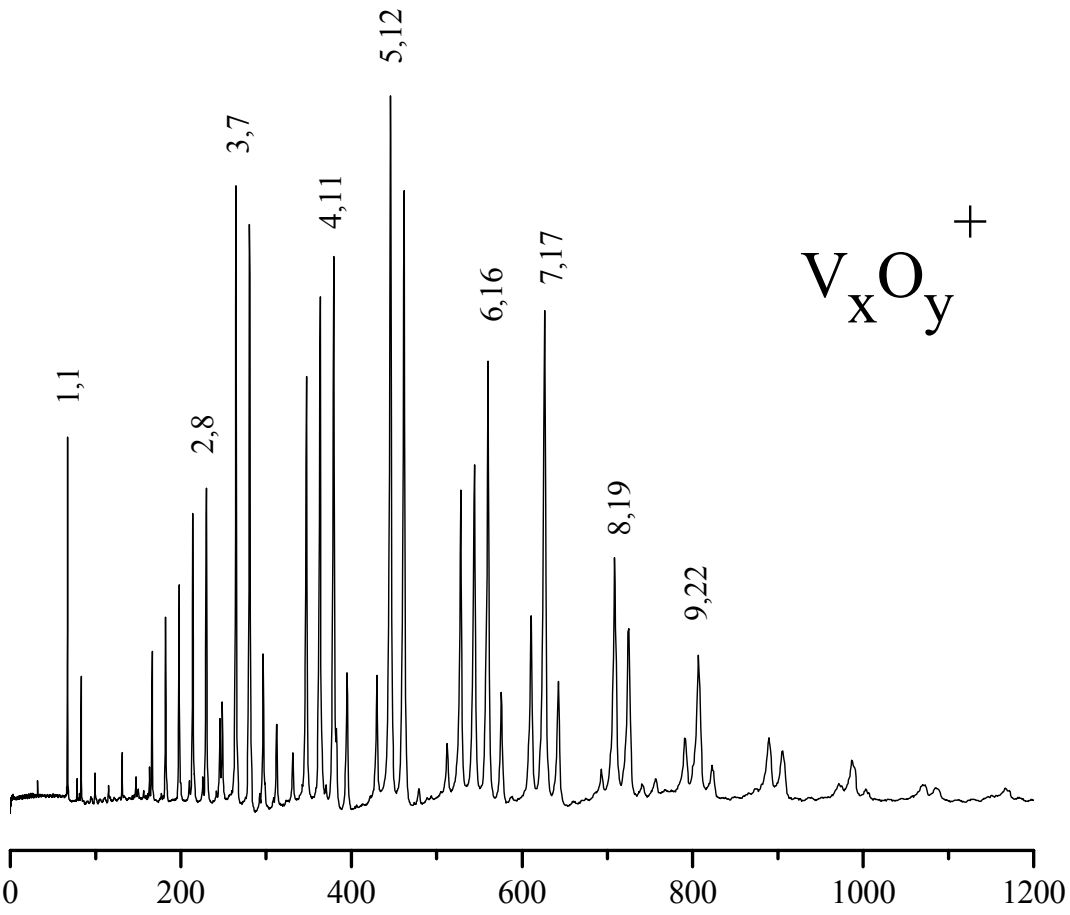

Figure 6. Distribution of vanadium oxide clusters produced by molecular beam experiments.[44]

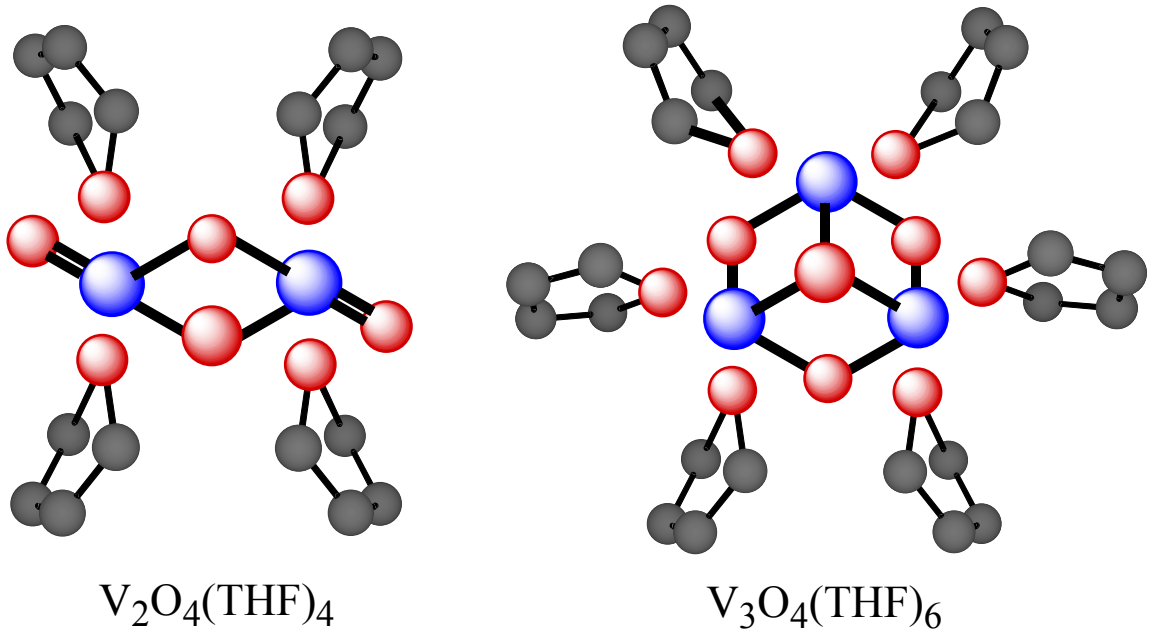

$V_2O_4(THF)_4$ $V_3O_4(THF)_6$

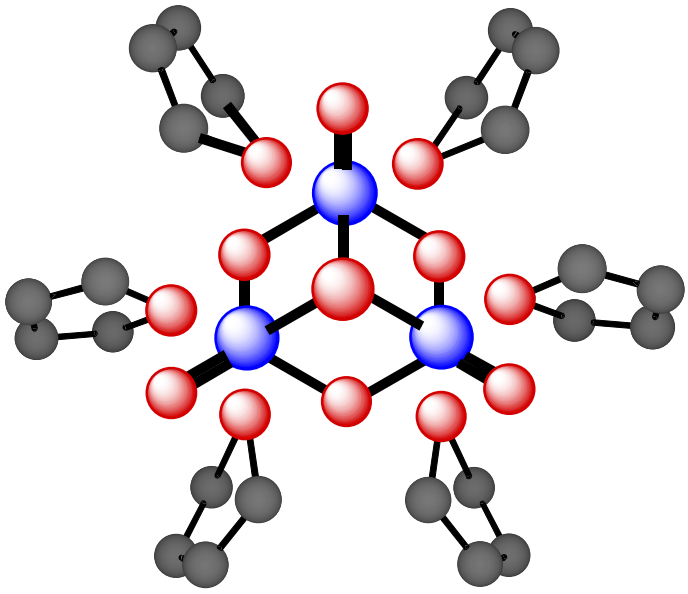

$V_3O_7(THF)_6$

Figure 7. Proposed structures of vanadium oxide -THF cluster molecules. The core V_xO_y structures were derived from previous calculations by Bernstein and coworkers.[48]

CHAPTER 6

FUTURE DIRECTIONS

6.1 LASER VAPORIZATION FLOWTUBE MODIFICATIONS

The initial version of the LVFR system possessed two flaws which limited progress greatly. With no means of analyzing the clusters as they were being produced, each experiment was performed assuming the proper conditions for cluster synthesis had been created. Even in the cases where we succeeded in producing substantial amounts of material, as in titanium/vanadium oxide – THF experiments discussed in Chapter 5, it remains unlikely that we struck upon the conditions for synthesis which would result in the highest percentage yield. Since the process of production, isolation and analysis requires an average time of two hours per run, exploring a wide range of conditions is not feasible given the number of variables (laser power, gas pressures, flow rates, ligand concentration, etc.).

Another possible issue lies in the method of analysis. Determination of size and composition of metal containing particles is not an easy task. Laser desorption mass spectrometry analysis methods described in section 2.1 may selectively desorb clusters of certain sizes or composition. There is also a possibility that the laser desorption/ionization process may alter the product composition completely. These two issues must be resolved before this experiment can realize its true potential.

An online reflectron time-of-flight mass spectrometer (RTOF-MS) has been added to the LVFR in order to optimize synthetic conditions before initializing the isolation process. By monitoring the clusters produced within the flowtube in real-time, this addition should allow for the exploration of a wide range of conditions. A figure of the present version of the LVFR combining a RTOF-MS produced by the Jordan Company[1] is presented in Figure 4. Material from the flowtube is sampled into the spectrometer via a continuous flow through a small aperture (1/3 - 1 mm dia.). Ionization occurs in the mass spectrometer chamber using an ArF

excimer laser (GAM EX10-300, 25 mJ/pulse, 300 Hz); the ions produced are then accelerated down the flight tube and detected using a microchannel plate detector (MCP). Signals pass through a fast preamplifier (Stanford SR445A) and are subsequently collected with a digital oscilloscope (LeCroy 6100 Waverunner) and transferred to a PC via an IEEE-488 interface for processing.

Knowing what material is being produced by the LVFR during the production process will allow for continuously altering synthetic conditions until the desired clusters are produced in the greatest abundance before beginning the isolation process. Furthermore, cluster distributions observed in online analysis using the Jordan instrument can be compared to the results of subsequent analysis techniques to test the validity of the analysis techniques. If the products observed in the RTOF-MS match with those observed in post-production analysis and characterization, then we will be assured that the sample has been unaltered in the isolation/analysis steps of the process.

6.2 FUTURE EXPERIMENTS

The first experiments that will be performed on the modified LVFR will be titanium and vanadium oxide coated materials. This will provide a good starting point for testing the new apparatus, since we already know that the LVFR is efficient in producing these clusters. It will also provide the chance to see if the cluster distributions seen in previous experiments can be produced more efficiently or even altered to produce a desired series of clusters. We remain interested in producing met-cars in bulk amounts. However, it also remains unclear which ligand systems will be best for coating and protecting these species, since we have already observed that ligands containing oxygen tend to dissociate and produce transition metal oxide materials

instead. We are also interested in isolating transition metal-PAH adducts such as those reported in Chapter 4. These species also pose a different problem, as the solubility these complexes is likely to be limited in most solvents However, we remain optimistic that these problems may be solved given time and effort, and that new and interesting materials may be produced by this new and versatile technique.

6.3 REFERENCES

(1) R. M. Jordan Company, Inc., 2006; Vol. 2006.

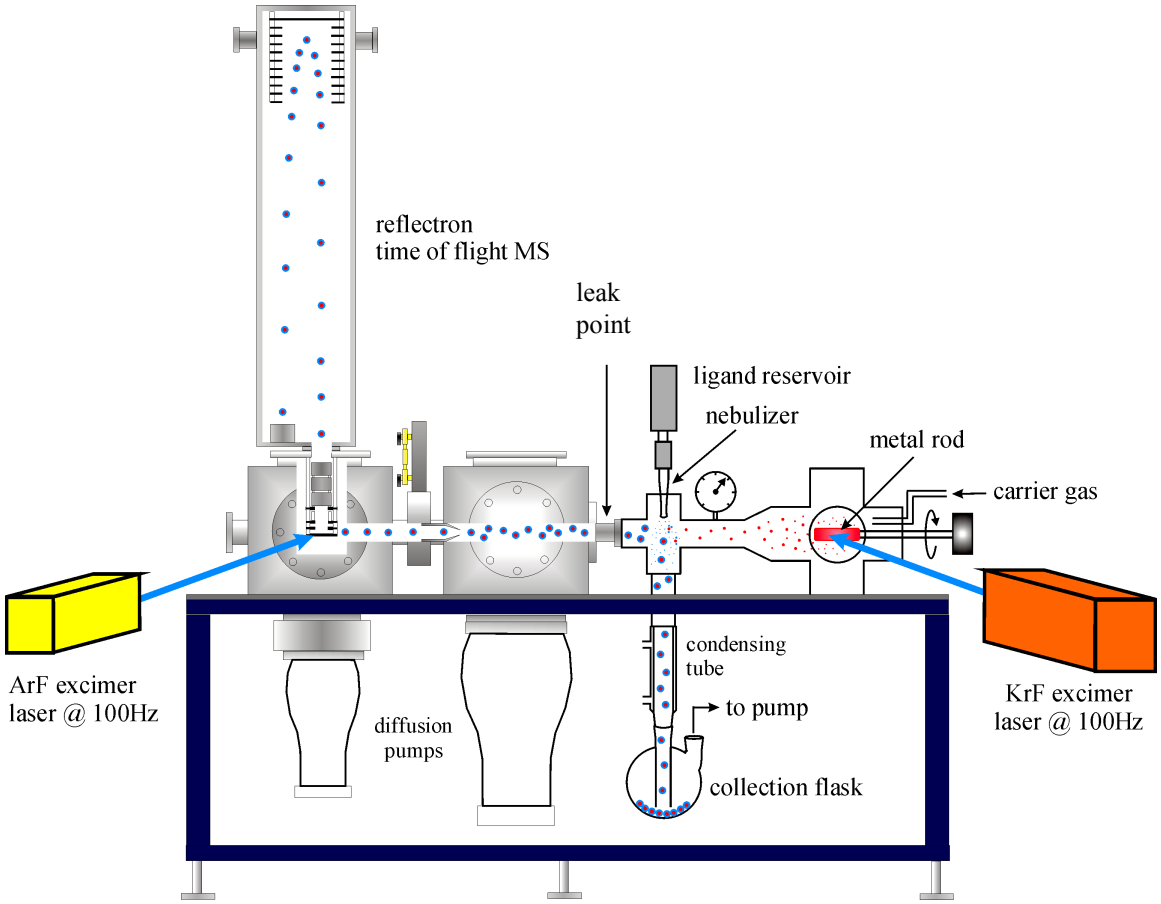

Figure 1. Laser vaporization flowtube with mass spectrometer attached for real-time reaction analysis.